Alma Mater Studiorum – Università di Bologna

DOTTORATO DI RICERCA IN CHIMICA

Ciclo XXVIII

**Settore Concorsuale di afferenza:** 03/A2

**Settore Scientifico-Disciplinare:** CHIM/02

# High-voltage lithium-ion batteries for a sustainable transport

**Presentata da:** Francesca De Giorgio

**Coordinatore Dottorato**

Prof. Aldo Roda

**Relatori**

Prof.ssa Marina Mastragostino

Prof.ssa Catia Arbizzani

**Esame finale anno 2016**

# Table of Contents

List of symbols ..... I

Acknowledgments ..... V

Abstract ..... VII

**Chapter 1. Introduction ..... 1**

1.1 Overview ..... 1

1.2 Lithium-ion batteries ..... 4

1.3 Cathode materials for lithium-ion batteries ..... 5

1.3.1 High-voltage cathode materials: $LiNi_{0.4}Mn_{1.6}O_4$ and $LiNi_{0.5}Mn_{1.5}O_4$ ..... 9

1.4 Strategies to improve the interface stability in $LiNi_{0.4}Mn_{1.6}O_4$ and $LiNi_{0.5}Mn_{1.5}O_4$ electrodes ..... 13

1.4.1 Electrolytes and additives for high-voltage cathode materials ..... 13

1.4.2 Particle size ..... 18

1.4.3 Surface modification ..... 19

1.4.4 Reduced graphene oxide as additive in $LiNi_{0.5}Mn_{1.5}O_4$-based electrodes ..... 19

1.4.5 Separators ..... 21

1.4.6 Binders for high-voltage cathode materials ..... 25

1.5 Aim of the thesis ..... 29

**Chapter 2. Experimental section ..... 31**

2.1 Chemicals ..... 31

2.2 Equipments for chemical-physical characterizations ..... 34

2.3 Electrode preparation ..... 35

2.4 Electrochemical characterization ..... 37

2.4.1 Tests of $LiNi_{0.4}Mn_{1.6}O_4$ and $LiNi_{0.5}Mn_{1.5}O_4$ composite electrodes in half and

full cells ..... 37
2.4.2 HPPC tests for graphite//$LiNi_{0.4}Mn_{1.6}O_4$ and graphite//$LiNi_{0.5}Mn_{1.5}O_4$ cells ..... 42
2.4.3 Electrochemical characterization of separator ..... 45

**Chapter 3. High-voltage graphite//$LiNi_{0.4}Mn_{1.6}O_4$ cells operating with different electrolytes and separators ..... 47**

3.1 Electrochemical characterization of graphite//$LiNi_{0.4}Mn_{1.6}O_4$ cells with LF30 and additives ..... 48

3.2 Non-conventional PVdF-based separator in high-voltage graphite//$LiNi_{0.4}Mn_{1.6}O_4$ cells ..... 60

3.2.1 Characterization of PVdF-NCC and Celgard®2400 separators ..... 61
3.2.2 Electrochemical characterization of graphite//LNMO cells with PVdF-NCC and Celgard®2400 separators ..... 66

3.3 Conclusions ..... 71

**Chapter 4. The role of conducting additives on electrochemical performance of $LiNi_{0.5}Mn_{1.5}O_4$ composite electrodes ..... 73**

4.1 Electrochemical performance of $LiNi_{0.5}Mn_{1.5}O_4$ composite electrodes featuring different carbonaceous additives ..... 74

4.1.1 $LiNi_{0.5}Mn_{1.5}O_4$ characterization ..... 75
4.1.2 Synthesis and structural characterization of partially reduced graphene oxide ..... 76
4.1.3 Morphological and electrical characterization of the $LiNi_{0.5}Mn_{1.5}O_4$-based powders ..... 77
4.1.4 Electrochemical characterization of $LiNi_{0.5}Mn_{1.5}O_4$ composite electrodes with different carbon blacks as conducting additives ..... 79
4.1.5 Electrochemical characterization of $LiNi_{0.5}Mn_{1.5}O_4$ composite electrodes with different carbon blacks and partially reduced graphene oxide as conducting additives ..... 86
4.1.6 Electrochemical characterization of $LiNi_{0.5}Mn_{1.5}O_4$ composite electrodes with

carbon black Super C65 and reduce graphene oxide as conducting additives .... 90
4.1.7 Graphite//$LiNi_{0.5}Mn_{1.5}O_4$/pRGO-C65 cell ..... 99
4.1.8 $Li^+$ diffusion coefficient evaluation ..... 100
4.2 Conclusions ..... 104
**Chapter 5. Water-soluble sodium carboxymethyl cellulose binder for $LiNi_{0.5}Mn_{1.5}O_4$ electrodes ..... 107**
5.1 Electrochemical performance of $LiNi_{0.5}Mn_{1.5}O_4$ composite electrodes featuring water-soluble carboxymethyl cellulose binder ..... 108
5.1.1 Water-soaked $LiNi_{0.5}Mn_{1.5}O_4$ characterization ..... 109
5.1.2 Electrochemical characterization of $LiNi_{0.5}Mn_{1.5}O_4$ composite electrodes with CMC or PVdF binder ..... 110
5.1.3 Graphite//$LiNi_{0.5}Mn_{1.5}O_4$ cell featuring both electrodes with CMC binder .... 121
5.2 Conclusions ..... 123
**Chapter 6. Characterization tests for power-assist and plug-in hybrid electric vehicle applications ..... 125**
6.1 DOE battery tests for power-assist and plug-in HEV applications on lab-scale cells ..... 126
6.2 High-voltage graphite//$LiNi_{0.4}Mn_{1.6}O_4$ cells for power-assist HEV application ..... 128
6.3 High-voltage graphite//$LiNi_{0.5}Mn_{1.5}O_4$ and graphite//$LiNi_{0.4}Mn_{1.6}O_4$ cells for plug-in HEV application ..... 136
6.3.1 DOE battery tests for plug-in HEV applications on graphite//$LiNi_{0.4}Mn_{1.6}O_4$ cell with pre-industrial electrodes ..... 137
6.3.2 DOE battery tests for plug-in HEV application on graphite//$LiNi_{0.5}Mn_{1.5}O_4$ cells with CMC binder for both electrodes ..... 143
6.4 Conclusions ..... 147
**Chapter 7. Conclusions ..... 151**

**Bibliography.....155**

**List of Publications.....165**

**List of contribution to Conferences .....166**

## List of symbols

| | |
|---|---|
| d | thickness |
| $D_{Li+}$ | lithium ion diffusion coefficient |
| E | energy |
| $i_p$ | peak current |
| $I_s$ | ion path through the separator |
| j | $\sqrt{-1}$ |
| $N_M$ | MacMullin number |
| Q | capacity |
| V | voltage |
| Y | admittance |
| $Y_0$ | ideal capacitance |
| α | Warburg element |
| $\sigma_0$ | ionic conductivity |
| $\sigma_{eff}$ | effective conductivity |
| τ | tortuosity |
| ω | angular frequency of a sinusoidal oscillation; 2πν |

## List of abbreviations

| | |
|---|---|
| AE | available energy |
| $AE_{CD\ Target}$ | available energy target for charge-depleting mode |
| $AE_{CS\ Target}$ | available energy target for charge-sustaining mode |
| AMELIE | Advanced Fluorinated Materials for High Safety, Energy and Calendar Life Lithium Ion Batteries. (European Project in the Seventh Framework Programme) |
| BEV | battery electric vehicle |
| BSF | Battery size factor |

| | |
|---|---|
| C45 | carbon black Super C45 |
| C65 | carbon black Super C65 |
| CC | constant current |
| CD | charge-depleting mode |
| CMC | carboxymethyl cellulose |
| CS | charge-sustaining mode |
| CV | constant voltage |
| DEC | diethyl carbonate |
| DOD | depth-of-discharge |
| DOE | U.S. Department of Energy |
| EAP | Environment Action Programme |
| EC | ethylene carbonate |
| ENEA | Italian National Agency for New Technologies, Energy and Sustainable Economic Development |
| EREV | extended-range electric vehicle |
| $E_{SCT}$ | specific cumulative energy removed from the cell during the static capacity test |
| EU | European Union |
| EV | electric vehicle |
| $F_1EC$ | mono-fluoroethylene carbonate |
| FTIR | Fourier transform infrared spectroscopy |
| GHGs | green-house gases |
| HEV | hybrid electric vehicle |
| HPPC | hybrid pulse power characterization |
| ICE | internal combustion engine |
| IS | impedance spectroscopy |
| LF30 | 1 M $Li[(C_2F_5)_3PF_3]$ in ethylene carbonate : dymethyl carbonate (1:1 w/w) |
| LIBs | lithium-ion batteries |
| LiFAP | lithium tris(pentafluoroethyl)trifluorophosphate ($Li[(C_2F_5)_3PF_3]$) |
| LN05MO | $LiNi_{0.5}Mn_{1.5}O_4$ |

| | |
|---|---|
| LNMO | $LiNi_{0.4}Mn_{1.6}O_4$ |
| LP30 | 1 M $LiPF_6$ in ethylene carbonate : dymethyl carbonate (1:1 w/w) |
| LSV | linear sweep voltammetry |
| MSE | Italian Ministry of Economic Development |
| MW | Microwave |
| NMP | *N*-methyl-2-pyrrolidone |
| OCV | open circuit voltage |
| $P_{dis}$ | discharge pulse power |
| PHEV | plug-in hybrid electric vehicles |
| PP | polypropylene |
| $P_{reg}$ | charge pulse power |
| pRGO | partly reduced graphene oxide |
| PV | photovoltaic |
| PVdF | poly(vinylidene fluoride) |
| $Q_{cc}$ | constant phase element related to the current collector |
| $Q_{ct}$ | constant phase element related to the charge-transfer |
| $Q_{sl}$ | constant phase element related to the surface layer |
| $R_{cc}$ | current collector resistance |
| $R_{ct}$ | charge-transfer resistance |
| $R_{dis}$ | discharge pulse resistance |
| RGO | reduced graphene oxide |
| $R_{reg}$ | charge pulse resistance |
| $R_{sl}$ | surface layer resistance |
| $R_u$ | uncompensated resistance |
| SA | succinic anhydride |
| SC | static capacity |
| SEI | solid electrolyte interface |
| SEM | scanning electron microscopy |
| SOC | state-of-charge |

| | |
|---|---|
| SP | carbon black Super P |
| TEM | transmission electron microscopy |
| USABC | U.S. Advanced Battery Consortium |
| $UE_{CD}$ | useable energy for charge-depleting mode |
| $UE_{CS}$ | useable energy for charge-sustaining mode |
| $UE_{M}$ | useable energy margin |
| XPS | X-ray photoelectron spectroscopy |
| $Z_{im}$ | imaginary part of impedance |
| $Z_{re}$ | real part of impedance |

# Acknowledgments

I would like to express my gratitude to my thesis Supervisors: Prof. Marina Mastragostino for giving me the great opportunity to work in a highly scientific environment at the "Laboratory of Electrochemistry of Materials for Energetics" (LEME) of the University of Bologna where I carried out my PhD work, for being my scientific mentor and for having introduced me to the fascinating world of Electrochemistry, and Prof. Catia Arbizzani for her great scientific support, for being always available in carefully helping and advising me during my work.

I would like to sincerely thank Prof. Stefano Passerini for giving me the great opportunity to spend six months in his research group "Electrochemistry for batteries" at the Helmholtz Institute Ulm (HIU, Ulm - Germany) and for the pleasure of the fruitful scientific discussions.

I am grateful to Dr. Francesca Soavi for the exciting scientific discussions and very useful advices and suggestions. I am thankful to all my colleagues at LEME for their support and friendship.

I am thankful to all my colleagues at HIU for the help and support and for making my stay unforgettable, and to all the partners of the EU-AMELIE Project and the ENEA-MSE Italian Program Agreement "Electrical System Research" for the fruitful discussions.

Finally, I kindly acknowledge the financial support provided by the European Commission in the Seventh Framework Programme FP7-2010-GC-ELECTROCHEMICAL-STORAGE,"Advanced Fluorinated Materials for High Safety, Energy and Calendar Life Lithium Ion Batteries" (AMELIE, Project no.265910), and by the Italian National Agency for New Technologies, Energy and Sustainable Economic Development (ENEA) and the Italian Ministry of Economic Development (MSE) under the Italian Program Agreement "Electrical System Research"; the Department of Chemistry "Giacomo Ciamician" of the University of Bologna that funded the Marco Polo Exchange Programme and the Karlsruhe Institute of Technology (KIT) that funded my six-month Internship at HIU.

## Abstract

One of the key challenges to boost the progress of sustainable alternative energies and sustainable transport is the development of environmentally friendly, low-cost and safe lithium-ion batteries (LIBs) with increased energy and power densities. To promote the large-scale diffusion of the low-fuel consuming vehicles, such as hybrid electric vehicles (HEV) and totally electric vehicles, the development of advanced LIBs with specific energy higher than 200 Wh $kg^{-1}$ is necessary to achieve long electric-driving range. Approaches to increase the energy density of a battery are the use of high-voltage and/or high-capacity cathode materials, and $LiNi_{0.4}Mn_{1.6}O_4$ and $LiNi_{0.5}Mn_{1.5}O_4$ are among the most promising cathode materials for the high theoretical specific capacity of 147 mAh $g^{-1}$ and high nominal operating voltage of 4.7 V *vs.* $Li^+/Li$. The combination with a graphite anode should yield full cells with specific energy higher than 200 Wh $kg^{-1}$. Despite their appealing properties, e.g. low cost, environmental friendliness and good safety, the major concern that limits the use of such materials is their reactivity towards conventional electrolytes, which are prone to decompose at high potentials leading to thick surface layers on the cathode and resulting in capacity loss. Since advanced electrolytes stable over 5 V are under investigation but not yet available, several strategies have been pursued to address the interface instability issues.

This PhD work, developed in the frame of the European AMELIE Project (FP7-Transport) and the ENEA-MSE Italian Project, deals with the development of high energy and power LIBs featuring high-voltage $LiNi_{0.4}Mn_{1.6}O_4$ (LNMO) and $LiNi_{0.5}Mn_{1.5}O_4$ (LN05MO) cathodes, mainly for HEV applications. Starting from the challenging study focused on some cell components, such as electrolyte, separator, conductive additive and electrode binder, whose selection is greatly important when LNMO and LN05MO cathodes are involved, full cells with graphite anodes were assembled and tested according to the U.S. Department of

Energy (DOE) protocols in view of the use of such LIBs for power-assist HEV and plug-in HEV (PHEV) applications.

Fluorinated materials were proved to play a key role for the electrochemical performance of graphite//LNMO cells. It was demonstrated that the use of LF30, a carbonate-based electrolyte with the non-conventional ($Li[(C_2F_5)_3PF_3]$) lithium salt, even in presence of SEI-forming additives, and of the reinforced polyvinylidene fluoride macroporous membrane (PVdF-NCC) as separator significantly improve the rate capability, cycling stability and self-discharge of the cells with respect to those with the conventional LP30-based electrolyte and the commercial polypropylene Celgard®2400 separator.

The study on the effect of different conductive additives on the cycling performance of LN05MO composite electrodes tested in LP30 demonstrated that home-made partially reduced graphene oxide (pRGO) and commercial RGO improve the electrode/electrolyte interface by acting as a protective barrier that hinders the formation of a thick passivation layer of low electronic conductivity on the cathode surface due to the side-reactions with the electrolyte.

The study on the effect of water-soluble carboxymethyl cellulose (CMC) binder carried out during the six-month-Internship at Helmholtz Institute Ulm proved that CMC remarkably improve the cycling performance of LN05MO composite electrodes especially upon long-term cycling in LP30 compared to those having the most widely used PVdF binder.

Furthermore, the results of characterization tests performed according to the DOE protocols demonstrated that graphite//LNMO and graphite//LN05MO cells can meet the DOE targets of energy and power for power-assist HEVs and plug-in HEVs. Outstanding results were obtained with graphite//LNMO cells featuring both electrodes with optimized composition and mass loading suitable for the scale-up of batteries for high-energy demanding plug-in HEV applications.

# Chapter 1. Introduction

## 1.1 Overview

Nowadays, the anthropogenic emissions of green-house gases (GHGs) are higher than ever and are largely determining climate changes. Emissions due to energy consumption account for three-quarters of the anthropogenic GHG emissions, and $CO_2$ contributes for about 60% to the global emissions.[1] Since fossil fuels are the main primary energy supply and the main source of $CO_2$ emissions, the growing energy demand strongly influences the upward trend in $CO_2$ emissions and, then, the shift from a fossil-fuel economy to a low-carbon economy is mandatory. This can be feasible by boosting the progress of sustainable alternative energies and sustainable transport.[2] For instance, automotive transport accounts for more than 20% of $CO_2$ emissions in the 27 Member States of the European Union (EU27). Several measures have been introduced by the European Commission to reduce $CO_2$ emissions from road vehicles, responsible for more than 70% of the transport energy consumption in the EU27. The suggested target to be achieved by 2020 is 95 g($CO_2$)/km.[3] According to the 7th Environment Action Programme (EAP), the EU27 agreed to achieve a reduction of at least 20% of GHG emissions by 2020, to ensure that 20% of energy consumption relies on renewable energy.[4]

Renewable energy sources, such as solar or wind power, are inherently intermittent and, hence, require high efficient energy storage systems to address timely load demand and add flexibility in load management as well as to be competitive with the conventional fossil fuels. In this scenario, the electrochemical energy storage systems play a crucial role and have a significant potential to influence the future fossil-fuel demand in the transport sector and to foster a greater

penetration of the renewable energy. Among these systems, batteries are excellent energy storage technology for the integration of renewable sources in electrical energy systems.[5] Energy return factor and overall energy efficiency are the two key parameters for the choice of suitable battery system for stand-alone power plants. According to the estimation of energy return factors and energy efficiencies carried out for eight different battery technologies used in stand-alone photovoltaic (PV)-battery system,[6] lithium-ion batteries (LIBs) can provide the highest overall battery efficiency with respect to conventional batteries, e.g. lead-acid and Ni-MH, and are also expected to allow high energy return factors. LIBs are also considered the best option as power sources for low-emission electric vehicles (EVs) and hybrid electric vehicles (HEVs).[7] Despite the widespread success in consumer electronics market, the large-scale diffusion of LIBs for EVs and HEVs market is still sluggish. Many improvements in terms of safety, cost, cycle life, power and energy density and faster charge times are still needed to meet the increasing automotive energy demand and, hence, to make EVs and HEVs competitive with the vehicles driven by the conventional internal combustion engine (ICE). The development of advanced rechargeable LIBs is thus one of the most important challenges of modern electrochemistry to make vehicle electrification even more penetrating in worldwide society.

HEVs are based on the synergic combination of an ICE and an electric motor which is powered by a battery system. The wheels of the car are driven by both the ICE and the electric motor. HEVs combine the benefits of high fuel economy and low emissions with the power and range of conventional vehicles. Energy requirements of the battery system highly depend on the level of power-train hybridization and the unassisted electric driving range. There are basically two types of HEVs: power-assist HEVs and plug-in HEVs (PHEVs).

Power-assist HEVs, the most mature technology and already marketed by several car manufacturers, use the battery system during acceleration and braking

and operate in a very dynamic mode, namely charge-sustaining (CS) mode. The battery is used only for short times and kept within an almost constant state-of-charge, since it receives energy pulses from regenerative braking or from the engine. In power-assist HEVs the battery provides an extra-power to the ICE that is kept at a constant power level and auxiliary power when idling. However, in HEVs the primary vehicle-drive power source is still the gasoline.

PHEVs are the next step towards electric mobility because they can enable all-electric driving range (about 10 to 40 miles in current models). PHEVs can operate both in charge-sustaining mode, similar to HEVs, when the battery system reaches a set state-of-charge (SOC), and in charge-depleting (CD) mode with a net decrease of the battery SOC. The battery can be charged by plugging it to an outside electric power source, by the ICE or through regenerative braking like in HEVs.

The fully electric vehicles (EVs) have the highest degree of electrification. They are propelled by one or more electric motors that receive power from the onboard battery that provides more energy than PHEVs. An extended-range EV (EREV) operates essentially like a battery electric vehicle (BEV) for a certain driving range: when the battery is discharged, an ICE powers an electric generator for several hundred kilometres of extended-range driving.[8]

While the power demand for the battery system is almost the same for power-assist HEV and PHEV, the energy demand by the latter is significantly higher since it operates also in charge-depleting mode. The present LIBs can thus widely satisfy the energy demands of HEVs but not those of PHEVs that require the use of high-energy density batteries over 200 Wh $kg^{-1}$ to achieve longer electric-driving range and meet the high energy and power demand of such vehicles. Moreover, the environmental benefits of these types of vehicles increase if they are powered by electricity from renewable sources.

Given that the battery energy ($E$) depends on the capacity ($Q$) and the operating voltage ($V$) of the cell, according to the Equation 1.1:

$$E = V \times Q \tag{1.1}$$

it can be improved by pursuing mainly two strategies. One strategy is the increase of cell voltage by using cathode materials that feature high potentials (> 4.5 V) of $Li^+$ de-insertion/insertion reactions. Another strategy is the increase of cell capacity by using high-capacity cathode materials (e.g. lithium-rich oxides) or developing battery chemistries that can reach specific energy much higher than those of the state-of-the-art LIBs. In particular, lithium-air and lithium-sulfur batteries with theoretical value of 5200 Wh $kg^{-1}$ and of 2500 Wh $kg^{-1}$, respectively, could meet the energy demand of full electric vehicles.[9–11]

## 1.2 Lithium-ion batteries

The operating principle of rechargeable lithium-ion batteries is based on the reversible insertion/ de-insertion of lithium cations between two electrodes with the concomitant electron transfer process (Figure 1.1). During the discharge lithium ions are extracted from the negative electrode and inserted into the positive one; the reverse process takes place during the charge. Such a type of battery was called "rocking-chair battery".[9]

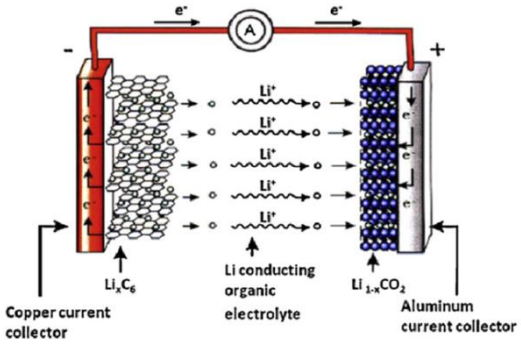


Figure 1.1. Scheme of a commercial lithium-ion battery during discharge. Reprinted from ref. [7], Copyright (2010), with permission from Elsevier.

Most of the commercially available LIBs are based on a graphite anode, a lithium-metal transition oxide cathode, such as $LiCoO_2$ (LCO), and a $Li^+$ conducting electrolyte solution consisting of a lithium salt (e.g. $LiPF_6$) in a mixed organic solvent (e.g. ethylene carbonate–dimethyl carbonate) trapped in a polyolefine membrane as separator.

Although graphite//LCO battery is one of the most widely used lithium-ion battery, it displays an operating voltage of ca. 3.7 V and provides a specific energy of 100-150 Wh $kg^{-1}$ that cannot fulfil the energy and power demand of EVs and PHEVs.[7]

Graphite is so far considered the negative electrode of choice for its appealing properties, i.e. relatively high specific capacity (theoretical value of 372 mAh $g^{-1}$), low average redox potential close to that of lithium metal (0.1 V *vs.* $Li^+/Li$), long cycle life, high-ionic/electronic conductivity, and low cost. Even though its gravimetric energy density cannot be further increased, it is higher than that of any practical cathode material and no cathode with considerably high specific charge (> 400 mAh $g^{-1}$) is yet available;[12] therefore, it is generally accepted by the battery community that graphite electrodes will continue to be the most important and relevant anodes in LIBs for EV applications.[13] Given that cathode materials are the limiting factor for the energy density in lithium battery system, the research efforts are mainly devoted to develop suitable cathodes to improve LIBs' energy and power. The combination of a high-voltage cathode material with a graphite anode should allow full cells with specific energies higher than 200 Wh $kg^{-1}$.

## 1.3 Cathode materials for lithium-ion batteries

Table 1.1 reports capacities and average discharge potentials *vs.* $Li^+/Li$ of several cathode materials for LIBs. The main categories of cathode materials are layered oxides, spinel oxides and phosphates of transition metal.[14,15]

Table 1.1. Capacity and average discharge potential *vs.* $Li^+/Li$ of several cathode materials.

| **Material** | **Practical discharge midpoint potential (V *vs.* $Li^+/Li$)** | **Practical specific capacity (mAh $g^{-1}$)** |
|---|---|---|
| $LiCoO_2$ (LCO) | 3.9 | 150 [12] |
| $LiNiO_2$ (LNO) | 3.8 | 160 [16] |
| $LiNi_{1-x-y}Mn_xCo_yO_2$ (NMC) | 3.7 | 170 [12] |
| $LiNi_{0.8}Co_{0.15}Al_{0.05}O_2$ (NCA) | 3.7 | 200 [12] |
| $LiMn_2O_4$ (LMO) | 4.05 | 130 [12] |
| $LiNi_{0.5}Mn_{1.5}O_4$ (LN05MO) | 4.7 | 130 [12] |
| $LiNi_{0.4}Mn_{1.6}O_4$ (LNMO) | 4.7 | 130 [17] |
| $LiFePO_4$ (LFP) | ~3.45 | 160 [18] |
| $Li_3V_2(PO_4)_3$ (LVP) | 3.8 | 130 [19] |
| $LiMnPO_4$ (LMP) | 4.0 | 150 [20] |
| $LiCoPO_4$ (LCP) | 4.8 | 130 [12] |
| $xLi_2MnO_3 \cdot (1-x)LiMO_2$ (M = Ni, Co and Mn) (LR-NMC) | 3.75 | 225 [12] |
| 0.6 LMP·0.4 LVP | 3.80 | 130 [21] |

Layered oxide materials, pioneered by $LiCoO_2$, feature the $LiMO_2$ structure where M could be Co, Ni, Mn, or a combination of these metals.[22] Because of its very good cycling performance, low self-discharge, $LiCoO_2$ is the most widely used cathode material in LIBs for electronic market. LCO's major limitations are the high cost due to the low cobalt availability, low thermal stability, and fast capacity fading at high currents. In order to overcome these limitations, very crucial for automotive applications, $LiNiO_2$ (LNO) was proposed. However, the LNO's structural instability due to the tendency of $Ni^{2+}$ cations to occupy $Li^+$ sites (similar

ionic radius) during synthesis and/or de-lithiation, thus obstructing $Li^+$ diffusion, led to the development of $LiNi_{1/3}Co_{1/3}Mn_{1/3}O_2$ (NMC) and $LiNi_{0.8}Co_{0.15}Al_{0.05}O_2$ (NCA). Their appealing properties, such as low-cost, high-capacity and good rate capability make NCA and NMC particularly attractive cathode materials for automotive applications. Indeed, NCA is used in Panasonic batteries for Tesla EVs.[12]

The major concern of layered oxide materials is the structural reorganization and, hence, some spinel crystal structure materials, which also enable higher working potentials than layered oxide materials, have been introduced because of environmental friendliness, good safety characteristics, and high power capability.[10] $LiMn_2O_4$ (LMO), which is the most common spinel material in commercial LIBs, displays a working potential of about 4.0 V. It crystallizes in the spinel structure *Fd*-3*m* where Li and Mn cations are located in tetrahedral (8a) and octahedral (16d) sites, respectively, in a cubic close-packed array of oxygen atoms (32e sites).[23] Although LMO shows high rate capability, it suffers from a huge capacity fading due the structural transition from spinel to tetragonal structure caused by the Jahn–Teller distortion of $Mn^{3+}$ ions, and the dissolution of $Mn^{2+}$ ions into the electrolyte. The partly replacement of Mn with other metal ions proved to effectively improve the LMO's performance and the most promising cathode material of this class is the high-voltage $LiNi_{0.5}Mn_{1.5}O_4$ [23] (LN05MO), where the high working potential of approximately 4.7 V *vs.* $Li^+$/Li is due to the reversible oxidation of $Ni^{2+}$ to $Ni^{3+}$ and of $Ni^{3+}$ to $Ni^{4+}$ during lithium de-insertion. The high electronic and $Li^+$ ion conductivities, good rate capability and safety, make it greatly attractive mainly for high-energy density LIBs for PHEV and EV applications. Despite these appealing properties, the major concern that limits the commercialization of these LIBs is the electrochemical instability of the conventional electrolytes towards oxidation at potential higher than 4.5 V *vs.* $Li^+$/Li.

Lithium-transition metal phosphates $LiMPO_4$ (M = Fe, Mn, Co or Ni) with the olivine structure (*Pnma*) were firstly investigated by Goodenough *et al.*[24] Besides

their environmentally friendliness, $LiMPO_4$ materials exhibit high thermal and chemical stability, and low cost. The thermal stability is provided by the strong covalent bond between oxygen and phosphorus ions that makes difficult the removal of oxygen atoms from the lattice. However, the major drawback of these cathodes is the intrinsically low ionic and electron conductivity. Some strategies were thus pursued in order to facilitate their kinetics as Li-insertion electrodes, such as the synthesis of the materials in nanoscale form, the use of carbon layer to coat the particle surface and the doping of the material with a different elements. $LiFePO_4$ (LFP) was the first member of olivine materials, widely investigated and it is now used in commercial LIBs for its excellent rate cyclability and safety features. Moreover, LFP today reaches almost the theoretical specific capacity (170 mAh $g^{-1}$) in real operating conditions. However, the low working potential (~ 3.4 V *vs.* $Li^+/Li$) significantly reduces LFP's energy density on the cell level. Moving to olivine materials containing manganese ($LiMnPO_4$, LMP), cobalt ($LiCoPO_4$, LCP) or nickel ($LiNiPO_4$, LNP), which work at high redox potentials, may improve the cell energy density. However, LNP is not a realistic alternative as cathode material due to its high working potential of 5.2 V *vs.* $Li^+/Li$ and LCP needs of extensive efforts to develop both a reliable synthesis and a suitable electrolyte systems.[13] For these reasons, the current research is devoted to $LiMnPO_4$. It displays the same theoretical capacity of LFP and a working potential of 4.1 V *vs.* $Li^+/Li$ that falls within the electrochemical stability window of conventional electrolytes, making it inherently safer and more stable and attractive than LCP and LNP. Nevertheless, LMP shows poor cycle stability and rate capability due to the low intrinsic electric conductivity, and many issues have still to be solved before LMP becomes the cathode of choice for high-energy lithium-ion batteries for PHEV and EV applications. Several strategies have been proved to enhance LMP's electrochemical performance: the synthesis of nano size particles, the transition metal site or Li-site doping and the carbon coating of the particle surface.[20] More recently, another

strategy was proposed, i.e. the synthesis of a composite material composed of LMP and $Li_3V_2(PO_4)_3$ (LVP). LVP, known for its excellent cycling stability, features a high theoretical specific capacity of 197 mAh $g^{-1}$ when three $Li^+$ ions are reversibly de-inserted/inserted in the potential range 3.6-4.8 V *vs.* $Li^+/Li$. However, it is preferred to limit the charge at potential lower than 4.5 V in order to limit the electrolyte decomposition and to improve cycling stability, thereby consequently decreasing the LVP practical capacity.[19] The LMP-LVP (LMVP) composite material leads to a cathode material that should combine the attractive properties of the single components: the great cycling stability and the rate capability of LVP, which also shows higher conductivity than LMP, and the high and safe working potential of LMP, thus improving the electrochemical performance of the material.[25,26] Even though the LMVP composite material displays greater electrochemical performance than those of pristine LMP, further improvements are needed to achieve a LMP-based cathode with outstanding properties.

Li-rich oxides are also attracting great interest as they display high specific capacity. For instance, $xLi_2MnO_3 \cdot (1\text{-}x)LiMO_2$ (M = Ni, Co and Mn) (LR-NMC) is a notable example of this group of compounds. It displays an average working potential of about 3.8 V and a reversible specific capacity of 225 mAh $g^{-1}$. However, lithium-rich oxides withstand an irreversible capacity loss during the first charge, the so-called "activation", which results in destabilizing structural reorganizations and a partial loss of oxygen from the structure at the surface-near regions of particles. The structure is also exposed to transition metal migration and formation of defective spinel domains which lead to fast capacity fading and gradual voltage decay.[12]

### 1.3.1 High-voltage cathode materials: $LiNi_{0.4}Mn_{1.6}O_4$ and $LiNi_{0.5}Mn_{1.5}O_4$

Spinel $LiNi_{0.5}Mn_{1.5}O_4$ (LN05MO) is one of the most promising high-voltage cathode materials for the development of high-energy lithium-ion batteries for

PHEV and EV applications;[15,23,27,28] in particular, the great interest for the spinel $LiNi_xMn_{2-x}O_4$ ($0 < x < 0.5$) was first highlighted in 1997.[29,30] LN05MO's high nominal operating voltage is due to the reversible oxidation of $Ni^{2+}/Ni^{3+}$ and $Ni^{3+}/Ni^{4+}$ that occurs at 4.70 and 4.75 V, respectively, during the process of $Li^+$ insertion/de-insertion. The high operating voltage and the high theoretical specific capacity of LN05MO (146.7 mAh $g^{-1}$) should enable to provide the highest energy densities among the commercially available cathode materials, e.g. LCO, LMO, LFP and NMC.[23]

LN05MO is also competitive from the point of view of the battery costs. Lithium-ion batteries featuring LN05MO cathodes are the cheapest among LIBs, along with LR-NMC- based batteries,[12] as shown in Figure 1.2.

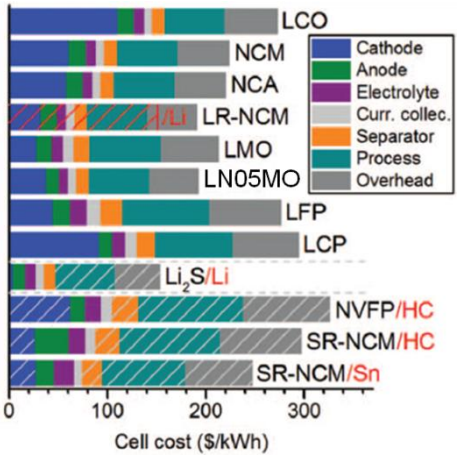


Figure.1.2. Cost estimation on battery cell level: dashed regions indicate rough estimates due to unavailable cost data and notation marked in red denote other negative electrode than graphite. Reproduced with permission from ref. [12]. Copyright 2015, The Electrochemical Society.

Depending on synthesis conditions, $LiNi_{0.5}Mn_{1.5}O_4$ can crystallize in two crystallographic structures: the face-centred spinel (*Fd*-3*m*), namely the disordered spinel, and the cubic phase ($P4_332$), namely the ordered spinel, shown in Figure 1.3. In *Fd*-3*m* disordered phase, Ni and Mn atoms are randomly distributed in 16d sites

with Li and oxygen atoms occupy 8a and 32e sites, respectively. In $P4_332$ ordered phase, Ni and Mn atoms are distributed regularly on 4a and 12d sites, respectively, Li atoms are located in 8c sites, and O atoms in 8c and 24e sites. An order-disorder phase transition can occur by annealing process, associated with a loss of oxygen that lead to the reduction of part of $Mn^{4+}$ ions to $Mn^{3+}$ to keep the electric neutrality. The disordered phase with the oxygen deficiency is usually considered as non-stoichiometric $LiNi_{0.5}Mn_{1.5}O_{4-\delta}$ phase, where NiO and $Li_xNi_{1-x}O$ can also appear as undesired impurities in the final product, and can worsen LN05MO's electrochemical behaviour.[15,23,31]

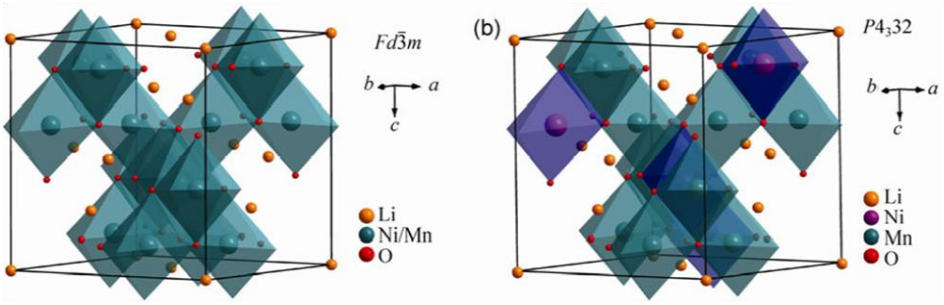


Figure.1.3. Structure of disordered $LiNi_{0.5}Mn_{1.5}O_4$ in *Fd*-3*m* disordered and $P4_332$ ordered phase. Reproduced form ref. [32]. Copyright 2013 with permission of Springer.

The presence of $Mn^{3+}$ affects the electrode performance. Whereas its larger ionic radius with respect to $Mn^{4+}$ results in an expanded lattice that benefits fast $Li^+$ diffusion, $Mn^{3+}$ may lead to the formation of $Mn^{2+}$ via disproportionation reaction: the $Mn^{2+}$ dissolves into the electrolyte, mostly at high temperature, causing important capacity loss over cycling.[31,32] The amount of $Mn^{3+}$ in LN05MO's spinel structure can be quantified by the characteristic plateau in the voltage profile of the $Mn^{3+}/Mn^{4+}$ redox couple at about 4.0 V. However, it is demonstrated that LiN05MO *Fd*-3*m* disordered phase exhibits superior electrochemical performance than the $P4_332$ ordered one.[27,31] This was explained by the investigation of the structural changes that both *Fd*-3*m* and $P4_332$ phases undergo over cycling.[31,33]

During lithium extraction upon charge process, while $LiNi_{0.5}Mn_{1.5}O_{4-\delta}$ (*Fd*-3*m*) undergoes a one-step topotactic phase transition between two cubic phases, $LiNi_{0.5}Mn_{1.5}O_4$ ($P4_332$) undergoes a two-step topotactic phase transition between three cubic phases leading to a much higher strain during cycling, particularly at high rates. The Li extraction in $P4_332$ causes a disordering of the Ni and Mn ions with the structural transformation from $P4_332$ to spinel *Fd*-3*m* of low reversibility at high rates. $P4_332$ thus shows a structure similar to that of *Fd*-3*m* at fully charged state.

Patoux *et al.*[17,34] introduced the disordered $LiNi_{0.4}Mn_{1.6}O_4$ (hereinafter called LNMO) and prepared it without any impurity. Owing to its remarkable electrochemical properties even at high rates, LNMO appeared very attractive for next-generation LIBs. They proposed successful 5 V-high-energy cells by combining the LNMO with graphite anode and 3 V-safe and power cells by combining it with $Li_4Ti_5O_{12}$ anode. In LNMO the oxidation of $Mn^{3+}$ ions at ca. 4.0 V *vs.* $Li^+/Li$ contributes with one fifth to the capacity of the material, and that of $Ni^{2+}$ with four fifth. The $LiNi_{0.4}Mn_{1.6}O_4/Ni_{0.4}Mn_{1.6}O_4$ redox couple also displayed high structural reversibility.

Although LNMO and LN05MO are very attractive and their use as cathode materials in high-energy lithium-ion batteries is feasible, their high operating voltage makes critical the use of conventional carbonate-based electrolytes that are unstable toward oxidation at potentials higher than 4.5 V *vs.* $Li^+/Li$. Since advanced electrolytes are not yet commercially available, great research efforts are devoted to optimize the existing electrolytes or to develop new stable ones, as well to find strategies to develop $LiNi_xMn_{2-x}O_4$ with suitable morphology and enhanced electrochemical performance.

## 1.4 Strategies to improve the interface stability in $LiNi_{0.4}Mn_{1.6}O_4$ and $LiNi_{0.5}Mn_{1.5}O_4$ electrodes

### 1.4.1 Electrolytes and additives for high-voltage cathode materials

The most common electrolyte solution for LIBs is a mixture of aprotic organic solvents, such as ethylene carbonate (EC) with dimethyl carbonate (DMC) and/or diethyl carbonate (DEC), and $LiPF_6$ salt. The choice of proper electrolyte for LIBs has to meet the demand of performance parameters like conductivity, temperature range and electrochemical stability. However, EC:DMC- based electrolytes are not thermodynamically stable and suffer from reductive decomposition on the surface of lithium metal or lithiated graphite. The decomposition products deposit on the electrode surface during the first charge cycle, leading to the formation of a passivation layer, namely solid electrolyte interface (SEI), that prevents further electrolyte reduction while being $Li^+$ conductor and electronic insulator.[9,35] The chemistry of electrolyte solutions significantly affects the nature of the protective film. The commercialization of graphite has strongly influenced the choice of the suitable electrolyte for LIBs, indeed, the combination of the organic solvents, such as EC and DMC, with $LiFP_6$ facilitates the formation of a good SEI on graphite, making LIBs commercially viable.[36]

EC is a mandatory component of the organic solvents due to its unique film formation ability. It decomposes at potentials lower than 1.5 V *vs.* $Li^+/Li$ and forms a protective layer on graphite surface that prevents the co-intercalation of solvent molecules within the graphite bulk and, hence, the graphite exfoliation. The structure and stability of SEI thus strongly influence the new electrode surface and the electrochemical performance of the graphite electrode. Despite the protective role of the surface layers towards the side-reactions with the electrolyte, they could also create a barrier for $Li^+$ ions during charge/discharge cycles causing the increase

of cell impedance and, then, of the capacity fading of the cell.

The surface film formation and related phenomena are generally associated with the anode side, albeit they also involve the cathodic counterpart. The cathode/electrolyte interface, generally referred as "passivation film" or "surface layer", should show the same physicochemical properties of SEI formed on the anode. According to Aurbach and co-workers,[37,38] which widely investigated the nature of electrode/electrolyte interfaces, the reduction process of carbonate-based solvents mainly lead to the formation of $Li_2CO_3$, lithium alkyl carbonates ($RCO_3Li$), lithium alkyl oxide, and of other salt by-products like LiF and P-containing moieties for $LiPF_6$-based electrolytes. The oxidation of EC and DMC cause the formation of new compounds, which include open chain organic carbonates, aldehydes, formates, dimers and oligomers. $CO_2$ and CO can also be formed as co-products. All the formed oxidation products accumulate in the bulk solution. However, during prolonged oxidation which likely develops in Li-ion battery operating condition, it is expected that long chain polycarbonates may be formed and precipitate on electrode surfaces.[39]

Electrolyte is very sensitive to impurities which strongly affect its stability. In particular, $LiPF_6$ which is in equilibrium with LiF and $PF_5$ ($LiPF_6 \leftrightarrow LiF + PF_5$)[40] can react with trace amounts of water present into electrolyte, leading to the formation of HF and $POF_3$ ($PF_5 + H_2O \leftrightarrows 2\ HF + POF_3$).

$PF_5$ is a strong Lewis acid which can lead to the ring opening of EC cyclic carbonate and can also attack the carbonyl oxygen atoms of the linear carbonates because of the higher electron density in those bonds. $PF_5$ may also interact with SEI layer components leading to electronically insulating LiF/alkyl fluoro compounds and gaseous $CO_2$, and, finally, to the crack of the SEI layer. On the other hand, HF and $POF_3$ may cause further solvent decomposition and gas generation, resulting in rapid performance decay of the battery. Therefore, the electrolyte has a significant impact on battery safety as well on thermal stability,

especially in abuse conditions (overheating, overcharging, external short circuiting or crushing). Solvent decomposition causes different gas species including $CO_2$, $CH_4$, $C_2H_4$, $C_2H_5F$, and other subsequent reaction products. All these effects are facilitated at temperatures above 130-150 °C where exothermic chemical reactions between electrodes and electrolyte take place, raising internal temperature of the cell.[41] Chemical reactions are thus accelerated, finally resulting in thermal runaway. Exothermic reactions that trigger thermal runaway may include thermal decomposition of electrolyte, reduction of electrolyte by the anode, oxidation of electrolyte by cathode, thermal decomposition of electrodes, and melting of separator, resulting in internal short circuits. Li-ion electrolytes have been shown to breakdown at temperature of about 150-200 °C and the venting may occur at temperatures as low as 130 °C, strictly depending on the increased vapor pressure. The high rate gas generation usually accompanies the thermal runaway peak (generally 250-350 °C). Gas generation will occur whenever the cell reaches the solvent decomposition temperature, both from internal or external sources. Even the safest cathode and anode chemistries cannot prevent the release of flammable vapors. The volume of gas released from a cell in full thermal runaway is more than that can be contained by any standard cell fixture. In fact, many cell designs purposely allow gases to be released through a designed vent. Accelerating-rate calorimetry measurements using different cathode materials demonstrated that the volume of gas released at the end of the thermal runaway peak (typically 350 °C) was almost 1200 mL/mAh, evaluated from thermal runaway of 18650 cells featuring $LiCoO_2$ (1.20 Ah), $LiNi_{0.8}Co_{0.15}Al_{0.05}O_2$ (0.93 Ah), $Li_{1.1}(Ni_{1/3}Co_{1/3}Mn_{1/3})_{0.9}O_2$, (0.90 Ah), $LiFePO_4$ (1.18 Ah) and $LiMn_2O_4$ (0.65 Ah).[42]

Electrolyte stability issues become particularly crucial when high-voltage cathode materials are involved.[43] As the anodic stability window of conventional carbonate-based electrolytes is lower than 4.5 V *vs.* $Li^+/Li$, they suffer from oxidative decomposition on the fully charged (delithiated) cathode surface at high

potentials, leading to the formation of thick and high resistive surface layers that are detrimental for the cycling performance of the cell. Therefore, there is a significant interest in developing novel electrolyte systems with higher anodic stability, like ionic liquid electrolytes, sulfone- and dinitril-based solvents.[9,44,45] However, the major concerns of these electrolytes are high intrinsic viscosities, low dielectric constant, low conductivities and no formation of SEI on carbonaceous anode materials.

More recently, fluorinated solvents (e.g. monofluoroethylene carbonate $F_1$EC, trifluoroethyl methyl carbonate F-EMC, tetrafluoroethyl tetrafluoropropyl ether F-EPE) were investigated as co-solvents in graphite//LN05MO cells as very promising high-voltage electrolyte systems since they are thermodynamically more stable than their non-fluorinated counterparts under high operating voltages.[45–49] The higher oxidation stability and reduction potential with respect to the conventional electrolytes result from the fluorine substitution that lowers both HOMO and LUMO levels, since the electrochemical stability window of electrolyte is the difference between the lowest unoccupied molecular orbital (LUMO) and the highest occupied molecular orbital (HOMO) of the electrolyte. Therefore, graphite//LN05MO cells displayed enhanced cycling performance than those of cells with conventional electrolytes even at elevated temperature.

Another interesting approach is the substitution of $LiPF_6$ with fluorinated salts, such as < (LiFAP) in alkyl carbonates. The replacement of fluorine atoms of $LiPF_6$ with electron withdrawing perfluorinated alkyl groups leads to stabilize P-F bonds. Therefore, LiFAP is more stable than $LiPF_6$ towards hydrolysis and, thus, should contain less HF contamination; moreover, it displays a conductivity comparable to $LiPF_6$ and an improved thermal stability.[50–53]

An alternative and economically effective approach to develop electrolyte systems with enhanced stability towards oxidation reactions is the incorporation of an additive into carbonate-based electrolytes, in order to form a passivation layer on

cathode surface, thus stabilizing the cathode/electrolyte interface upon high-operating voltages. This should inhibit further oxidative reactions between cathode and electrolyte.[54,55] The use of additives was firstly investigated in graphite electrodes, and later it was extended to the cathode counterpart to prevent its performance deterioration mainly due to water and acidic impurities, and to irreversible oxidization of the electrolyte solvents, which is particularly accelerated when high-voltage cathode materials are involved. An electrolyte additive (commonly no more than 5 wt.%) should exhibit suitable properties to effectively improve the cyclability and cycle life of LIBs by forming a stable protective layer on both anode and cathode surfaces, reducing irreversible capacity and gas generation due to the SEI formation and long-term cycling, enhancing chemical stability of $LiPF_6$ against the organic electrolyte solvents, protecting the cathode material from dissolution and overcharge, and improving physical properties of the electrolyte, i.e. ionic conductivity, viscosity and wettability to the polyolefine separator.[54]

Recent studies have demonstrated that electrolyte additives effectively improve the electrochemical performance of LN05MO and LNMO-based cells. Lithium bis(oxalato)borate (LiBOB) was investigated as additive in Li/LN05MO cells as it forms a thin protective layer which inhibits the detrimental reactions of the electrolyte with the cathode surface, thus improving the cycling efficiency and capacity retention of the cell and decreasing cell impedance.[56] Moreover, LiBOB could prevent the generation of HF or $PF_5$ and inhibit the dissolution of Mn or Ni from the cathode surface. Tris(hexafluoro-iso-propyl)phosphate is another effective additive as it is involved in forming a protective layer not only on LN05MO surface but also on graphite electrode, making it possible the development of an electrolyte system that supports reversible $Li^+$ intercalation in the 5 V region.[57] Glutaric anhydride, which was investigated as electrolyte additive in $Li_4Ti_5O_{12}$//LNMO cell, significantly reduced both the capacity fading and the self-discharge and formed a

passivation film like a polymer electrolyte interface at the surface of both electrodes.[58]

Lee *et al.*[59] demonstrated the beneficial effect of succinic anhydride and 1,3-propane sultone as SEI-forming electrolyte additives in 1M $LiPF_6$ EC:EMC (1:2 hgv/v) on electrochemical performance of graphite//LN05MO cells. Moreover, succinic anhydride was lately proved to effectively reduce the self-discharge of LNMO based electrodes, which, in turn, showed enhanced coulombic efficiency and decreased capacity loss per cycle.[60]

### 1.4.2 Particle size

The high reactivity of fully charged LN05MO towards the carbonate-based electrolytes lead to a reactive electrode/electrolyte interface that is greatly affected by the LN05MO's morphology (particle size, shape and surface area). The proper combination of particle size and shape of LN05MO make it possible to improve the cycling performance of the electrodes as demonstrated in ref. [32]. The matching of micro-sized particles in disordered phase with nano-sized ones in ordered phase appeared the best combination to achieve a spinel material with both high rate capability and cycling performance. Despite nano-sizing can dramatically shorten $Li^+$ diffusion paths by improving the lithiation/de-lithiation kinetics, the high surface area permits high electrode/electrolyte contact thus increasing the interfacial side-reactions, which lead to undesirable capacity loss over cycling. In disordered LN05MO the presence of $Mn^{3+}$ results in a $Li^+$ diffusion because the larger radius of $Mn^{3+}$ than that of $Mn^{4+}$ is responsible of an expanded lattice. On the other hand, $Mn^{3+}$ ions can induce Jahn-Teller distortion and manganese dissolution into electrolyte, resulting in a detrimental effect for the cycling stability of the electrode. However, by using micro-sized particles, the unwanted reactions with the electrolyte are reduced since the surface area is lower than that of nano-sized particles.

### 1.4.3 Surface modification

One of the most effective strategy to improve the stability of LN05MO's electrodes is the surface modification by coating.[27] Nano-sized ZnO-coating was demonstrated to greatly improve the electrochemical performance of LN05MO as it protects the cathode surface against the HF attack and prevents the Mn dissolution into electrolyte, thus increasing the structural stability of the spinel material.[61] $SiO_2$-coating also enhanced the cycling stability of LN05MO, by lowering HF content into electrolyte and LiF content on the cathode surface.[62] Thin $Li_3PO_4$-based films deposited on LN05MO surfaces in solid-state lithium batteries significantly affected the interface properties, as $Li_3PO_4$ avoids the supply of $O^{2-}$ ions from the cathode during the charge process, thus preventing the oxidation of polymer electrolyte and improving both the performance and the safety of the battery system.[63] The thin protective layers of $V_2O_5$,[64] of $TiO_2$ or $Al_2O_3$ deposited on LN05MO by atomic layer deposition as reported in ref. [65], effectively prevent the electrolyte decomposition and Mn dissolution in LN05MO based electrodes, thus improving the discharge capacity retention over cycling.

### 1.4.4 Reduced graphene oxide as additive in $LiNi_{0.5}Mn_{1.5}O_4$-based electrodes

The outstanding properties of graphene make it great interesting and promising material for the use in electrochemical energy storage applications.[66] Recently, it was also explored as efficient conductive additive in cathode materials for LIBs.[67,68]

Graphene is a two-dimensional material that displays a honeycomb lattice structure and comprises a monolayer of graphite consisting of $sp^2$ hybridized carbon atoms. It composes the basic structure of carbon materials such as graphite, carbon nanotubes and fullerenes. The properties of graphene are strongly affected by the methods used for its production. While the micromechanical exfoliation of highly

oriented pyrolytic graphite and chemical vapour deposition of hydrocarbons are unsuitable for mass-production of graphene for electrochemical energy storage being both highly expensive methods, liquid-phase exfoliation and reduction of graphene oxide are the most widely employed methods for its bulk production.[69] In particular, the latter is the method most common used to prepare graphene-based cathode materials for LIBs. Graphene oxide (GO), produced by strong oxidation of pristine graphite, is a monolayer of a graphite oxide electrically insulating due to its disrupted $sp^2$-bonding networks. The graphene characteristic $\pi$-network is partially restored when GO is reduced via chemical, thermal and electrochemical processes, thus obtaining the reduced graphene oxide (RGO), or simply called graphene.[67] The hydrophilic oxygen-containing functional groups that remain on graphene surface after its reduction provide anchor sites for the consequently adhesion of active material particles on surfaces and edges of GO sheets. The physical and electric contact between the graphene and the active material is crucial for the development of graphene-based cathode material with high electrochemical performance.[66,67]

More recently, reduced graphene oxide was also proposed as conductive additive in LN05MO electrodes.[70,71] It can act as surface layer that protects the cathode against the interfacial side-reactions, and can suppress the electrolyte decomposition over cycling. RGO's coating also enhances the electronic conductivity of the electrode, thus reducing the cell resistance and allowing LN05MO electrodes with improved rate capability. In ref. [71], a graphene-sandwiched LN05MO structure was proposed. LN05MO nanoparticles are well interconnected with each other by graphene layers via the residual oxygen functionalities on the basal plane of partly reduced graphene oxide (pRGO). This structure, schematized in Figure 1.4, permits an efficient conducting network that lowers the electrode polarization, thus enhancing the coulombic efficiency and, hence, the capacity retention over cycling. Moreover, pRGO coating also

suppresses the manganese dissolution, thus improving the cycling stability of the electrode.[70,71]

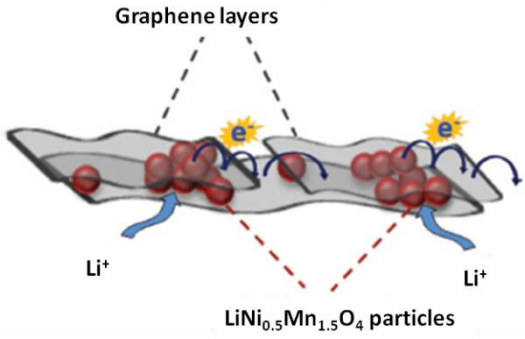


Figure 1.4. Schematic structure of graphene-sandwiched LNMO. Reproduced with permission from ref. [71]. Copyright 2013, The Electrochemical Society.

### 1.4.5 Separators

Separator is an important component in LIBs for cell energy and power densities and cycle life, and crucial for cell safety.[72,73] It is basically a thin porous membrane that separates the anode from the cathode while enabling the ionic transport and isolating electronic flow in the cell. Separator must be chemically and electrochemically stable towards both electrodes and electrolyte in order to provide a good interface between them, especially under strong reductive and oxidative environments when the battery is fully charged, or in presence of high-voltage cathode materials. It should also display high mechanical strength to withstand the tensions during the battery assembly and a proper porosity to assure good electrolyte absorption and retention, needed for good ionic conductivity between the electrodes. However, separators add electrical resistance to the cell and, hence, could adversely affect the battery performance.

Tortuosity, pore size and permeability of separators are key properties. Tortuosity ($\tau$), a long-range property of porous medium, is the ratio of mean effective capillary length to separator thickness, according to Equation 1.2:

$$\tau = \frac{I_s}{d} \tag{1.2}$$

where $I_s$ is the ion path through the separator and $d$ the thickness of the separating layer.[72] An appropriate tortuous structure of pores is desirable in regard to lithium dendrites. Tortuosity strictly depends on pore size that must be smaller than that of active electrode materials and of conductive additives to avoid them to penetrate into separator and to reach the opposite electrode. A homogeneous distribution of pores is crucial to provide an uniform current distribution and avoid capacity losses. Basically, sub-micrometric pores are critical for preventing short-circuits and commercial LIB separators usually display approximately 40% porosity.[72] Moreover, pore size and porosity of separator strongly affect the ionic conductivity of the liquid electrolyte and, hence, the electrochemical response of the battery.

The presence of the separator basically reduces the ionic conductivity of the electrolyte ($\sigma_0$) by a factor of 4-5 and the so-called MacMullin number ($N_M$) relates the effective conductivity ($\sigma_{eff}$) of a porous network, to $\sigma_0$, according to Equation 1.3:[74,75]

$$N_M = \frac{\sigma_0}{\sigma_{eff}} \tag{1.3}$$

MacMullin number should be as low as possible for high power and energy density LIBs for HEVs applications in order to assure high rate capability. Pore structure is inherently linked to the permeability that can be estimated as air permeability via the Gurley number, i.e. the time required for a specific amount of air to pass through a specific area of the separator under a specific pressure.[72]

Separator is also used as internal safety device of battery in abuse conditions when overheating occurs due to occasional short circuits or overcharge. It may

protect the cell via the shutdown behaviour: as the temperature of the cell increases, it melts to close the pores thus resulting in a large increase of impedance that stops ions transport and, then, the current flow. This permits to avoid the thermal runaway whether the separator still maintains the mechanical integrity to prevent the physical contact between the two electrodes.[72,76–78]

Most of separators available on the market are single or multilayer sheets based on microporous polyethylene (PE) or polypropylene (PP). The current separators are approximately 25 μm thick. PE–PP bilayer and PP–PE–PP trilayer separator are the most widely used. In multilayer separators each layer has different phase transition, hence, different shutdown behaviour. For instance, in PE-PP bilayer separators as the cell temperature increases, PE layer melts at 130 °C and fills the pores of PP layer blocking ion transport and current flow, followed by PP melt at 155 °C.[76]

On the basis of structure and composition, separators can be mainly divided into microporous polymer membranes, non-woven fabric mats and inorganic composite membranes. Two are the processes for making lithium-ion battery separators: dry and wet processes.[73] Both processes comprise an extrusion step followed by a mechanical stretching process to induce porosity. While the dry process is applicable only to polymers with high crystallinity and provides tightly ordered micropores, the wet process is applicable to both crystalline and amorphous polymers and provides a non-oriented membrane.

The optimization of all separator's properties is of great importance to develop a suitable separator, particularly for high power and energy densities lithium-ion batteries, for which very thin, mechanically robust and highly porous membranes, stable at potentials higher than 4.5 V *vs.* $Li^+/Li$, are highly demanded.[73]

Poly(vinylidene fluoride) (PVdF) and its copolymer have attracted great interest as separators for LIBs because of their much more appealing properties than those of commercial polyolefine separators, such as high polarity that allows high affinity

with polar conventional electrolytes like those based on EC:DMC.[79,80] PVdF-based separators are most commonly prepared by phase inversion process or electrospinning.

Phase inversion process mainly comprises the dissolution of the polymer into a solvent and the casting of the resulting viscous solution onto a flat substrate to form a thin polymer layer. After the evaporation of the solvent, the film is thus immersed in a non-solvent coagulation bath to induce the phase inversion; the exchange between the solvent and non-solvent makes it possible the formation of pores into membrane.[73]

Electrospinning is an alternative, efficient and simple method for the versatile and scalable production of fibrous mats of various polymers with submicrometric or nanometric diameters. The method is based on the interaction between a charged fluid, like a polymer solution or melt, and a strong electric field (ca. 1 - 25 kV $cm^{-1}$) leading to the formation of a structure, namely Taylor cone, at the nozzle tip from which the charged jet is ejected when the electrical forces overcome the surface tension and viscosity of the fluid. Then, as the solvent evaporates during the motion, a solid non-woven fibre mat is deposited on the target collector.[81–83]

Lithium-ion batteries featuring PVdF-based membranes were first reported by Tarascon *et al.*[84] and later by Boudin *et al.*[85] They proposed a gel polymer electrolyte where the liquid electrolyte was embedded in a PVdF-based polymer matrix. This solid lithium-ion battery showed electrochemical performance similar to those of conventional liquid lithium-ion batteries, while displaying higher shape flexibility and scaleability. Moreover, one of the main advantages of fluorinated PVdF-based separators is their ability to adapt to different geometries, even in very thin cells.[84–86]

Macroporous PVdF membrane was proposed as effective separator in $Li_4Ti_5O_{12}$//$LiMn_2O_4$ cell that showed high rate capability thanks to the good electrode/electrolyte contact promoted by the good affinity between PVdF and

organic solvents, thus enabling a better wettability with respect to the commercial polyolefine separators.[87] Despite the strong affinity of PVdF-based separators with polar solvents, PVdF can suffer from swelling that sharply decreases mechanical properties and may modify the electrode/electrolyte interface resulting in membrane dissolution, even compromising battery safety. A proper combination between salt and solvent mixture is thus important to assure good affinity between electrolyte and PVdF membrane, as well its good wettability and long-term stability.[88–90] The reinforcement of PVdF-based separators with nanosized particles has also been suggested as effective strategy to enhance their mechanical properties. In particular, the blending of PVdF with nanocrystalline cellulose whiskers (NCC), based on highly crystalline rod-like particles with high aspect ratio and surface area, can greatly improve its mechanical stability. NCC thus provides a rigid network through hydrogen bonds between each adjacent whisker involving surface -OH groups.[91,92]

### 1.4.6 Binders for high-voltage cathode materials

Binders, even though electrochemically inactive, are also crucial battery components that provide mechanical cohesiveness during battery operation and affect electrode properties via surface modification. The main role of binder is holding together the electrode components, thereby preventing their chemical and mechanical disintegration during cycling. The particles can be bound via direct or indirect binding as shown in Figure 1.5. The direct binding is typical of elastomers which contact quite a small surface area of each particles; this assures good binding while giving flexibility to the electrode since the binder can absorb the expansion and the contraction of the active material during charge/discharge cycles, thereby improving battery's cycle life. By contrast, in the indirect binding the binder contacts a larger surface area thus strongly influencing the electrode flexibility and battery's cycle life.[93,94]

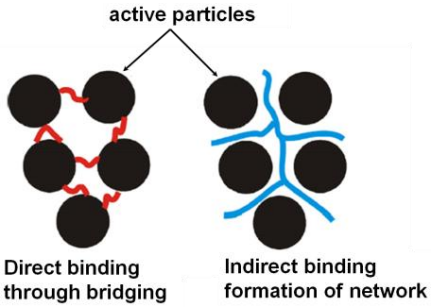


Figure 1.5. Binding models in composite electrodes. Reprinted from ref. [93], Copyright (2008) with permission from Elsevier.

The binder is also the key factor in determining the choice of the solvent for electrode preparation, thereby the overall processing sustainability. PVdF is the most commonly employed binder in LIB cathodes as it shows good electrochemical stability and binding strength. However, it is costly and requires the use of an expensive and highly toxic organic solvent, i.e. *N*-methyl-2-pyrrolidone. Therefore, many efforts are aimed at the development of fluorine-free binders easily processed in water. The use of water-soluble binders for LIBs is a very effective and eco-friendly approach. Several natural and naturally derived polymers were thus proposed, such as sodium carboxymethyl cellulose (CMC),[93,95] alginate,[96] chitosan,[97] polyvinyl acetate.[98] Besides their low cost and environmentally friendliness, water-soluble binders enable the increase of the active material in the composite electrode. These binders have also been proved to enhance the cyclability of alloying anodes, by assuring a good contact among particles even when they undergo large volume expansion.

CMC (Figure 1.6) is one of the most interesting water-soluble binders. CMC's environmentally friendliness and low cost (1-2 € $kg^{-1}$, one order of magnitude less than PVdF) make appealing its use in LIBs. The employment of CMC binder would contribute to a much easier end-of-life disposability due to the absence of fluorine in the binder. In fact, once the electrode is extracted from the cell, the active

electrode material can be easily recovered by pyrolysis of the binder. Therefore, the introduction of CMC as binder could be a critical step for the improvement of the electrode preparation and the development of greener and cost-effective lithium-ion batteries.[99]

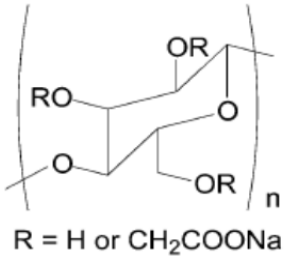


Figure 1.6. Molecular structure of carboxymethyl cellulose.

The advantage of using CMC binder was also proved by the enhanced electrochemical performance of both negative [100,101] and positive electrodes [94,102] with regard to those with PVdF. Recently, the use of CMC binder was demonstrated to efficiently improve the cycling stability of high-voltage cathode materials, such as $Li_2MnO_3$–$LiMO_2$,[103] $LiNi_{0.4}Mn_{1.6}O_4$ [104] and $LiNi_{0.5}Mn_{1.5}O_4$.[105]

CMC is a linear polymeric derivative of natural cellulose, comprising β-linked glucopyranose residues with different levels of carboxymethyl substitution, i.e. -$CH_2COO^-$ groups which are responsible of the aqueous solubility of CMC with respect to the insoluble cellulose. The degree of substitution (DS) is most commonly in the range of 0.60-0.95 derivatives per monomer unit. DS is a key factor in determining the hydrophobicity of CMC, thereby influencing its interaction with the active material particles as demonstrated by Lee *et al.*[106] for graphite electrodes. CMC can promote the formation of homogenous three-dimensional network between the conductive additive and active material particles, leading to tight and homogeneous electrode architecture, thereby decreasing the electrode polarization and the charge-transfer resistance.[107] The homogeneous

network is formed when CMC is dissolved in water where adopts a fully stretched molecular conformation, due to the backbone rigidity and the electrostatic repulsive interactions between ionized carboxy lateral groups.

## 1.5 Aim of the thesis

The aim of this PhD work was the development of high-energy and high-power lithium-ion batteries (LIBs) featuring high-voltage $LiNi_{0.4}Mn_{1.6}O_4$ (LNMO) and $LiNi_{0.5}Mn_{1.5}O_4$ (LN05MO) cathode materials, mainly for HEV applications. Starting from the challenging study focused on some cell components, such as electrolyte, separator, conducting additives and binder for cathode materials, whose selection is greatly important when high-voltage cathodes are involved, full cells with graphite anode were assembled and tested according to the U.S. Department of Energy protocols in view of the use of LNMO and LN05MO in LIBs for HEV and plug-in HEV applications. In particular, LNMO was investigated in the frame of FP-7 European Project (Transport), "Advanced Fluorinated Materials for High Safety, Energy and Calendar Life Lithium Ion Batteries" (AMELIE) and synthesized by Commissariat à l'énergie atomique et aux énergies alternatives (CEA) - Le Laboratoire d'Innovation pour les Technologies des Energies nouvelles et les Nanomatériaux (LITEN) (Grenoble, FR, Partner of EU-AMELIE Project), the latter, a commercial material, was investigated under Italian Programme Agreement "Electrical System Research" supported by Italian National Agency for New Technologies, Energy and Sustainable Economic Development (ENEA) and the Italian Ministry of Economic Development (MSE). Part of the research was also carried out at Helmholtz Institute Ulm (HIU) (Ulm, DE) supported by the Marco Polo Exchange Programme and Karlsruhe Institute of Technology (KIT) under the supervision of Prof. Dr. Stefano Passerini.

# Chapter 2. Experimental section

Chapter 2 deals with materials and methods used for the study of $LiNi_{0.4}Mn_{1.6}O_4$ (LNMO) and $LiNi_{0.5}Mn_{1.5}O_4$ (LN05MO) cathodes electrochemically characterized in half cell *vs.* Li and in full cells with graphite anode.

## 2.1 Chemicals

The $LiNi_{0.4}Mn_{1.6}O_4$ (LNMO) active material with the cubic crystal structure *Fd*-3*m* was synthesized by Commissariat à l'énergie atomique et aux énergies alternatives (CEA) - Le Laboratoire d'Innovation pour les Technologies des Energies nouvelles et les Nanomatériaux (LITEN) (Grenoble, FR, Partner of AMELIE Project) via high-temperature solid-state synthesis, as described in refs. [17,34]. The precursors were $MnCO_3$, $LiCO_3$ and $NiCO_3 \cdot 2Ni(OH)_2$, mixed in stoichiometric proportions by wet ball milling in hexane. The mixed powders were thermally treated at 60 °C for 10 h and annealed at 900 °C for 15 h, followed by the cooling step at 1 °C $min^{-1}$. The resulting powders were thus stirred in aqueous solution for 48 h in order to separate the agglomerated particles.

$LiNi_{0.5}Mn_{1.5}O_4$ (NANOMYTE® SP-10, LN05MO) from NEI Corporation displays a cubic crystal structure *Fd*-3*m* with a grain size of 300 nm and average particle size of 5 μm, surface area of 2-3 $m^2\ g^{-1}$ and tap density of 1.0-1.5 g $cm^{-3}$.

Graphite electrodes were based on commercial graphite powders: FormulaBT™ SLA-1025 graphite (BET surface area of 1.5 $m^2\ g^{-1}$, particle size $d_{90}$ of 29.9 μm) from Superior Graphite Co., and SLP 30 graphite (BET surface area 7.0 $m^2\ g^{-1}$, particle size $d_{90}$ of 32 μm) from Imerys. SLA-1025 graphite electrodes of low- and high-mass loading were prepared by Kiev National University of Technologies and Design (KNUTD) and by CEA-LITEN, respectively, both Partners of EU-AMELIE

Project. SLP 30 graphite electrodes were prepared at Münster Electrochemical Energy Technology (MEET, DE).

Binders used for the electrode preparation were polyvinylidene fluoride (PVdF) and sodium carboxymethyl cellulose (Na-CMC), i.e. PVdF Solef®5130 and Solef®5320 from Solvay, PVdF Kynar HSV 900 from Arkema, and CMC Walocel™ 2000 PPA12 with a degree of substitution of 1.2 from Dow Wolff Cellulosics. *N*-methyl-2-pyrrolidone (NMP, Fluka, purity grade > 99%) and deionized water were used to dissolve PVdF and CMC, respectively.

Different nanometric carbon blacks were used as electrode conducting additives: C-NERGY™ Super C65 (C65, Imerys), Super P (SP, Erachem) and PureBLACK™ (Superior Graphite, Co.) with PVdF binder and C-NERGY™ Super C45 (C45, Imerys) with CMC binder. C65 and SP feature almost the same particle size (40 nm), BET area (62 $m^2$ $g^{-1}$), absorption stiffness (AS) value (32 mL $5g^{-1}$) and resistivity (0.2 ohm cm). C45 features the same particle size and resistivity of C65 and SP while differing for BET area (45 $m^2$ $g^{-1}$) and AS value (36 mL $5g^{-1}$). All the given value are from data sheets. C45 is recommended for aqueous solutions. Reduced graphene oxides were also used as conducting additives in LN05MO composite electrodes: a home-made prepared partially reduced graphene oxide (pRGO), obtained by microwave (MW) irradiation of graphene oxide (GO, NanoInnova) in a CEM Discover MW oven,[108] and a commercial reduced graphene oxide (RGO, NanoInnova). The LN05MO composite electrodes with pRGO always contained carbon C65 or SP in a 1 : 1.4 weight ratio. The LN05MO powder was coated by pRGO before its mixing with the other components. The coating was carried out by moderate stirring of a suspension of LN05MO and pRGO powders in anhydrous ethanol, at room temperature and then at 45 °C to evaporate all the solvent, as in ref. [70]. The LN05MO composite electrodes containing RGO and C65 (1 : 1 w/w) or RGO alone were obtained by dry mixing of the components.

Carbonate-based electrolytes used in electrochemical cells were 1 M $LiPF_6$ in ethylene carbonate (EC) : dimethyl carbonate (DMC) (1:1) (LP30, BASF) and 1M lithium tris(pentafluoroethyl)trifluorophosphate (LiFAP) in EC:DMC (1:1) (LF30, BASF). In both LP30 and LP30 the water content was ≤ 20 ppm and HF content ≤ 50 ppm. Mono-fluoroethylene carbonate ($F_1$EC, Solvay Fluor, purity ≥ 99.9 wt%, water and HF content ≤ 20 ppm) and succinic anhydride (SA, Sigma-Aldrich, purity ≥ 99%) were used in proper amount as additives in LP30 and LF30 electrolytes: 1.6 wt.% $F_1$EC and 2 wt.% SA. Both were used as received. While SA was added to electrolyte LP30 and LF30 to protect the cathode, $F_1$EC was added as SEI forming for graphite electrode.

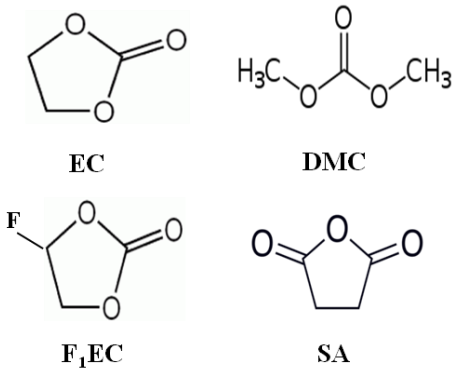


Figure 2.1. Structures of EC, DMC, $F_1$EC and SA.

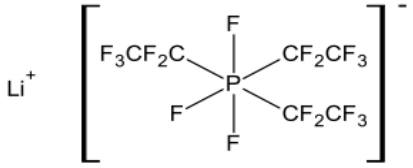


Figure 2.2. Structure of lithium tris(pentafluoroethyl)trifluoroposphate (LiFAP) salt.

## 2.2 Equipments for chemical-physical characterizations

X-ray diffraction analyses (XRD) were performed by a PANalytical X'Pert PRO powder diffractometer equipped with a X'Celerator detector (CuKα radiation, 40 mA, 40 kV).

The differential thermal analysis (DTA) of dry separators was carried out with a Linseis L6310 and the thermo-gravimetric analyses (TGA) with a TA Q50 balance in argon atmosphere.

Scanning electron microscopy (SEM) measurements were performed with Zeiss EVO 50 at University of Bologna and Zeiss LEO 1550 at Helmholtz Institute Ulm, both equipped with an energy dispersive X-ray analyzer; the former from Oxford INCA Energy 350 system and the latter from Oxford Instruments X-Max$^N$ (50 mm$^2$). Transmission electron microscopy (TEM) images were performed with a Philips CM100 (accelerating voltage 80 kV).

Fourier Transform Infrared Spectroscopy (FTIR) analysis was carried out using a Bruker Alpha spectrometer on grind materials scraped off electrodes and mixed with KBr.

X-ray photoelectron spectroscopy (XPS) measurements performed on LNMO based electrodes were carried out at Münster Electrochemical Energy Technology (MEET) Battery Research Centre (in the frame of AMELIE Project) with the Axis Ultra HSA spectroscopy (Kratos) using a monochromatic Al Kα source, at 10 mA and 12 kV source energies. To compensate the charging of the sample the charge neutralizer was used. Calibration of the binding energy (BE) of the measured spectra was performed by usage of the energy of the C1s graphite peak (CC at BE = 284 eV) as an internal reference. XPS measurements were performed on pristine cathodes as well as after charge/discharge cycles. The half cells were disassembled in an argon-filled dry-box and electrodes were analyzed without rinsing to prevent inequality. The samples were transferred to the spectrometer using sealed vials in order to avoid air/moisture contamination. Residual electrolyte was removed by

applying ultra-high vacuum overnight before XPS characterization.

XPS measurements on LN05MO-CMC electrodes were performed at Ulm University by Physical Electronics "PHI 5800 ESCA System" using a monochromatized Al Kα radiation (15 kV, 250 W) and a Mg Kα radiation (13 kV, 200W) to measure Ni 2p and Mn 3s. The charging of the sample was neutralized with an electron flood gun and all XPS spectra were calibrated to the signal of C 1s at 284.5 eV.

## 2.3 Electrode preparation

Table 2.1 reports active materials, conducting additives and binders used for electrode preparation.

Table 2.1. Components for electrode preparation.

| | |
|---|---|
| **Positive active materials** | $LiNi_{0.4}Mn_{1.6}O_4$, $LiNi_{0.5}Mn_{1.5}O_4$ |
| **Negative active materials** | SLA-1025 graphite, SLP 30 graphite |
| **Conducting additives** | carbon blacks Super P, Super C65 and PureBLACK™; pRGO and RGO |
| **Binders** | PVdF Solef®5130, PVdF Solef®5320, PVdF Kynar HSV 900, Na-CMC |

LNMO composite electrodes were prepared by MEET in the frame of AMELIE Project featuring 85 wt.% of active material, 10% of carbon black Super C65 conductive additive and 5% PVdF binder (Solef®5130). The disk electrodes (0.636 $cm^2$ and 1.13 $cm^2$), pressed at 1500 psi for 1 min, were dried at 120 °C under dynamic vacuum for 12 h before use. The active material mass loading was in the range of 7-15 mg $cm^{-2}$.

LN05MO composite electrodes were prepared by a lamination technique by mixing 85 wt.% active material, 5% PVdF binder (Kynar HSV 900) and 10% total carbon conducting additive (Super C65 or Super P and/or pRGO or RGO) using

NMP as solvent. The slurries were prepared by a planetary ball milling (Planetary Mill Pulverisette 6, Fritsch) at 250 rpm or by a IKA Ultra-Turrax. The resulting slurries were coated on 10 µm thick aluminum foil current collector by using a lab-scale mini coating machine (MC 20, Hohsen Corp.) and pre-dried at 60 °C for two hours in air conditions. In order to promote a better adhesion of the slurry to the current collector, aluminum foils were previously etched by immersion in 5 wt.% KOH at room temperature for one minute, subsequently washed in deionized water and dried at 60 °C. Disk electrodes (0.636 $cm^2$, active material mass loading in the range of 2-10 mg $cm^{-2}$) were punched and pressed at 2500 psi for 1 minute (ICL-12, Ton EZ-Press) and, finally, dried at 120 °C under dynamic vacuum in a glass oven (Büchi B-580) for 12 h before use.

The aqueous processing of LN05MO electrodes was carried by mixing 85% LN05MO, 5% CMC binder and 10% Super C45 conducting additive. CMC binder was previously dissolved in deionized water by magnetic stirring at 200 rpm for 2 h. Subsequently, ball milling (Vario-Planetary Mill Pulverisette 4, Fritsch) or magnetic stirring were used for the making of slurries. In the first case, after CMC dissolving, the active material and the carbon additive were added to the solution and ball milled together at 250 rpm for 3 h. In the second case, C45 was added to the binder solution and dispersed by magnetic stirring for 2 h. Subsequently, LN05MO was added and further mixed by magnetic stirring for 2 h, followed by a high speed mixing (Dremel) for 10 min at 5000 rpm. The magnetic stirring procedure was also used for the preparation of LN05MO-PVdF electrodes to compare their electrochemical performance with that of CMC-based electrodes. All slurries were casted on Al foil current collector (20 µm) with a laboratory doctor blade coater (Olbrich). Disk electrodes (1.13 $cm^2$, active material mass loading in the range of 4-10 mg $cm^{-2}$) were punched and pressed at 2500 psi for 1 min. Finally, CMC- and PVdF-based electrodes were dried at 180 °C and 120 °C, respectively, under dynamic vacuum in a glass oven for 12 h before use.

SLA-1025 graphite electrodes featuring 89 wt.% active material, 3% PureBLACK™ conducting additive and 8% PVdF (Solef®5130 or Solef®5320) were prepared and roll pressed by Kiev National University of Technologies and Design in the frame of AMELIE Project. Disk electrodes (0.636 $cm^2$) were dried at 120 °C under dynamic vacuum for 12 h before use. The active material mass loading was in the range of 2.5-5.5 mg $cm^{-2}$. SLP 30 graphite electrodes featuring 90 wt.% active material, 5% Super C45 and 5% CMC were prepared by using the battery line at MEET. Disk electrodes (1.13 $cm^2$, active material mass loading in the range of 3.0-4.0 mg $cm^{-2}$) were punched and pressed at 1000 psi for 30 s and dried at 180 °C under dynamic vacuum for 12 h before use.

LNMO and SLA-1025 graphite composite electrodes of electrode formulation and loading optimized for the scale-up of batteries for HEVs applications were also tested. They were prepared by CEA-LITEN by using the battery line, roll pressed and provided in the frame of AMELIE Project. The positive electrode composition was 92 wt.% LNMO, 4% Super C65 conductive carbon and 4% PVdF binder (Solef®5130). The negative electrode composition was 91% graphite, 3% PureBLACK™ conducting additive and 6% PVdF (Solef®5130). The active material mass-loading for single-face electrodes was 21.0-21.5 mg $cm^{-2}$ for the positive and 8.5-9.5 mg $cm^{-2}$ for the negative electrodes. Disk electrodes (0.636 $cm^2$) were dried under dynamic vacuum at 120 °C for 12 h before use.

## 2.4 Electrochemical characterization

### 2.4.1 Tests of $LiNi_{0.4}Mn_{1.6}O_4$ and $LiNi_{0.5}Mn_{1.5}O_4$ composite electrodes in half and full cells

All the electrochemical tests were performed in three-electrode mode configuration in T-shaped BOLA (Figures 2.3a) and Swagelok (Figure 2.3b)

electrochemical cells using LNMO or LN05MO as working electrode and Li metal as reference electrode. Li in excess and graphite anode with balanced capacity were used as counter electrodes in half and full cells, respectively. The electrode mass balancing in the full cells was made by setting the ratio of the capacity of the negative to that of the positive near 1.

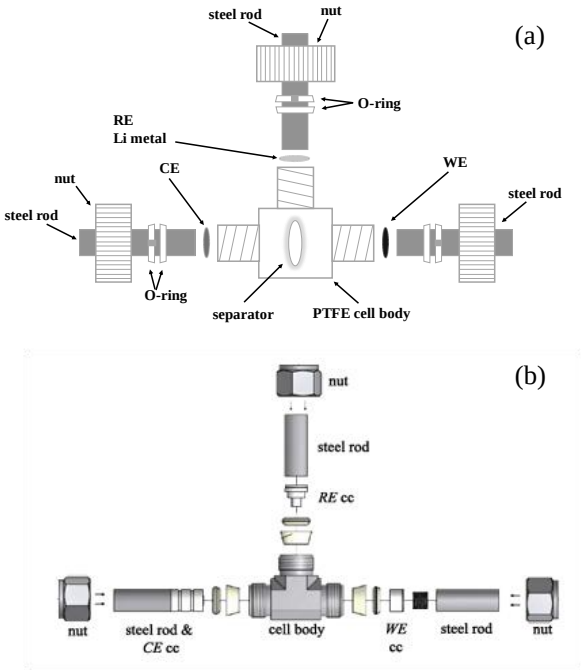


Figure 2.3. Schematic representation of the three-electrode T-shaped (a) BOLA cell (electrode disk 0.636 $cm^2$) and (b) Swagelok cell (electrode disk 1.13 $cm^2$).

For cell assembly different separators were used, i.e. commercial polyolefine or glass fibre separators and a new fluorinated membrane. Dried and degassed commercial monolayer polypropylene (Celgard®2400, 25 µm) and glass fibre (Whatman GF/D, 400 µm thick) separators were used after soaking in the electrolyte solution. PVdF (Solef®6020, Solvay)-based macroporous membrane (18, 23-28 µm), reinforced with nano crystalline cellulose (NCC, FP Innovation), was

also used as separator. This membrane was prepared via a phase-inversion process and provided by Institut Polytechnique de Grenoble (INP) - Laboratoire d'Electrochimie et de Physico-chimie des Matériaux et des Interfaces (LEPMI) (Grenoble, FR, Partner of AMELIE Project).[109] The amount of NCC in the new reinforced PVdF separator was 8-15 wt.%. The dried membrane was soaked in LP30 or LF30 electrolytes, with or without electrolyte additives ($F_1$EC and SA).

Cell assembly was carried out in MBraun Labmaster SP glove box (water and oxygen content < 0.1 ppm) and the electrochemical tests were performed by Perkin-Elmer VMP and Biologic VSP multichannel potentiostats/galvanostats or by the Maccor Battery Tester 4000 in temperature-controlled environments. The electrochemical characterization tests were performed following different protocols. Graphite//LNMO cells were characterized by discharge (Figure 2.4a) and charge capability (Figure 2.4b) tests. The former involved charges at C/10 up to 4.95 V, open circuit voltage (OCV) condition of 0.5 h and discharges at different C-rates, i.e. at C/10 (from two to five cycles) and at C/5, C/3, C/2, 1C and 2 C (four cycles at each C-rate) down to 3.50 V; similarly, the charge capability test involved charges at different C-rates from C/10 to 2C, OCV 0.5 h and discharges at C/10. At the end, additional two or four charge/discharge cycles at C/10 (including 0.5 h OCV) were performed to estimate the capacity retention, i.e. the ratio between the discharge capacity of the last C/10 cycle and that of the 1st one.

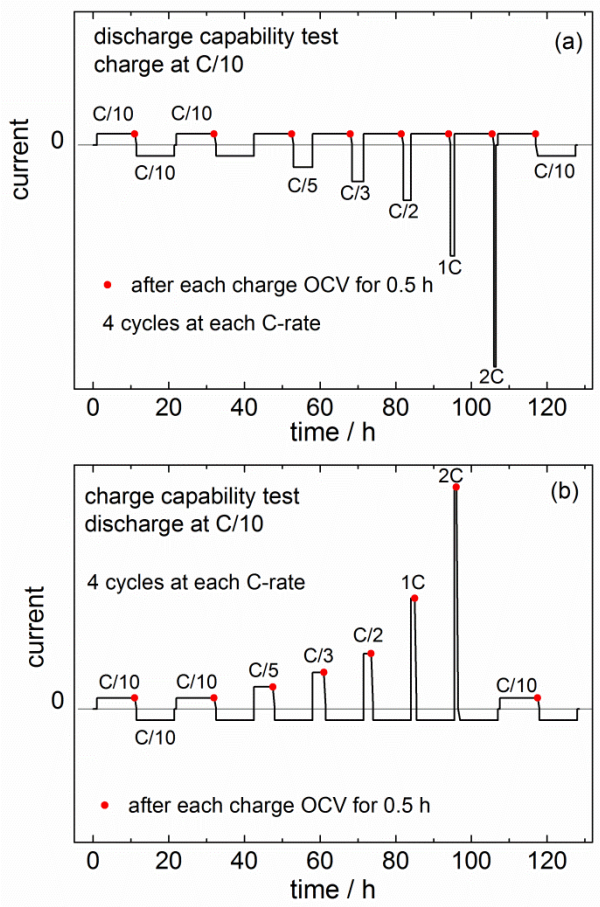


Figure 2.4. Protocols of (a) discharge capability and (b) charge capability tests.

The cells were also tested by 100 galvanostatic charge/discharge cycles between 3.50 V and 4.95 V at 1C effective rate to evaluate their cycling stability. Self-discharge tests were performed as follows: the cell was fully charged at C/10 up to 4.95 V, left in OCV for different times (0.5, 20, 40, 72, 165 h) and discharged down to 3.50 V at C/10. Self-discharge test was performed after five initial cycles (C/10 charge - 0.5 h OCV - C/10 discharge). The recovered charge was evaluated by the following Equation 2.1:

$$Q_{recovery}\% = \frac{Q_{discharge}}{Q_{charge}} \times 100 \quad (2.1)$$

LN05MO-PVdF electrodes were tested in half cell *vs.* $Li^+/Li$ by discharge capability tests with galvanostatic charge up to 4.80 or 4.85 V and discharge at different C-rates (C/2, 1C and 2C, 3C, 5C and 10C) down to 3.50 V. Deep charge/discharge cycles were also performed at 1C within 3.50 and 4.80 or 4.85 V voltage range. In some cases, galvanostatic (CC)-potentiostatic (CV) charge and CC discharge cycles were performed. The electrodes were charged in CC mode at 1C up to 4.80 V, followed by CV charge at 4.80 V with current cut-off of C/7 or C/5, and discharged at 1C down to 3.50 V.

LN05MO-CMC electrodes were characterized in half cell *vs.* $Li^+/Li$ by rate capability test followed by cycling stability test. The former, performed after four galvanostatic charge/discharge cycles at C/3, comprised galvanostatic cycles with charge and discharge at different C-rates (C/3, C/2, 1C, 2C, 3C, 5C and 10C, three cycles at each C-rate); the latter consisted of 20 deep charge/discharge cycles at C/3 followed by 400 cycles (except where a different number of cycles is indicated) at 1C where 5 cycles at C/3 were performed each 100 cycles at 1C.

The C-rates were calculated on the basis of the 146.7 mAh $g^{-1}$ theoretical specific capacity of the LNMO and LN05MO active materials.*

*The method to characterize the discharge (or charge) rates is to standardize the currents to the nominal electrode capacity by the C-rate which indicates the discharge time, expressed in *h*, to deliver the theoretical capacity, expressed in *mAh*, and then the discharge current, in *mA*.

For instance, for an electrode of LNMO (146.7 mAh $g^{-1}$ theoretical specific capacity) featuring 1 g of active mass, the C-rates of C/10, 1C and 2 C indicate discharge times of 10 h, 1 h and 0.5 h and, then, discharge currents of 14.67 mA, 146.7 mA and 293.4 mA, respectively.

The electrode coulombic efficiencies for a defined cycle were determined as the ratio of discharge to charge capacities when performed at the same C-rate; when the C-rates of charge and discharge were different, it was referred to as recovered charge.

Impedance spectroscopy (IS) measurements were performed on graphite//LNMO cells in discharged state in OCV conditions, on Li/LN05MO-PVdF cells in charged state in OCV and on Li/LN05MO-CMC cells in charged state under dc potential using a Biologic VSP potentiostat/galvanostat or Solartron SI 1255 frequency response analyzer coupled with a 273 A PAR potentiostat/galvanostat. An ac amplitude of 5 mV was used, and data were collected taking 10 points per decade in the range 10 kHz - 0.1 Hz or 100 kHz - 10 mHz.

The resistivity of LN05MO-PVdF composite films deposited on Mylar foil (2.54 $cm^2$ area and ca. 50 μm thick) was evaluated using a Jandel multi-height, four-point probe apparatus on dried and pressed composite film.

### 2.4.2 HPPC tests for graphite//$LiNi_{0.4}Mn_{1.6}O_4$ and graphite//$LiNi_{0.5}Mn_{1.5}O_4$ cells

U.S. Department of Energy (DOE) protocols were performed on lab-scale cells even with pre-industrial, high-mass loading electrodes on graphite//LNMO-PVdF and graphite//LN05MO-CMC cells to simulate the performance of these cells in power-assist [110] and plug-in HEV applications.[111] DOE protocols can be directly applicable to a complete battery pack and can also be applied to test lab cells and modules with appropriate scaling by using the battery size factor (BSF) which is the minimum number of units (cells or modules) required for a battery pack to meet all targets.

The characterization tests for hybrid electric vehicle applications included the static capacity (SC) test at constant discharge current to evaluate capacity and energy of the battery system at different depth-of-discharge (DOD), and hybrid

pulse power characterization (HPPC) tests with 10 s discharge and regenerative pulses to determine the dynamic power capability of the battery system. The discharge of SC test was set at 1C effective rate for power-assist HEVs and at constant discharge power of 10 kW referred to the full-size battery pack for plug-in HEVs. In power-assist HEVs the battery is used during acceleration for a brief time and is kept in an almost constant state-of-charge within a DOD range, never approaching the fully charged or fully discharged state, by the regenerative braking or the engine, whereas in PHEVs the battery can be fully discharged and recharged by plugging it into the grid. Therefore, the energy demanded by PHEVs is significantly higher than for power-assist HEVs. Table 2.2 shows the FreedomCAR performance goals for minimum and maximum types of power-assist HEVs and Table 2.3 the DOE goals for the three PHEV types. Minimum and maximum are related to the different types of HEV or PHEV, especially in terms of required power and energy.

Table 2.2. Performance goals for power-assist hybrid electric vehicles

| **Characteristics** | **Units** | **Power-Assist (Minimum)** | **Power-Assist (Maximum)** |
|---|---|---|---|
| Pulse discharge power (10 s) | kW | 25 | 40 |
| Peak regenerative pulse power (10 s) | kW | 20 (55 Wh pulse) | 35 (97 Wh pulse) |
| Total available energy (over DOD range where power goals are met) | kWh | 0.3 (at 1C rate) | 0.5 (at 1C rate) |
| Cycle life, for specified SOC increments | cycles | 300,00 25 Wh cycles (7.5 MWh) | 300,00 50 Wh cycles (15 MWh) |
| Calendar life | years | 15 | 15 |
| Maximum weight | Kg | 40 | 60 |
| Maximum volume | L | 32 | 45 |
| Operating voltage limits | Vdc | max ≤400 min≥ (0.55 Vmax) | max ≤400 min≥ (0.55 Vmax) |

Table 2.3. Performance goals for plug-in hybrid electric vehicles

| **Characteristics at EOL (End-of-Life)** | **Units** | **Minimum PHEV Battery** | **Medium PHEV Battery** | **Maximum PHEV Battery** |
|---|---|---|---|---|
| Reference equivalent electric range | miles | 10 | 20 | 40 |
| Peak discharge pulse power (2 s/10 s) | kW | 50/45 | 45/37 | 46/38 |
| Peak regen pulse power (10 s) | kW | 30 | 25 | 25 |
| Available energy for CD (Charge-Depleting) Mode, 10 kW rate | kWh | 3.4 | 5.8 | 11.6 |
| Available energy for CS (Charge-Sustaining) Mode, 10 kW rate | kWh | 0.5 | 0.3 | 0.3 |
| CD Life/discharge throughput | cycles/MWh | 5,000/17 | 5,000/29 | 5,000/58 |
| CS HEV cycle life, 50 Wh profile | cycles | 300,000 | 300,000 | 300,000 |
| Calendar life, 30 °C | years | 15 | 15 | 15 |
| Maximum system weight | kg | 60 | 70 | 120 |
| Maximum system volume | L | 40 | 46 | 80 |
| Operating voltage limits | Vdc | max 400<br>min> 0.55 Vmax | max 400<br>min> 0.55 Vmax | max 400<br>min> 0.55 Vmax |

### 2.4.3 Electrochemical characterization of separator

The electrochemical tests to evaluate the shutdown behaviour, the resistances and the electrochemical stability towards oxidation and reduction of electrolyte-soaked Celgard®2400 and PVdF-NCC separators were performed in T-shaped BOLA cells with stainless steel blocking electrodes in temperature controlled environments in Memmert IPP 200 oven. The separators were previously soaked for 24 h into electrolyte solution. The shutdown behaviour and the resistances of both soaked separators to calculate the respective MacMullin numbers at 30 °C were evaluated by IS measurements using a Solartron SI 1255 frequency response analyzer coupled with a 273 A PAR potentiostat/galvanostat with a perturbation amplitude of 5 mV and 10 points/decade in the range 10 kHz - 0.1 Hz. In particular, the shutdown behaviour was evaluated by IS measurements at different temperatures. The temperature increased starting from 30 °C up to 220 °C at 1 °C $min^{-1}$. The IS spectra were collected each 20 °C up to 90 °C, subsequently each 10 °C up to 220 °C to better determine the temperature at which the shutdown took place and the cells were kept for 10 min at the selected temperature before starting the measurement. The resistance of the soaked separators was evaluated by the real part of impedance, Zre, at 1 kHz.

The electrochemical stability towards oxidation and reduction of the PVdF-NCC membrane and Celgard®2400 separator as investigated by linear sweep voltammetries at 5 mV $s^{-1}$ in LF30 electrolyte (without additives) at 30 °C in the range from 0.05 to 6.00 V *vs.* $Li^+/Li$ in three-electrode mode configuration using Li as reference electrode.

# Chapter 3. High-voltage graphite//$LiNi_{0.4}Mn_{1.6}O_4$ cells operating with different electrolytes and separators

Chapter 3 deals with the investigation of the effect of electrolytes and separators on capacity retention over cycling and on self-discharge of full cells with $LiNi_{0.4}Mn_{1.6}O_4$ (LNMO) positive and graphite negative electrodes. Electrochemical performance of cells having carbonate-based (EC:DMC) electrolyte with a non-conventional ($Li[(C_2F_5)_3PF_3]$) lithium salt, named LF30, is compared to that of cells in EC:DMC with conventional $LiPF_6$ lithium salt, named LP30, with and without SEI-forming additives, succinic anhydride (SA) to protect the cathode and 1-fluoro ethylene carbonate ($F_1EC$) for the graphite anode. Even the effect of a new fluorinated macroporous PVdF separator reinforced with nano crystalline cellulose (NCC), instead of the commercial microporous Celgard®2400, on cycling performance of the cells is reported and discussed.

Elsevier is acknowledged for the permission to reprint some parts of the following publications:

- C. Arbizzani, F. De Giorgio, L. Porcarelli, M. Mastragostino, V. Khomenko, V. Barsukov, D. Bresser, S. Passerini, Use of non-conventional electrolyte salt and additives in high-voltage graphite/$LiNi_{0.4}Mn_{1.6}O_4$ batteries, J. Power Sources, 238 (2013), 17-20. Copyright (2013).
- C. Arbizzani, F. Colò, F. De Giorgio, M. Guidotti, M. Mastragostino, F. Alloin, M. Bolloli, Y. Molméret, J.-Y. Sanchez, A non-conventional fluorinated separator in high-voltage graphite/$LiNi_{0.4}Mn_{1.6}O_4$ cells, J. Power Sources 246 (2014), 299-304. Copyright (2014).
- C. Arbizzani, F. De Giorgio, M. Mastragostino, Characterization tests for plug-in hybrid electric vehicle application of graphite/$LiNi_{0.4}Mn_{1.6}O_4$ cells with two different separators and electrolytes, J. Power Sources 266 (2014), 170-174. Copyright (2014).

## 3.1 Electrochemical characterization of graphite//$LiNi_{0.4}Mn_{1.6}O_4$ cells with LF30 and additives

The study on the effect of the substitution of $LiPF_6$ with the non-conventional lithium tris(pentafluoroethyl)trifluorophosphate (LiFAP) lithium salt in EC:DMC and of the addition of additives on the electrochemical performance of graphite//LNMO cells was carried out by using LNMO cathodes and graphite anodes provided in the frame of AMELIE Project from different Partners. LNMO composite electrodes based on LNMO active material synthesized by CEA-LITEN (Grenoble, FR) were prepared by MEET (Münster, DE), and the graphite composite electrodes based on commercial graphite were prepared by Kiev National University of Technologies and Design. The cells with electrodes of 0.636 $cm^2$ geometric area were tested in LP30 and LF30 without and with additives, namely 1.6 wt.% $F_1$EC and 2 wt.% SA, with commercial Celgard®2400 separator at 30 °C. Table 3.1 reports the formulation and the active material mass loading of the LNMO and graphite electrodes. All the graphite//LNMO cells were assembled with electrodes having balanced capacity.

Table 3.1. Formulation and active mass loading range of graphite and LNMO electrodes tested in full cells with LF30 and LP30 based electrolytes and Celgard®2400 separator at 30 °C.

| **electrode formulation / wt.%** | | **active mass loading / mg $cm^{-2}$** | |
|---|---|---|---|
| **graphite anode** | **LNMO cathode** | **graphite** | **LNMO** |
| 89% SLA-1025<br>3% PureBLACK™<br>8% PVdF<br>(Solef®5130) | 85% LNMO<br>10% Super C65<br>5% PVdF<br>(Solef®5130) | 2.5 ÷ 5.2 | 7.5 ÷ 14.8 |

The characteristic charge/discharge voltage profiles of LNMO composite electrodes display a shoulder at ca. 4.0 V *vs.* $Li^+/Li$ due to the oxidation of $Mn^{3+}$ to $Mn^{4+}$ and a sharp plateau at higher potentials (4.70 - 4.75 V *vs.* $Li^+/Li$) due to

oxidation of $Ni^{2+}$ to $Ni^{3+}$ and of $Ni^{3+}$ to $Ni^{4+}$, as clearly shown by the voltage profiles of Figure 3.1 during the first galvanostatic cycle between 3.50 V and 4.95 V of an electrode in half cell with LP30 at 30 °C. The Mn redox process contributes to one fifth of the overall capacity while the remaining capacity is due to the Ni redox processes.

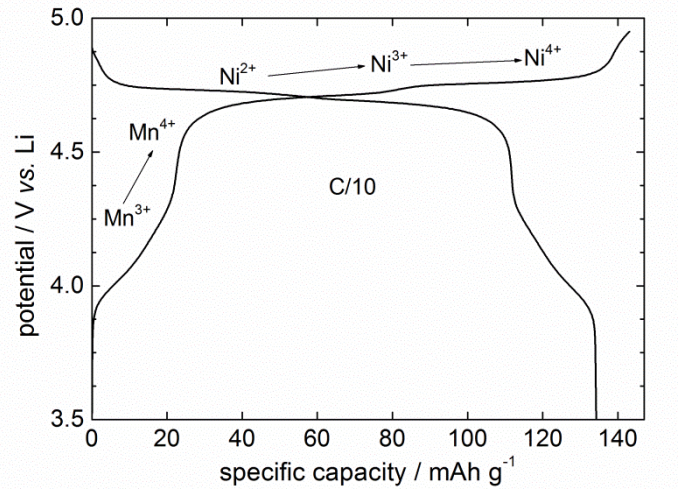


Figure 3.1. Voltage profile of LNMO (half cell *vs.* Li with LP30 and Celgard®2400 separator) over the first galvanostatic charge/discharge cycle at C/10 (135 μA $cm^{-2}$) at 30 °C. Reprinted from ref. [112], Copyright (2013), with permission from Elsevier.

Despite the thermodynamic instability of LP30 above 4.5 V, the lithium extraction/insertion process during the first cycle of LNMO electrode in half cell *vs.* Li is highly reversible, thus showing a coulombic efficiency of 94%. However, moving to full cell, the electrochemical performance of graphite//LNMO cells are very poor, as shown by the results of the charge capability tests of Figure 3.2 performed in LP30 at 30 °C on low-mass loading graphite and LNMO electrodes. The test involved galvanostatic cycles between 3.50 and 4.95 V at different C-rates from C/10 to 2C during charge and the same discharge rate (C/10) after 30 min in OCV (4 cycles at each C-rate). Additional 4 charge-discharge cycles at C/10 were

carried out at the end of such charge capability test for the evaluation of the capacity retention, i.e. the ratio between the discharge capacity of the last C/10 cycle and that of the 1st one.

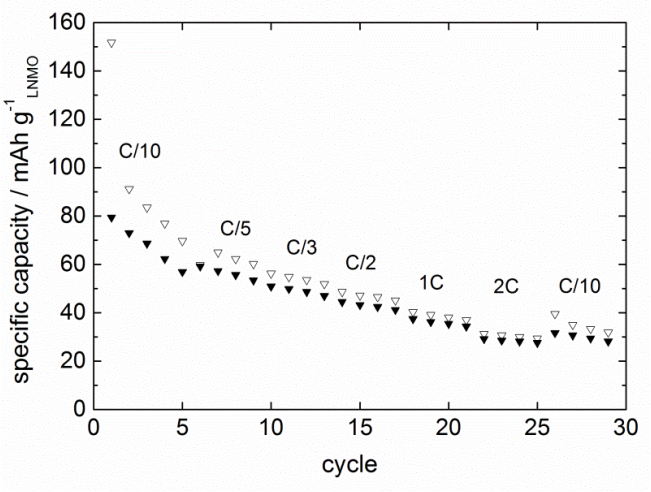


Figure 3.2. Specific capacity (referred to the active mass of the cathode) of charge (void symbol) and discharge (full symbol) under charge capability tests in LP30 at 30 °C.

With the aim to improve the cycling performance of the cells, SA (2 wt.%) was added to LP30 to protect the cathode since it should promote the formation of a protective layer on the LNMO surface against the oxidative electrolyte decomposition,[60] and $F_1$EC (1.6 wt.%) as SEI forming for the anode (instead of vinylene carbonate not suitable in combination with high-voltage cathodes).[59] Figure 3.3 compares the LSVs at Pt electrode in LP30 with and without additives and evinces the beneficial effect of the two additives on the oxidation potentials of LP30. However, the results of the charge capability tests of the graphite//LNMO cells were not sufficiently enhanced by the presence of additives, as shown in Figure 3.4 which compares the results of tests in LP30 with and without additives, even though a slight improvement is observable in the capacity retention, i.e. 49% in LP30 with additives against 35% in LP30 alone.

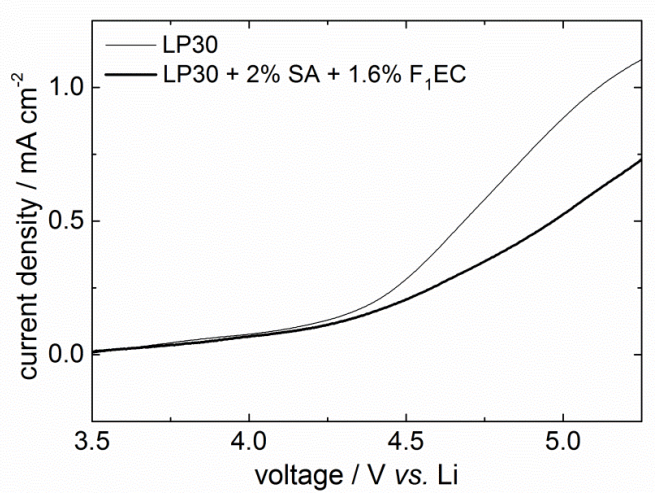


Figure 3.3. LSVs at 20 mV $s^{-1}$ on Pt electrode at 30 °C of LP30 and LP30 – 1.6% $F_1EC$ – 2% SA with Celgard®2400 separator. Reprinted from ref. [112], Copyright (2013), with permission from Elsevier.

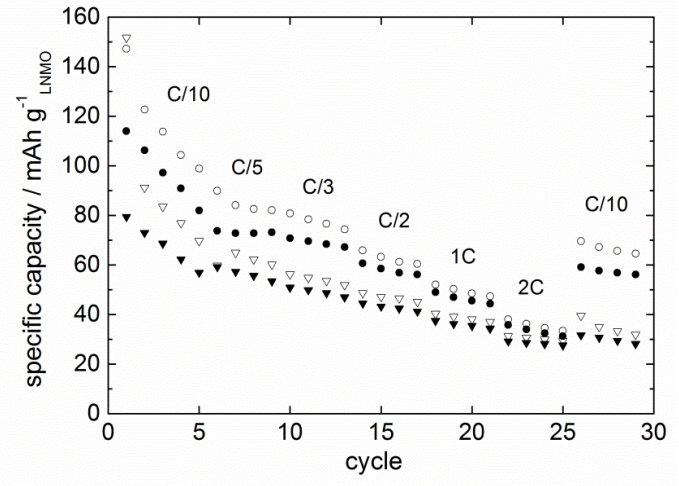


Figure 3.4. Specific capacity (referred to the active mass of the cathode) of charge (void symbol) and discharge (full symbol) under charge capability tests at 30 °C of graphite//LNMO cells having low mass loading electrodes with LP30 (triangles) and LP30 – 1.6% $F_1EC$ – 2% SA (circles) and Celgard®2400 separator. Reprinted from ref. [112], Copyright (2013), with permission from Elsevier.

Owing to the low performance of the graphite//LNMO cells in LP30 even with additives, the shift to a more stable electrolyte at such high operating voltages was mandatory. The commercial LF30 featuring as lithium salt lithium tris(pentafluoroethyl)trifluoroposphate (LiFAP) instead of LP30 was proposed and its effect on cell electrochemical performance was investigated. The replacement of fluorine atoms of $LiPF_6$ with electron withdrawing perfluorinated alkyl groups leads to stabilize P-F bonds and LiFAP is thus more stable than $LiPF_6$ towards hydrolysis. Therefore, it is expected to have a beneficial effect on the performance of the high-voltage graphite//LNMO cells. Moreover, LF30 and LP30 display roughly the same conductivity, and LiFAP has also a positive effect on the flashpoint of the organic carbonates with respect to $LiPF_6$, thus improving the safety of the resulting lithium-ion cells.[50–53]

Full cells with LF30 even in presence of $F_1$EC (1.6 wt.%) and SA (2 wt.%) additives were assembled with Celgard®2400 separator and tested at 30 °C. Figure 3.5 compares the results of the charge capability tests performed on graphite//LNMO cells with low-mass loading electrodes in LF30 and in LF30-$F_1$EC-SA. Irrespective of the presence of additives, the charge capability results of both cells are almost the same and the recovered charge is ca. 80% at the first cycle (C/10) increasing over cycling up to 96% at the fifth cycle at C/10. The slightly positive effect of additives is observed on the capacity retention that was 64% for the cell in LF30 and 69% for that in LF30 with additives.

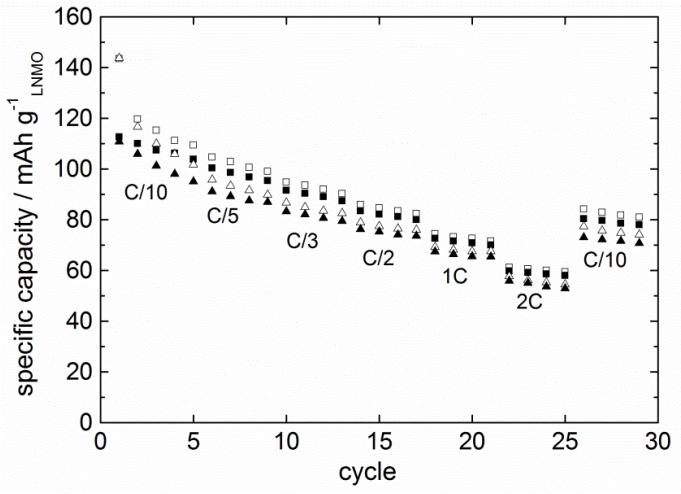


Figure 3.5. Specific capacity (referred to the active mass of the cathode) of charge (void symbol) and discharge (full symbol) under charge capability tests at 30 °C of graphite//LNMO cells having low mass loading electrodes with LF30 (triangles) and LF30 – 1.6% $F_1$EC – 2% SA (squares) and Celgard®2400 separator. Reprinted from ref. [112], Copyright (2013), with permission from Elsevier.

The comparison of the charge capability data of cells tested in LF30 and LP30 electrolytes reported in Figure 3.6 clearly shows the beneficial effect of LF30 with respect to LP30 on cycling performance of the graphite//LNMO cells. The capacity retention of the cells with LF30 is 64% against 35% in LP30 and that of the cells in LF30-$F_1$EC-SA is 69% against 49% in LP30-$F_1$EC-SA. However, the loss of capacity over the first cycles at C/10 still occurs also in LF30 with and without additives, although it is more limited than that in LP30.

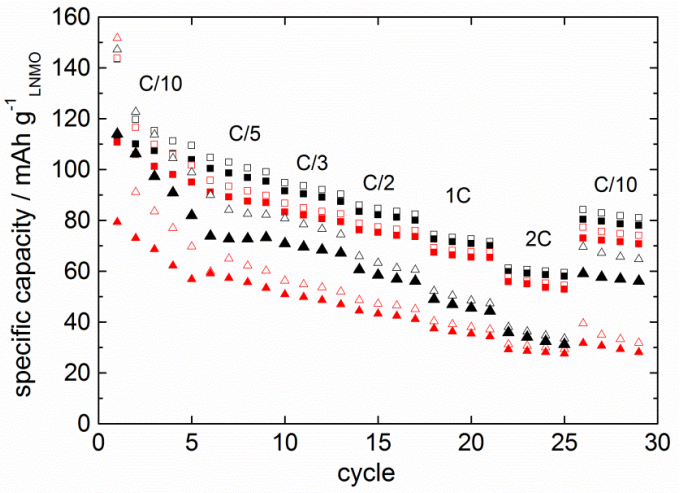


Figure 3.6. Specific capacity (referred to the active mass of the cathode) of charge (void symbol) and discharge (full symbol) under charge capability tests at 30 °C of graphite//LNMO cells having low-mass loading electrodes with LF30 (squares) and LP30 (triangles) without (red) and with 1.6% $F_1$EC and 2% SA (black) and Celgard®2400 separator.

Such a capacity loss is mitigated in full cells with high-mass loading electrodes as shown in Figure 3.7 which compares the results of charge capability tests of cells with high- and low-mass loading electrodes. Indeed, high-loadings involve high current densities that should limit the side-reactions at the electrode/electrolyte interface, particularly during the first cycles where the effect of additives on the recovered charge is more evident. By contrast, at high-rates (1C and 2C) the current densities of the high-mass loading electrodes are much higher than for low-mass loadings, thus resulting in higher ohmic drops and, hence, higher capacity loss. However, the capacity retention at the end of the tests of the cells with high-mass loading electrodes increased up to 70% in LF30 and 87% in LF30 with additives.

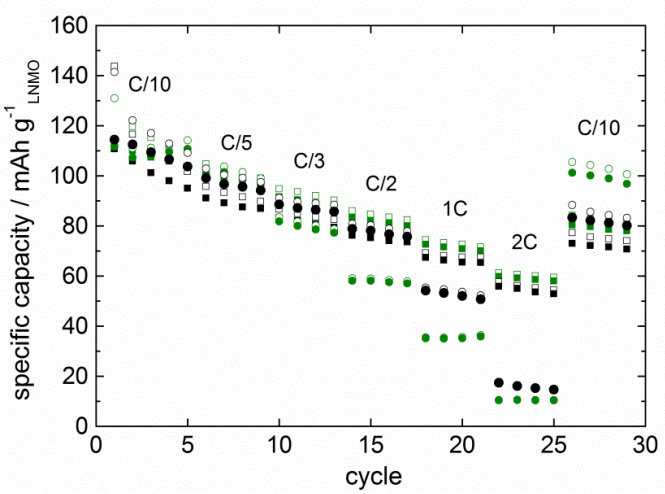


Figure 3.7. Specific capacity (referred to the active mass of the cathode) of charge (void symbol) and discharge (full symbol) under charge capability tests at 30 °C of graphite//LNMO cells having low- (squares) and high- (circles) mass loading electrodes in LF30 (black) and LF30-1.6% $F_1$EC-2% SA (green) and Celgard®2400 separator.

In order to investigate the self-discharge behaviour of graphite//LNMO cells, the self-discharge tests were performed in LP30 and LF30 both with and without additives at 30 °C. The self-discharge tests were carried out according to the following protocol: five initial cycles with charge at C/10, followed by OCV of 0.5 h and discharge at C/10, charge/discharge cycles with charge at C/10 up to 4.95 V (100% state-of-charge), storage in OCV for different times (0.5, 20 and 40 h) and subsequently discharge at C/10 down to 3.50 V. The self-discharge process is basically caused by the ongoing electrolyte decomposition at the cathode surface, which leads to capacity loss and voltage decay.[113–116]

According to Yang *et al.*,[116] who investigated the self-discharge of high-voltage $LiNi_{0.5}Mn_{1.5}O_4$ in EC/DEC/DMC with $LiPF_6$ stored in OCV for one week at potentials higher than 4.7 V *vs.* $Li^+$/Li, the main component of passivation film formed on the cathode surface is the poly(ethylene)carbonate due to the oxidative polymerization of EC with the reduction of the cathode material and the re-insertion

of $Li^+$ to maintain the charge neutrality. However, the oxidative electrolyte decomposition could be inhibited by the formation of an effective protective layer at the cathode/electrolyte interface, as expected when SEI-forming additives are used.[60]

The results of self-discharge test performed on graphite//LNMO cells, shown in Table 3.2, demonstrate that the lowest self-discharges were observed in LF30 with and without (the presence of the additives slightly improve the self-discharge behaviour of the cells). The Table reports the percentage of recovered charge after storage in OCV for different time for the cells tested in different electrolytes. The data clearly show that in LP30 the oxidative electrolyte decomposition is much stronger than in LF30. Moreover, the addition of the additives in LP30 is not sufficient to form an effective protective layer on LNMO surface, as evinced by the self-discharge results of the cell with LP30 and additives even lower than that of cell with LP30 alone.

Table 3.2. Recovered charge upon discharge at C/10 of graphite//LNMO cells charged at C/10 and stored in OCV for different times at 30 °C in different electrolytes with Celgard®2400 separator.

| **self-discharge test on graphite//LNMO in different electrolytes** | **recovered charge after discharge at C/10 and storage in OCV for different times %** | | | | |
|---|---|---|---|---|---|
| | **0.5 h** | **20 h** | **40 h** | **72 h** | **165 h** |
| LP30 | 89 | 74 | 57 | - | - |
| LP30-1.6 wt.% $F_1$EC - 2 wt.% SA | 86 | 68 | 46 | - | - |
| LF30 | 89 | 81 | 73 | - | - |
| LF30-1.6 wt.% $F_1$EC - 2 wt.% SA | 90 | 83 | 75 | 72 | 53 |

The self-discharge in LF30-$F_1$EC-SA was investigated over longer times, i.e. 72 and 165 h, and Figure 3.8 displays the discharge voltage profiles at C/10 *vs.* the recovered charge of fully charged cells at C/10 and stored in OCV for different times at 30 °C. The cell recovered 72% and 53%, after 72 and 165 h, respectively.

These findings suggest that LF30 with additives may be a suitable electrolyte to form stable protective layer on the LNMO surface thus preventing further electrolyte decomposition promoted during the self-discharge upon storage at high potentials.

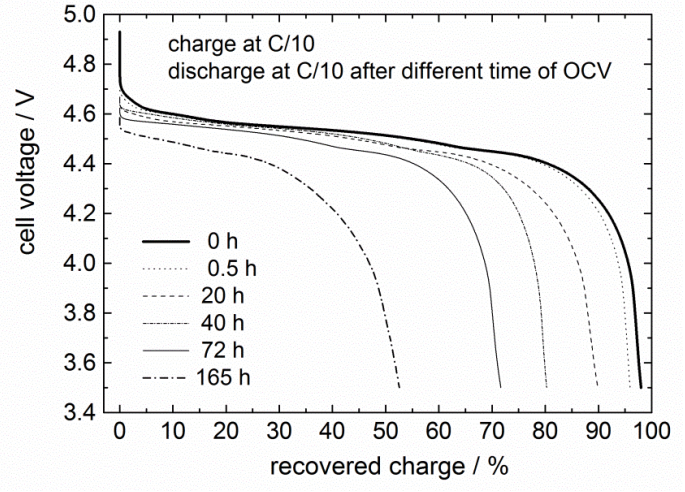


Figure 3.8. Recovered charge upon discharge at C/10 of graphite//LNMO cell charged at C/10 and stored in OCV for different times at 30 °C in LF30–1.6% $F_1$EC–2% SA and Celgard®2400 separator.

In order to better investigate the effect of $F_1$EC and SA on the LNMO/electrolyte interface, and to evaluate thickness and composition of the layer formed on LNMO surface due to electrode-electrolyte reactions, XPS measurements on low-mass loading cathodes before (pristine LNMO) and after (cycled LNMO) cycling in different electrolyte systems were performed. The cycling tests were carried out in half cell *vs.* Li and involved 3 charge/discharge cycles at C/10 followed by 27 cycles at C/5 between 3.50 and 4.95 V *vs.* $Li^+$/Li.

Figures 3.9a-h show the spectra of Mn 2p (Fig. 3.9a-d) and O 1s (Fig. 3.9e-h).

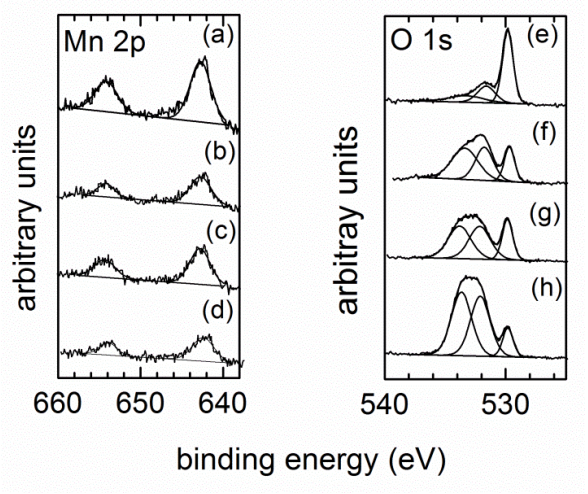


Figure 3.9. Mn 2p and O 1s XPS peaks of LNMO electrodes (a, e) pristine, and after 30 cycles at 30 °C using (b, f) LF30, (c, g) LF30 – 1.6 % $F_1$EC– 2% SA, (d, h) LP30 – 1.6 % $F_1$EC – 2% SA. Reprinted from ref. [112], Copyright (2013), with permission from Elsevier.

Mn2p signal (Figure 3.9a-d) is split in two peaks due to spin-orbit coupling: the peak at ~ 654 eV corresponds to the Mn $2p_{1/2}$ and that at ~ 642 eV (intensity ratio of 1:2) corresponds to the Mn $2p_{3/2}$ both for the pristine LNMO (3.9a) and for those cycled at 30 °C in LF30 (3.9b), LF30-1.6% $F_1$EC-2% SA (3.9c) and LP30-1.6% $F_1$EC-2% SA (3.9d). After cycling, the intensity of the signals is lower due to the decomposition products of the electrolyte oxidation deposited on the electrode surface. The atomic percentage of Mn was 1.60 for the pristine LNMO and 0.59, 0.76, 0.56 for LNMO cycled in LF30, LF30-1.6% $F_1$EC-2% SA and LP30-1.6% $F_1$EC-2%SA, respectively. Given that the intensity of the signal strongly depend on the thickness of the passivation layer on LNMO surface, the higher is the intensity of the signal of Mn 2p peaks the thinner is the layer; therefore, the thinnest layer was formed when LF30-1.6% $F_1$EC-2% SA was used.

The O 1s spectra of the pristine LNMO electrode (Figure 3.9e) displays a narrow peak at ~ 529 eV attributable to the $O^{2-}$ anions of LNMO,[117] as well as two peaks

at higher binding energies at ~ 530 and ~ 533 eV, that can be assigned to absorbed species at the LNMO surfaces. The intensity of the peak at ~ 529 eV lowers after 30 cycles in all the cycled LNMO cathodes (3.9f-h), as also observed for Mn2p spectra (3.9b-d). The peaks at ~ 530 and ~ 533 eV are shifted to higher values of binding energies in the cycled electrodes (3.9g-h), owing to the formation of oxygenated species like $R_2CO_3$ and $Li_2CO_3$ on the electrode surface upon cycling.[60] These peaks are much stronger when LP30 with additives was used, thus suggesting that the amount of these species are higher than for the other samples.

The XPS results confirm that the best electrochemical performance of the graphite//LNMO cells with LF30-based electrolyte is due to a decreased electrolyte decomposition in LF30 thanks to a more stable passivation layer on LNMO surface, being in good agreement with the improved capacity retention over cycling and with the lowest self-discharge upon storage at high potentials of cells in LF30 with and without additives.

## 3.2 Non-conventional PVdF-based separator in high-voltage graphite//$LiNi_{0.4}Mn_{1.6}O_4$ cells

The investigation of the effect of the separator on electrochemical performance of graphite//LNMO cells were carried out by using LNMO cathodes, graphite anodes and separators provided in the frame of AMELIE Project as previously described in Section 3.1. The study was also carried out on LNMO and graphite pre-industrial electrodes of optimized composition and mass loading prepared by means the battery line at CEA-LITEN laboratories. The cells with electrodes of 0.636 $cm^2$ geometric area were tested with PVdF-NCC macroporous membrane provided by INP-LEPMI and PP commercial microporous Celgard®2400 used as separators and soaked in EC:DMC 1:1 - 1 M LiFAP (LF30) electrolyte with 1.6% $F_1$EC and 2% SA as additives. Table 3.3 reports the formulation and the active material mass loading of the LNMO and graphite electrodes tested in full cell.

Table 3.3. Formulation and active material mass loadings of the graphite and LNMO electrodes tested in full cells with LF30-1.6% $F_1$EC-2% SA and different separators at 30 °C.

| **electrode formulation / wt.%** | | **active mass loading / mg $cm^{-2}$** | |
|---|---|---|---|
| **graphite anode** | **LNMO cathode** | **graphite** | **LNMO** |
| 89% SLA-1025<br>3% PureBLACK™<br>8% PVdF<br>(Solef®5130) | 85% LNMO<br>10% Super C65<br>5% PVdF<br>(Solef®5130) | 3.0 | 7.7 |
| *pre-industrial electrodes* | | | |
| 91% SLA-1025<br>3% PureBLACK™<br>6% PVdF<br>(Solef®5130) | 92% LNMO<br>4% Super C65<br>4% PVdF<br>(Solef®5130) | 8.7 | 21.4 |

### 3.2.1 Characterization of PVdF-NCC and Celgard®2400 separators

The PVdF macroporous membrane reinforced with nano crystalline cellulose (NCC) to enhance the mechanical properties of PVdF was prepared by INP-LEPMI by means of a phase inversion process as described in ref. [109].

The evaluation of the NCC content was carried out by thermogravimetric (TGA) measurements. Figure 3.10 shows the TGA in Ar atmosphere of dry PVdF-NCC membrane from 30 °C to 700 °C and clearly evinces a first weight loss in the temperature range 260-300 °C that corresponds to 8 wt.% due to the thermal decomposition of NCC; then, the weight remains constant up to 430 °C where the PVdF decomposition starts. The Figure also shows the TGA of dry Celgard®2400 separator for comparison of the thermal stabilities of both separators.

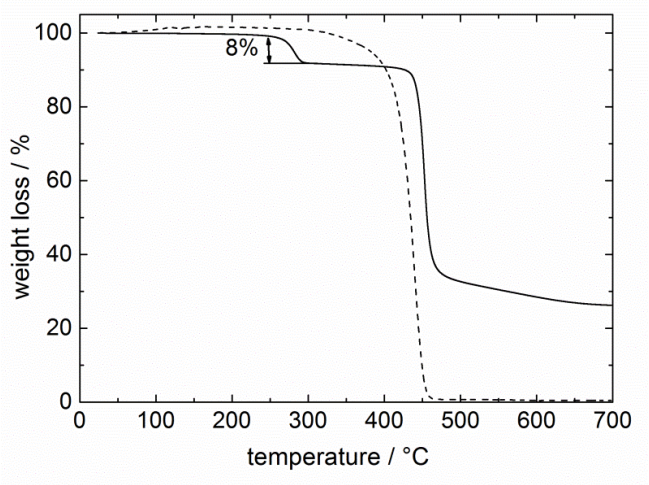


Figure 3.10. Thermogravimetric analysis of dry PVdF-NCC (solid line) and Celgard®2400 (dashed line) separators in Ar flux (5 °C $min^{-1}$). Reprinted from ref. [109], Copyright (2014), with permission from Elsevier.

To evaluated the resistance of electrolyte (LF30-1.6% $F_1$EC-2% SA)-soaked membranes, PVdF-NCC and Celgard®2400, impedance spectroscopy measurements with stainless steel blocking electrodes were performed at 30 °C and the

corresponding Nyquist plots are in Figure 3.11. The resistance values at 1 kHz are 5.6 and 11.6 ohm $cm^2$ for PVdF-NCC and Celgard, respectively, thus suggesting that the reinforced PVdF-NCC membrane will contribute to the cell resistance less than the Celgard. This is also confirmed by the MacMullin number, $N_M$, i.e. the ratio of resistivity of the electrolyte-soaked separator to that of the electrolyte according to Eq. 1.3, thus strictly depending on membrane's porosity and tortuosity.[74]

$N_M$ was evaluated for both membranes, by taking into account their thickness (18 μm for PVdF-NCC and 25 μm for Celgard), from the intercepts on the *x*-axis of the plots of Figure 3.11 and the electrolyte resistivity of $1.2 \cdot 10^2$ ohm cm obtained by the conductivity measurement of LF30-1.6% $F_1$EC-2% SA ($8.51 \cdot 10^{-3}$ S $cm^{-1}$ at 30 °C). The $N_M$ of PVdF-NCC membrane resulted 6, much lower value than that of Celgard separator, namely 16.

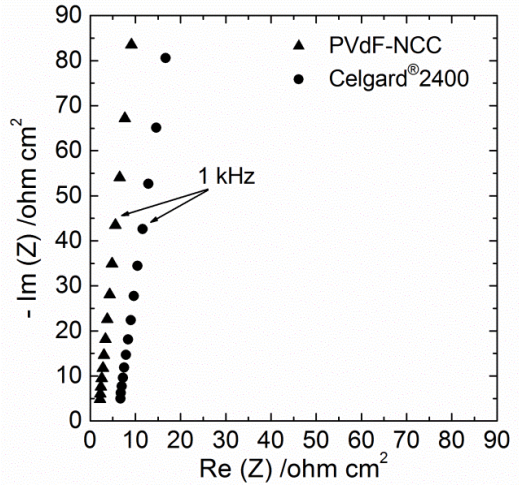


Figure 3.11. IS spectra at 30 °C (10 kHz - 0.5 kHz) of PVdF-NCC and Celgard®2400 separators soaked in LF30-1.6%$F_1$EC-2%SA. Reprinted from ref. [109], Copyright (2014), with permission from Elsevier.

This result is also supported by the higher porosity of PVdF-NCC (60%) than that of Celgard®2400 (41%), as clearly shown by SEM images of Figure 3.12. Given that the MacMullin number should be as low as possible to assure high rate capability, safety and long cycle life of the battery,[73] the PVdF-NCC separator should affect battery performance at high C-rates less than Celgard.

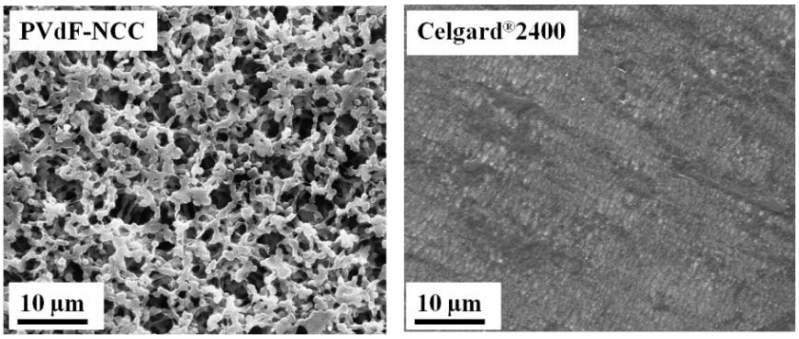


Figure 3.12. SEM images of dry PVdF-NCC and Celgard®2400 separators at 5.00 KX magnification. Reprinted from ref. [109], Copyright (2014), with permission from Elsevier.

As previously explained in Chapter 1, separator is also a crucial component for battery safety.[78] In abuse conditions as the cell temperature increases the separator should close the pores to stop ionic transport and then the current flow, still maintaining a good mechanical integrity to avoid internal short circuits. The temperature at which the membrane closes the pores and becomes an insulator is named shutdown temperature, and this temperature generally corresponds to the melting temperature of the polymer.

Figure 3.13a, which displays the logarithm of the real part of the impedance, $Z_{re}$, of the electrolyte (LF30-1.6%$F_1$EC-2%SA)-soaked PVdF-NCC membrane at 1 kHz *vs*. temperature, shows a great resistance increase at 180 °C and this is, thus, the shutdown temperature of this separator. It is worth noting that after the polymer melting, the PVdF-NCC still displays a good melt integrity as evinced by the resistance values that remain high up to 220 °C, a temperature well above the

required minimum melt integrity temperature of 150 °C. Figure 3.13b shows the results for Celgard®2400 separator, which are comparable to those of the PVdF-NCC, and the shutdown temperature for the Celgard is ca. 160 °C. The melting temperatures from differential thermal analysis (DTA) of the two separators are in the insets of Figures 3.13 and while the shutdown and the melting temperatures of Celgard correspond, the shutdown temperature of the PVdF-NCC is ca. 20 degrees higher than its melting temperature, presumably due to the macroporous nature of this reinforced membrane.

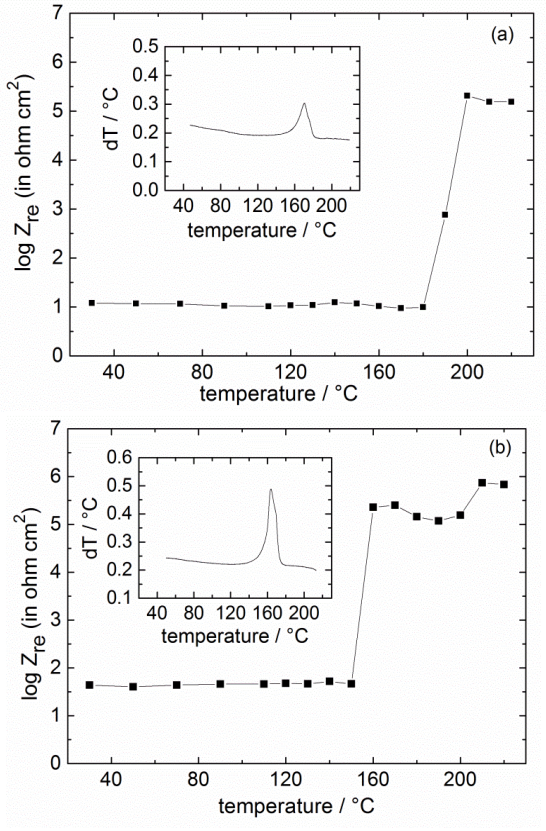


Figure 3.13. Logarithm $Z_{re}$, at 1 kHz *vs.* temperature over shutdown tests of electrolyte (LF30-1.6%$F_1$EC-2%SA)-soaked (a) PVdF-NCC and (b) Celgard®2400 separators. Insets display the DTA traces (5 °C min$^{-1}$) of dry separators. Reprinted from ref. [109], Copyright (2014), with permission from Elsevier.

The electrochemical stability of separators towards oxidation and reduction is an important requirement to assure good cycling performance, especially when high-voltage cathodes are involved. The electrochemical stability of PVdF-NCC and Celgard®2400 separators was evaluated by linear sweep voltammetry (LSV) measurements carried out in three-electrode cell with LF30 electrolyte without additives. Figure 3.14 shows the second LSV of PVdF-NCC at 5 mV $s^{-1}$ towards more positive and negative potentials as well as that of Celgard for a comparison. In both cells the anodic and the cathodic limits are restricted by the electrolyte, thus indicating that PVdF-NCC and Celgard®2400 separators are stable at oxidation potentials higher than 5.0 V *vs.* $Li^+$/Li and that both separators may be used in high-voltage lithium-ion batteries.

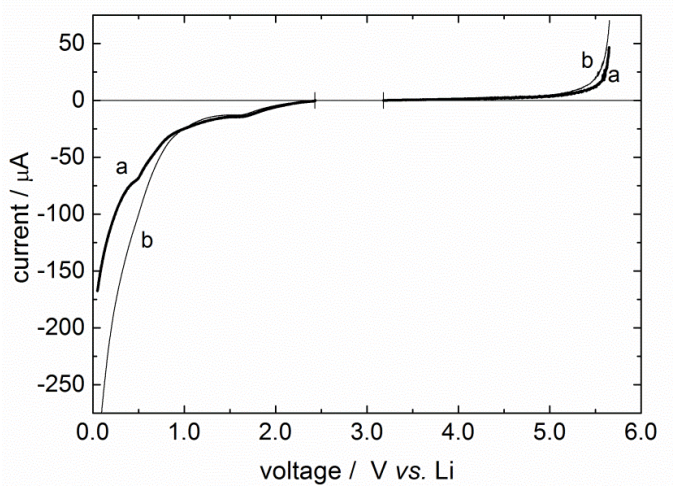


Figure 3.14. 2nd LSVs towards oxidation and reduction potentials at 5 mV $s^{-1}$ of (a) PVdF-NCC and (b) Celgard®2400 separators in LF30 at 30 °C. The LSVs were performed in three-electrode mode configuration with a T-shaped BOLA cell featuring stainless steel electrodes as working and counter electrodes and Li metal as reference. Reprinted from ref. [109], Copyright (2014), with permission from Elsevier.

### 3.2.2 Electrochemical characterization of graphite//LNMO cells with PVdF-NCC and Celgard®2400 separators

Owing to the appealing properties of the macroporous PVdF-NCC membrane, it was investigated in high-voltage graphite//LNMO cells as separator soaked in LF30- 1.6% $F_1$EC- 2% SA. The cells were tested between 3.50 and 4.95 V at 30 °C according to the protocols of discharge and charge capability and self-discharge. Repeated galvanostatic charge/discharge cycles at 1C effective rate were also performed to evaluate the cycling stability of the cells. IS measurements on the cell in discharged state at the beginning and at the end of the charge capability tests were performed. To better highlight the improvement in terms of cycling performance of the graphite//LNMO cells with PVdF-NCC separator, all the results are compared to those with Celgard®2400. The discharge and charge capability data of the cells with PVdF-NCC and Celgard®2400 separators are compared in Figure 3.15.

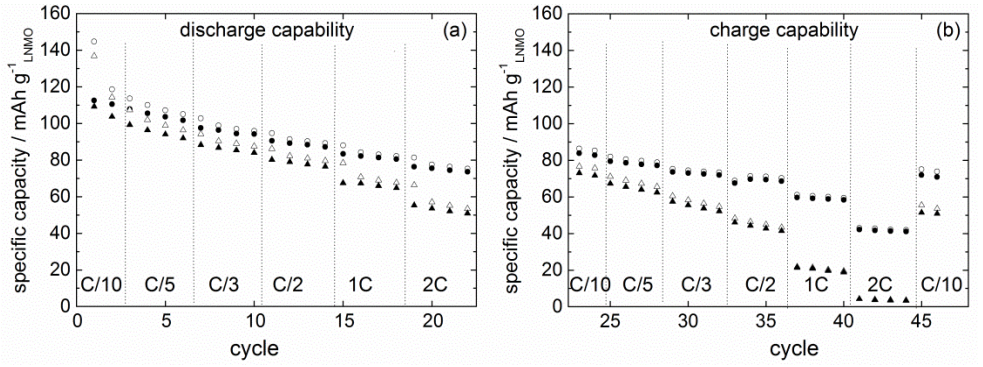


Figure 3.15. Comparison of discharge (a) and charge (b) capability data of graphite//LNMO cells with PVdF-NCC (circle) and Celgard®2400 separators (triangles) in LF30-1.6% $F_1$EC-2% SA at 30 °C. Charges are indicated by void and discharges by full symbols. Reprinted from ref. [109], Copyright (2014), with permission from Elsevier.

PVdF-NCC cell displays higher capacities than Celgard cell, especially at the highest C-rate (2C), particularly evident in the charge capability test of Figure 3.15b. The capacity retention of the cell with PVdF-NCC separator is thus higher than that of cell with Celgard, i.e. 62% against of 46%.

Presumably, the better compatibility between the PVdF-NCC membrane and the graphite and LNMO electrodes, which in turn feature PVdF binder, is responsible of the lower and more stable ion transport resistance of the PVdF-NCC separator with respect to the Celgard, thus positively affecting the graphite//LNMO performance especially at high C-rates. This assumption is also supported by the impedance data of Figure 3.16 recorded at the beginning (i.e. 24$^{th}$ cycle) and the end (46$^{th}$ cycle) of the charge capability tests on the discharged cells with PVdF-NCC and Celgard separators. The data clearly display that while the $Z_{re}$ value at 1 kHz of the cell with PVdF-NCC membrane remains constant over cycling at 17 ohm cm$^2$, that of the cell with Celgard increases from 41 to 57 ohm cm$^2$, thus justifying the higher capacity loss of Celgard cell over cycling.

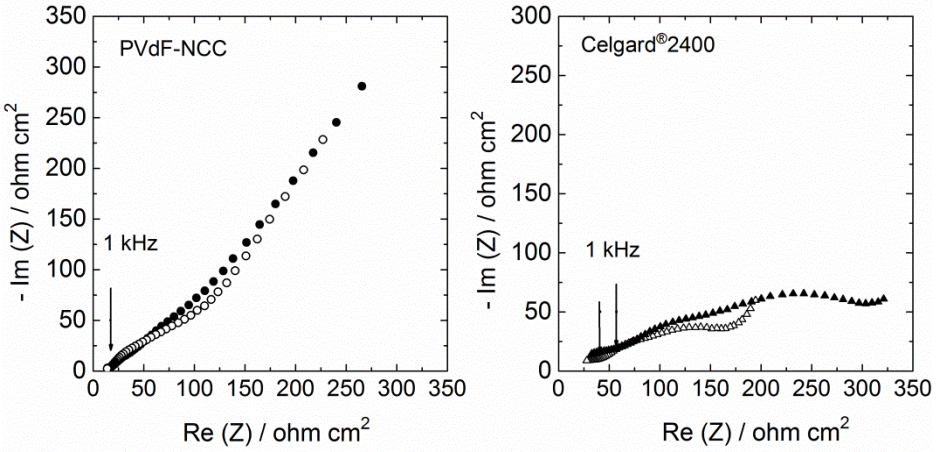


Figure 3.16. IS spectra (10 kHz - 0.1 Hz) recorded at the beginning (24$^{th}$ cycle) and the end (46$^{th}$ cycle) of the charge capability tests on the discharged graphite//LNMO cells with PVdF-NCC and Celgard®2400 separators in LF30-1.6%$F_1$EC-2%SA at 30 °C.

The superior performance of PVdF-NCC cell is also demonstrated by the self-discharge tests that were carried out on the cells fully charged up to 4.95 V at C/10, stored in OCV for 20 h and discharged at C/10; the sequence was repeated for 13 times. The recovered charge of the cell with PVdF-NCC separator were 87% and 84%, at the 2$^{nd}$ and at the last sequence, respectively, whereas those of the cell with Celgard were 83% and 80%. Therefore, these findings suggest that PVdF-NCC separator may mitigate the oxidative electrolyte decomposition that occurs on the cathode surface upon storage in fully charged state at high potentials for different times of OCV, thus improving the cathode/electrolyte interface by promoting the formation of a more stable passivation layer on LNMO surface than the Celgard.

Since high-energy lithium-ion batteries for automotive applications require the use of components stable over cycling, especially at high-rates, the impact of the PVdF-NCC separator on the cycling stability at 1C effective rate was investigated on graphite//LNMO cells featuring electrodes with optimized composition and mass loading highly demanded for hybrid electric vehicles application. Deep 100 galvanostatic charge/discharge cycles between 3.50 and 4.95 V were thus carried out on cells with PVdF-NCC and Celgard separators in LF30 and additives at 30 °C.

Figure 3.17 compares the cycling stability of the cells with PVdF-NCC and Celgard separators at 1C effective rate, i.e. each charge and discharge lasted 1 h, corresponding to 1.89 and 1.67 mA cm$^{-2}$, respectively. These cells display very different behavior over 100 cycles, although delivered almost the same capacity at low current density (C/10, 300 mA cm$^{-2}$), namely 120 with PVdF-NCC and 115 mAh g$^{-1}_{LNMO}$ with Celgard. On the other hand, at the first 1C cycle the PVdF-NCC and the Celgard cells delivered 108 mAh g$^{-1}_{LNMO}$ and 93 mAh g$^{-1}_{LNMO}$, respectively, thus indicating that the Celgard is affected more than the PVdF-NCC cell by the change of current density from low (C/10) to higher ones (1C). Indeed, unlike the PVdF-NCC cell, the Celgard cell displays a rapid capacity decrease of 92% against

of 34% of PVdF-NCC cell over cycling.

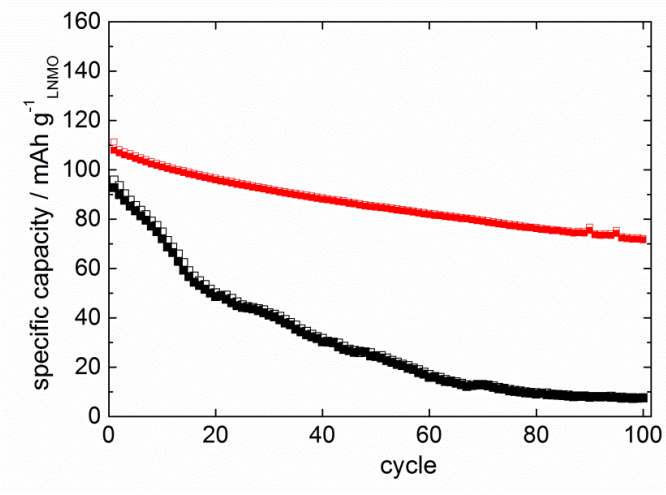


Figure 3.17. Discharge and charge capacities over deep 100 deep charge/discharge galvanostatic cycles at 1C-rate between 3.95 and 4.95 V of graphite//LNMO cells with PVdF-NCC (red symbol) and Celgard®2400 (black symbol) separators in LF30-1.6%$F_1$EC-2%SA. Charge is indicated by void and discharges by full symbols. Reprinted from ref. [118], Copyright (2015), with permission from Elsevier.

Figure 3.18 reports the voltage profile of the 1$^{st}$ and 100$^{th}$ cycle and clearly evinces the higher ohmic drops in the Celgard cell than those in PVdF-NCC cell. Galvanostatic charges followed by 1h constant voltage charge at 4.95 V were also performed; although the capacities improved, the coulombic efficiency worsened without the Celgard cells reaching the capacity values of those with PVdF-NCC. Given that the nickel oxidation potential of LNMO is as high as 4.75 V *vs.* Li, and the cells were charged up to 4.95 V, the findings suggest that higher ohmic drops in the Celgard cells than in the PVdF-NCCs provided lower states of charge for the former.

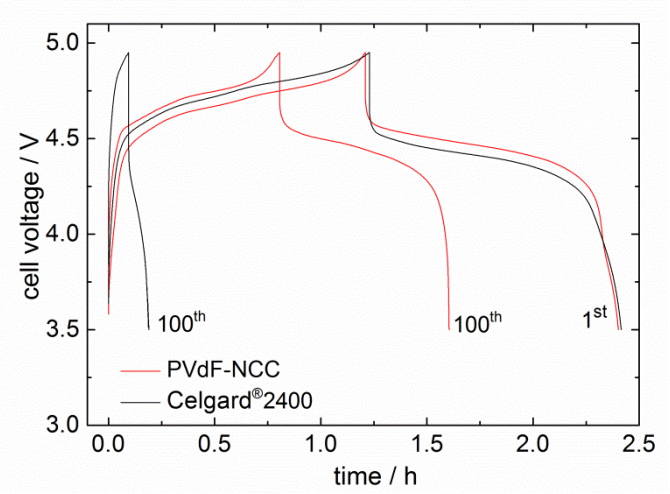


Figure 3.18. Voltage profiles of the 1st and 100th cycle at 1C effective rate of graphite//LNMO cells with PVdF-NCC and Celgard®2400 separators in LF30-1.6%$F_1$EC-2%SA at 30 °C. Reprinted from ref. [119], Copyright (2014), with permission from Elsevier.

This is supported by IS measurements collected on the cells after the first low current cycle and at the end of 100 cycles at 1C as shown in Figure 3.19 and the corresponding IS data at 1 Hz are reported in Table 3.4. The Celgard cell displays much higher resistance than that of PVdF-NCC cell that remains more stable over cycling, as expected.

These results confirm the great beneficial impact of the new macroporous PVdF-NCC separator on electrochemical performance of high-voltage graphite//LNMO cells especially at high C-rates. Therefore, these cells were also tested according to the DOE protocol in view of the use of the LNMO cathode in power-assist and plug-in hybrid electric vehicles and the results will be discussed in Chapter 6.

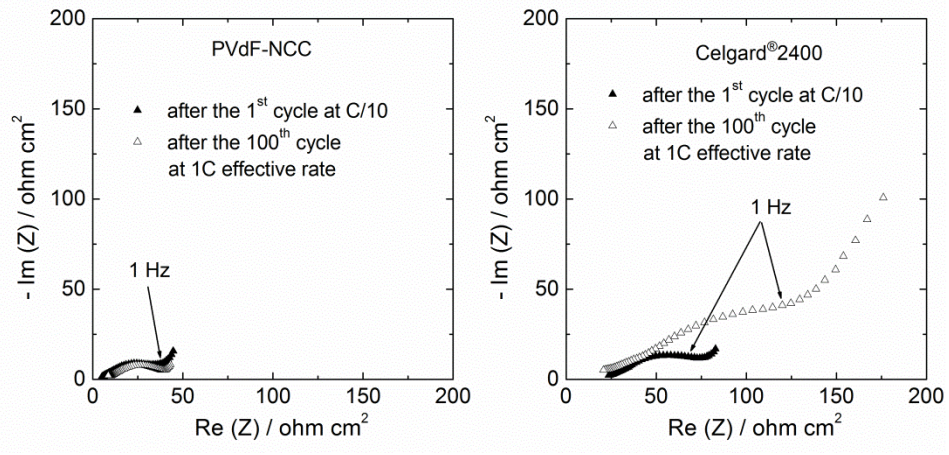


Figure 3.19. Impedance spectra in the range 10 kHz - 0.1 Hz of cells with PVdF-NCC and Celgard®2400 separators with LF30-1.6%$F_1$EC-2%SA after the first C/10-low current cycle and at the end of the 100th cycle at 1C effective rate at 30 °C. Reprinted from ref. [119], Copyright (2014), with permission from Elsevier.

Table 3.4. Internal resistance ($Z_{re}$) at 1 Hz of graphite//LNMO cells in discharge state with PVdF-NCC and Celgard®2400 separators after the first cycle at C/10 and 100 cycles at 1C. Reprinted from ref. [119], Copyright (2014), with permission from Elsevier.

| **graphite//LNMO cells with different separators** | **$Z_{re}$ at 1 Hz / ohm cm$^2$** | |
|---|---|---|
| | **after the 1st cycle at C/10** | **after 100 cycles at 1C effective rate** |
| PVdF-NCC (28 μm) | 35.0 | 69.5 |
| Celgard®2400 (25 μm) | 37.6 | 120.0 |

## 3.3 Conclusions

The study on the use of different electrolytes, i.e. LF30 and LP30 with and without additives, and separators, i.e. PVdF-NCC and Celgard®2400, highlighted the great importance of these cell components in affecting the cycling performance

of high-voltage graphite//$LiNi_{0.4}Mn_{1.6}O_4$ (LNMO) cells. It was proved the strong and beneficial impact of LF30 based electrolytes and PVdF-NCC separator in stabilizing the electrode/electrolyte interface at high operating voltages, by reducing the oxidative electrolyte decomposition thanks to a more stable, protective layer on LNMO surface than that formed in presence of LP30 electrolyte and Celgard. This allows to improve the capacity retention of the high-voltage graphite//LNMO cells over cycling and the self-discharge of the full charged cells up to 4.95 V.

The advantage of the new fluorinated separator can be ascribed both to a better compatibility between the PVdF-NCC membrane and the electrodes which in turn feature a PVdF binder, and to a better affinity of the PVdF-NCC with the carbonate-based electrolyte, as also evinced by the lower MacMullin number of the PVdF-NCC than that of the Celgard. The PVdF-NCC separator, which contributes to the cell resistance much less than Celgard, positively affects the graphite//LNMO cell performance and its importance mainly comes to the fore when high current densities are involved, as displayed by the cycling stability tests at 1 C effective rate over 100 charge/discharge cycles performed on graphite//LNMO cells featuring electrodes with optimized composition and mass loading suitable for scale-up of batteries for hybrid electric vehicle applications. The outstanding results of the cells with PVdF-NCC separator confirmed its beneficial effect on the electrochemical performance of the graphite//LNMO cells, thus highlighting that the use of PVdF-NCC separator in high-voltage lithium-ion batteries is very promising.

# Chapter 4. The role of conducting additives on electrochemical performance of $LiNi_{0.5}Mn_{1.5}O_4$ composite electrodes

Chapter 4 deals with the study on the role of different conducting additives on electrochemical performance of $LiNi_{0.5}Mn_{1.5}O_4$ (LN05MO) composite electrodes in conventional EC : DMC – 1M $LiPF_6$ (LP30) electrolyte, at 30 °C, by using commercial $LiNi_{0.5}Mn_{1.5}O_4$ powder as active material. Two nanometric carbon blacks, Super C65 (C65) and Super P (SP), and a home-made prepared partially reduced graphene oxide (pRGO) as well as a commercial reduced graphene oxide (RGO) were used as conducting additives.

The effect on cycling stability of the LN05MO composite electrodes in limiting the charge-cut-off voltage at 4.8 V is also reported as well as the performance of full cell with graphite anode and LN05MO/pRGO-C65 cathode. Furthermore, the evaluation of lithium diffusion coefficient in LN05MO-based electrodes from cyclic voltammetry data in regard to the discrepancies reported in literature on this matter is discussed.

Elsevier and The Electrochemical Society are acknowledged for the permission to reprint some parts of the following publications:

- S. Monaco, F. De Giorgio, L. Da Col, M. Riché, C. Arbizzani, M. Mastragostino, Electrochemical performance of $LiNi_{0.5}Mn_{1.5}O_4$ composite electrodes featuring carbons and reduced graphene oxide, J. Power Sources, 278 (2015), 733-740, Copyright (2015).
- C. Arbizzani, L. Da Col, F. De Giorgio, M. Mastragostino, F. Soavi, Reduced Graphene Oxide in cathode formulations based on $LiNi_{0.5}Mn_{1.5}O_4$, J. Electrochem. Soc., 162 (10), A2174-A2179. Copyright (2015).

## 4.1 Electrochemical performance of $LiNi_{0.5}Mn_{1.5}O_4$ composite electrodes featuring different carbonaceous additives

The formulation of all the LN05MO composite electrodes was the same in terms of component percentages and is reported in Table 4.1 together with the active material mass loading range. The composite electrodes were labelled according to the component addition type and order, namely LN05MO/C65, LN05MO/SP, LN05MO/pRGO-C65, LN05MO/pRGO-SP, LN05MO/RGO, LN05MO/C65/RGO and LN05MO/RGO/C65. Electrodes of 0.636 $cm^2$ geometric area were tested in LP30 at 30 °C in half cells *vs.* Li in excess with Whatman GF/D separator and Li reference electrode.

A graphite//LN05MO/pRGO-C65 cell with the electrodes balanced in capacity was also assembled and tested in LP30 at 30 °C.

Table 4.1. Formulation and active material mass loading range of the graphite and LN05MO electrodes tested in half or in full cells with LP30 and Whatman GF/D separator at 30 °C.

| **electrode formulation / wt.%** | | **active mass loading / mg $cm^{-2}$** | |
|---|---|---|---|
| **graphite anode** | **LN05MO cathode** | **graphite** | **LN05MO** |
| 89% SLA-1025<br>3% PureBLACK™<br>8% PVdF<br>(Solef®5320) | 85% LN05MO<br>10% conducting additive<br>5% PVdF<br>(Kynar HSV 900) | 3.5 | 2.0 ÷ 12.0 |

### 4.1.1 $LiNi_{0.5}Mn_{1.5}O_4$ characterization

The active material was a commercial submicrometric $LiNi_{0.5}Mn_{1.5}O_4$ (LN05MO) disordered spinel and Figure 4.1, which displays the XRD spectrum recorded on the pristine powder, confirms the nature of the LN05MO *Fd*-3*m* phase.

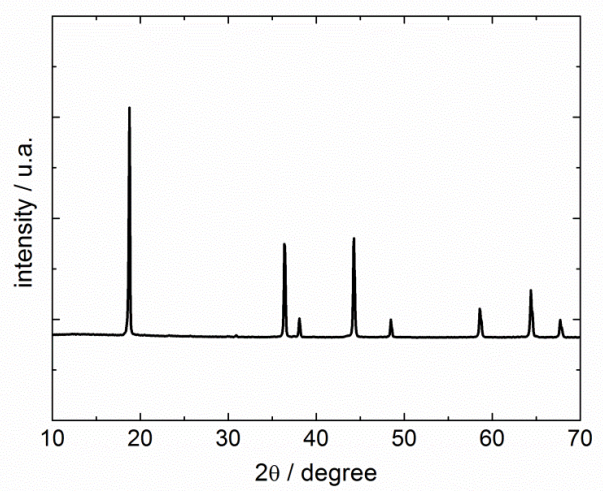


Figure 4.1 XRD pattern of $LiNi_{0.5}Mn_{1.5}O_4$ powder.

The cyclic voltammetry of a thin LN05MO/C65 electrode of Figure 4.2a shows, in addition to the main $A_1$ and $A_2$ peaks at high potentials due to the oxidation of $Ni^{2+}/Ni^{3+}$ and $Ni^{3+}/Ni^{4+}$ upon $Li^+$ de-insertion, a small peak $A_0$ at ca. 4.0 V which is related to the redox couple $Mn^{3+}/Mn^{4+}$. Such presence of $Mn^{3+}$ is the fingerprint of an off-stoichiometric $LiNi_{0.5}Mn_{1.5}O_{4-x}$, which is a typical chemical composition of the *Fd*-3*m* structure. Accordingly, Figure 4.2b which displays the voltage profile of the same electrode during the galvanostatic discharge at C/3 after charge, shows at high potentials the two main reduction plateaus of $Ni^{4+}$ and $Ni^{3+}$ and at ca. 4.0 V that of $Mn^{4+}$ to $Mn^{3+}$ which contributes to the total capacity by ca. 15%.

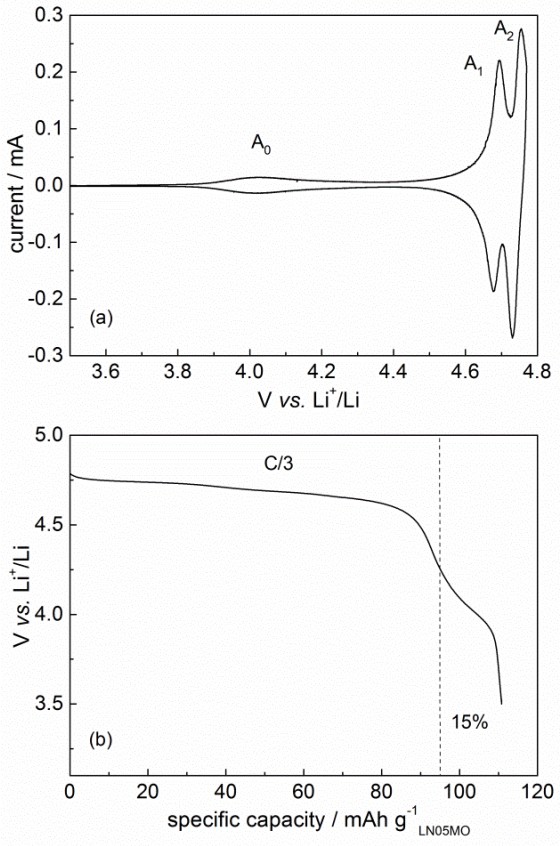


Figure 4.2. (a) Cyclic voltammetry at 50 μV $s^{-1}$ and (b) voltage profile upon galvanostatic discharge at C/3 after charge up to 4.8 V *vs.* Li+/Li of LN05MO/C65 (2.33 $mg_{LN05MO}$ $cm^{-2}$) composite electrode in LP30 at 30 °C. Reprinted from ref. [108], Copyright (2015), with permission from Elsevier.

### 4.1.2 Synthesis and structural characterization of partially reduced graphene oxide

The synthesis of the partially reduced graphene oxide (pRGO) was carried out by microwave irradiation (MW) of commercial graphene oxide (GO), i.e. 130 mg of GO were irradiated at 300 W for 15 seconds. The short irradiation time provided pRGO, as per the XRD spectrum in Figure 4.3 showing the peaks of both RGO (2θ = 26.1°) and GO (2θ = 11.6° and 42.3°).

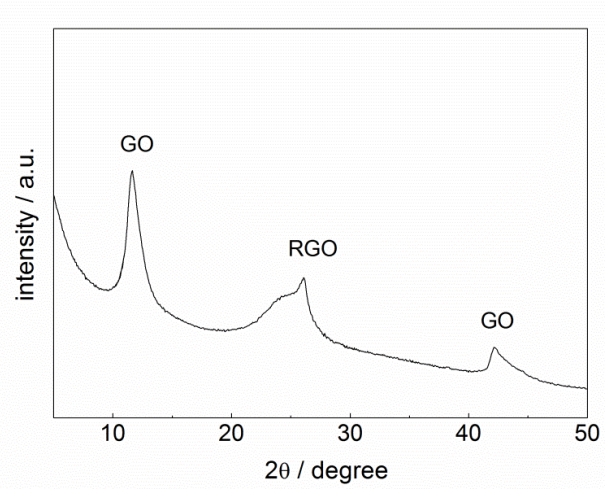


Figure 4.3. XRD pattern of the partially reduced graphene oxide prepared by MW irradiation of commercial graphene oxide. Reprinted from ref. [108], Copyright (2015), with permission from Elsevier.

The residual oxygenated groups on the surface of the pRGO should promote the carbon coating providing an interconnecting network for LN05MO particles able to enhance electronic conductivity of the electrode and to reduce feasible $Mn^{2+}$ dissolution and side-reactions at LN05MO/electrolyte interface.

### 4.1.3 Morphological and electrical characterization of the $LiNi_{0.5}Mn_{1.5}O_4$-based powders

The pRGO-coated LN05MO powder was prepared in anhydrous ethanol, whereas the LN05MO powders featuring RGO and C65 or RGO alone were obtained by simply dry mixing of the components, as reported in Chapter 2 (Paragraph 2.1).

TEM images, which give detailed information regarding the morphology of such composite powders, are shown in Figure 4.4 which also reports the TEM images of the pristine LN05MO, C65, pRGO and RGO. In particular, C65 particles are

connected by *quasi*-one-dimensional networks (4.4b) and the stacked graphene sheets of pRGO (4.4c) and RGO (4.4d) consist of two-dimensional conductive surfaces. The TEM image of the LN05MO/pRGO (4.4e) clearly shows that LN05MO particles are wrapped by pRGO whereas that of the LN05MO/RGO powder (4.4f) shows that the active particles are in contact with at least two large graphene sheets. TEM images of LN05MO/C65 powder (4.4g) shows that large agglomerates of C65 are not uniformly distributed around LN05MO particles. Furthermore, irrespective of the mixing sequence, the composites containing both C65 and RGO consist of C65 particles attached to LN05MO and of RGO sheets dispersed among the C65-LN05MO agglomerates (4.4h and 4.4i).

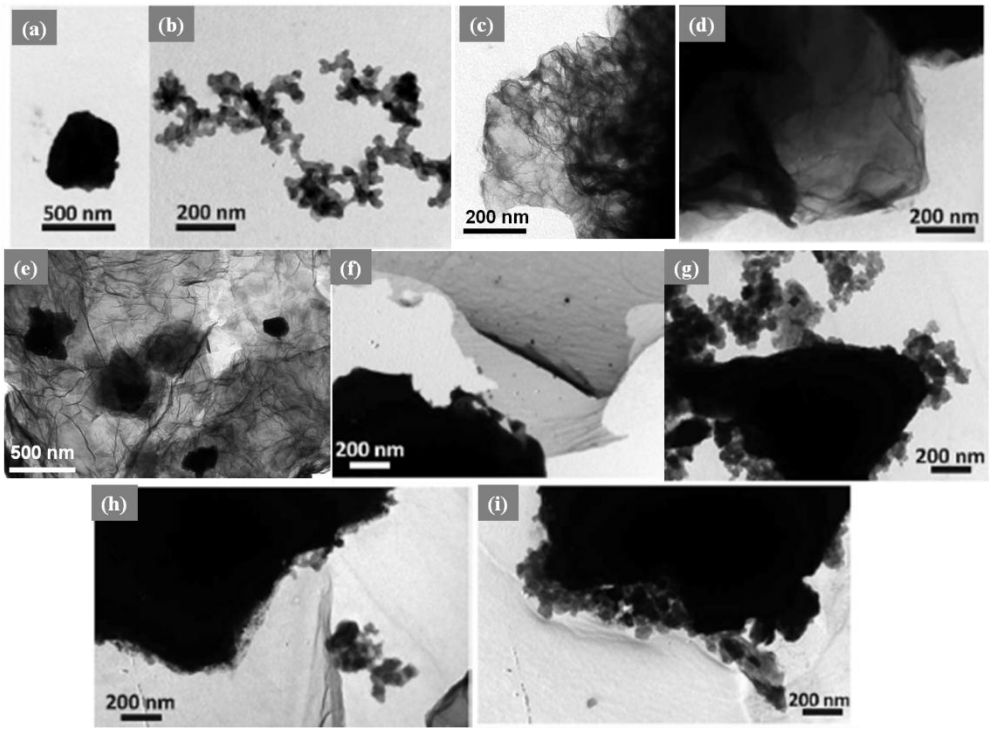


Figure 4.4. TEM images of a) LN05MO (x46000), b) C65 (x92000), c) RGO (x92000), d) pRGO (x92000), e) LN05MO/pRGO (x64000), f) LN05MO/RGO (x64000), g) LN05MO/C65 (x64000), h) LN05MO/RGO/C65 (x64000), (i) LN05MO/C65/RGO (x64000). Reproduced with permission from ref. [120]. Copyright 2015, The Electrochemical Society.

The resistivity measurements performed on composite films deposited on mylar foils, as described in Subsection 2.5.1, provided much lower resistivity values, as reported in Table 4.2, for the LN05MO/C65, LN05MO/pRGO-C65 and LN05MO/C65/RGO composites than for the LN05MO/RGO. This unexpected result on the basis of the very low resistivity of RGO, namely 0.014 ohm cm from NanoInnova datasheet, is presumably due to the tendency of RGO to agglomerate into thickly aggregate structures [71] that does not enable the dispersion of LN05MO particles. The presence of carbon black nanoparticles is thus mandatory in RGO-based composite to hinder RGO's stacking and assure its homogeneous dispersion and, hence, good conductivity values.

Table 4.2 Resistivity values of LN05MO/C65, LN05MO/pRGO-C65 and LN05MO/C65/RGO and LN05MO/RGO composites deposited on mylar foil.

| **composite films** | **resistivity ohm cm** |
|---|---|
| LN05MO/C65 | 4.3 |
| LN05MO/pRGO-C65 | 3.3 |
| LN05MO/C65/RGO | 2.1 |
| LN05MO/RGO | $2.3 \cdot 10^3$ |

### 4.1.4 Electrochemical characterization of $LiNi_{0.5}Mn_{1.5}O_4$ composite electrodes with different carbon blacks as conducting additives

The study on the effect of the different carbon blacks and charge cut-off potentials on the electrochemical performance of the composite electrodes was carried out on LN05MO/C65, LN05MO/SP and LN05MO/pRGO-C65 and LN05MO/pRGO-SP electrodes by charge/discharge cycles in LP30 at 30 °C between 3.50 and 4.80 or 4.85 V *vs.* $Li^+/Li$. LN05MO/C65 and LN05MO/SP electrodes were tested by 50 cycles with charges at C/3 and discharges at C/3, C/2, 1C and 2C (three cycles for each rate) in the voltage range of 3.50 - 4.85 V *vs.* $Li^+/Li$ and Figures 4.5a and 4.5b show the discharge capacity and the percentage

of recovered charge of the two electrodes. Irrespective of the carbon black, these composite electrodes yield almost the same performance with a capacity loss of ca. 23% over 50 cycles.

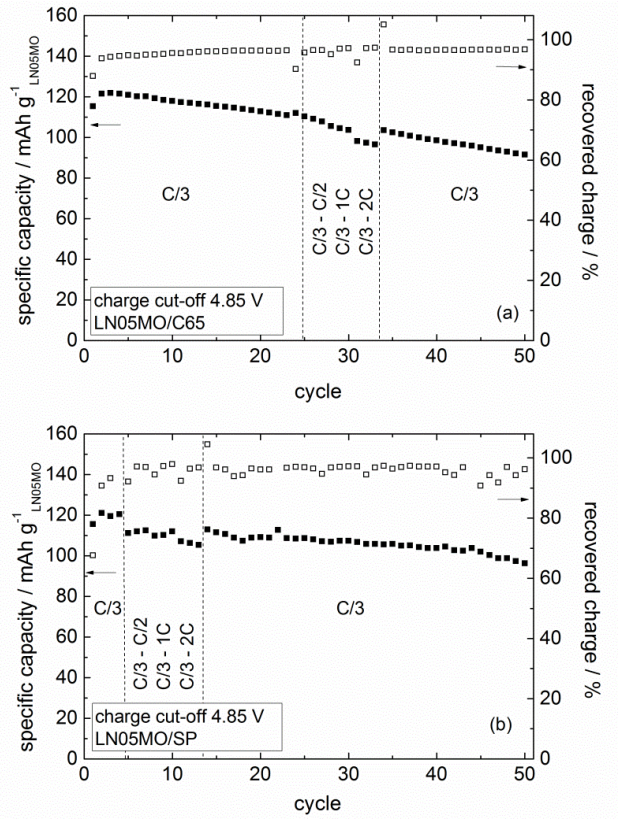


Figure 4.5. Discharge capacity and % of recovered charge over 50 cycles in LP30 at 30 °C of (a) LN05MO/C65 (7.61 $mg_{LN05MO}$ $cm^{-2}$) and (b) LN05MO/SP (7.10 $mg_{LN05MO}$ $cm^{-2}$) electrodes. Reprinted from ref. [108], Copyright (2015), with permission from Elsevier.

It is worth noting that the dissolution of $Mn^{2+}$ from $Mn^{3+}$ disproportion is not the main cause of such capacity loss over cycling, as in ref. [121,122], because the voltage profiles of LN05MO/SP electrode of Figure4.6a upon the galvanostatic charge/discharge cycles at C/3 shows that the manganese contribution to the total discharge capacity remains unchanged (ca. 18 mAh $g^{-1}_{LN05MO}$) by increasing the

number of cycles from the 3rd to the 43rd cycles. By contrast, the discharge overpotentials increase with the increase of cycle number because of the increasing thickness of a passivation surface layer as demonstrated by the impedance data of Figure 4.6b which display that the total discharge resistance increases from 12 ohm $cm^2$ to 60 ohm $cm^2$ after 44 cycles.

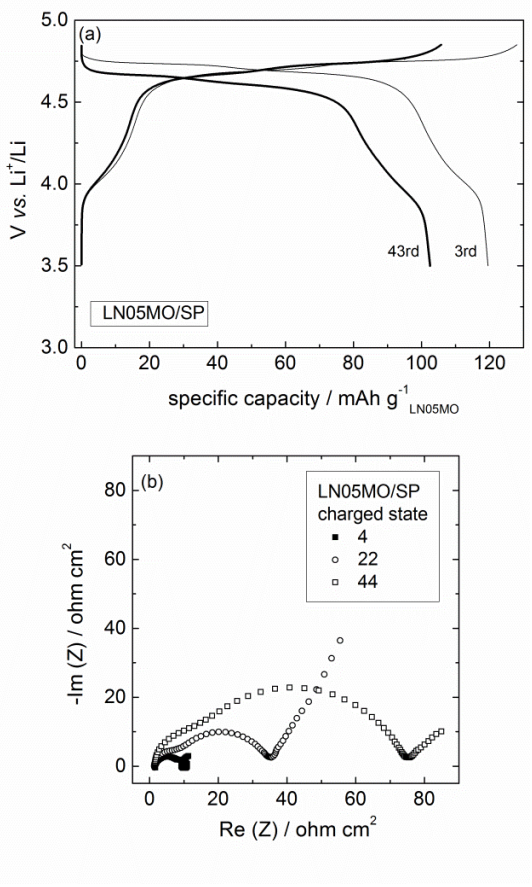


Figure 4.6. (a) Charge/discharge voltage profiles at C/3 of the 3rd and 43rd cycles of LN05MO/SP (7.10 $mg_{LN05MO}$ $cm^{-2}$) electrode and (b) the corresponding impedance spectra of the charged electrode at 4.78 V at different number of cycles. Reprinted from ref. [108], Copyright (2015), with permission from Elsevier.

Since the higher is the charge-cut-off potential, more facilitated are the side-reactions between the LN05MO cathode and the electrolyte which suffers from oxidative decomposition at high potentials, the effect of the decrease of the charge cut-off voltage at 4.80 V was investigated. The LN05MO/SP electrodes performed 70 charge/discharge cycles at 1C with charges up to 4.80 or 4.85 V and discharges down to 3.5 V. The discharge capacity values of the electrode charged up to 4.85 V are shown in Figure 4.7a and those of the electrode charged up to 4.80 V, with the last 10 cycles involving constant current and constant voltage (CC-CV) charges, in Figure 4.7b.

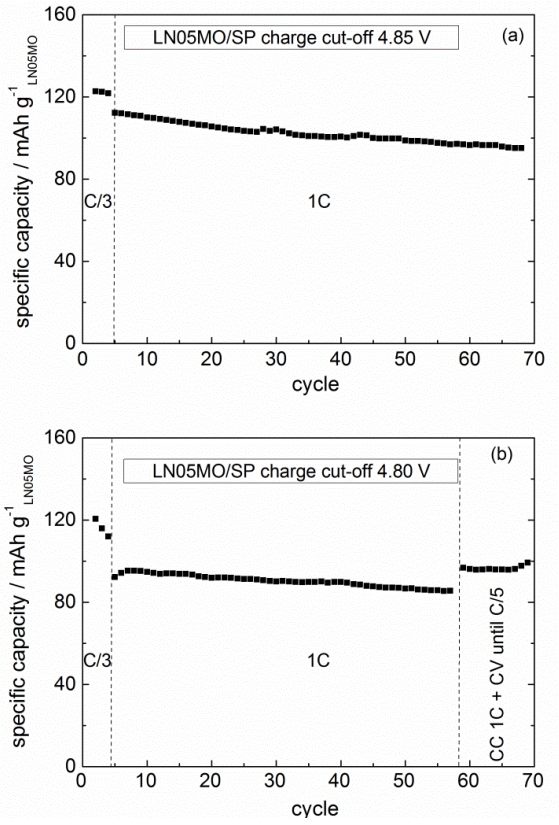


Figure 4.7. Discharge capacity over charge/discharge cycles of LN05MO/SP electrodes charged at 1C up to(a) 4.85 V (6.43 $mg_{LN05MO}$ $cm^{-2}$) and up to (b) 4.80 V (8.06 $mg_{LN05MO}$ $cm^{-2}$) in LP30 at 30 °C. Reprinted from ref. [108], Copyright (2015), with permission from Elsevier.

The electrode cycled up to 4.85 V initially delivered at 1C capacity values slightly higher than those of the electrode cycled up to 4.80 V, which in turn recovers capacity with the CC-CV cycles, as expected, but withstands a higher capacity loss than the electrode cycled up to 4.80 V, i.e. 15% against 7%, respectively. However, even the electrode cycled up to 4.85 V after 50 cycles at 1C displays a capacity loss that is two-fold lower than that of electrodes mainly tested at C/3 in the same voltage range (compare Figure 4.7a against Figure 4.5a), and this indicates the beneficial effect of the high C-rates on the electrode stability.

The impedance spectra of such two LN05MO/SP electrodes cycled up to 4.85 and 4.80 V are shown in Figure 4.8a and 4.8b, respectively. Figure 4.8b also includes the impedance spectrum of the charged electrode after the 4th cycle at the beginning of 1C-cycling.

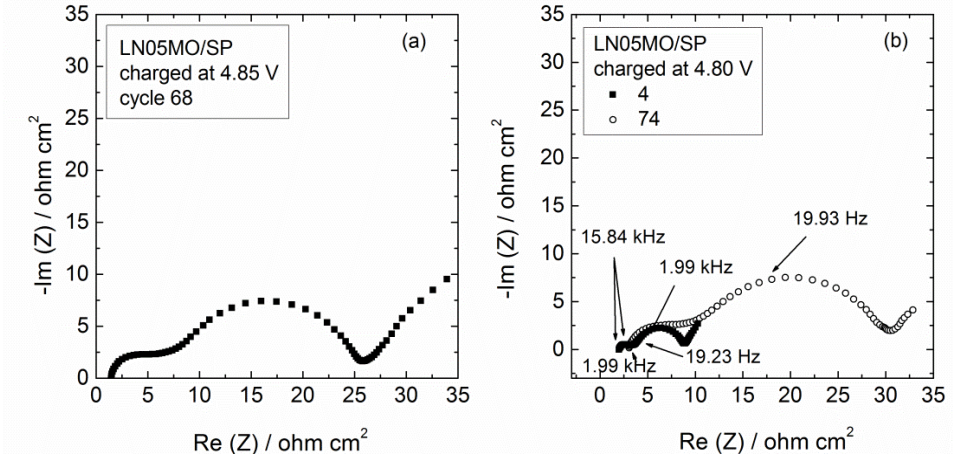


Figure 4.8. Impedance spectra of the LN05MO/SP electrodes in the charged state at 4.75 V at the end of the cycling at 1C up to(c) 4.85 V (6.43 $mg_{LN05MO}$ $cm^{-2}$) and up to (d) 4.80 V (8.06 $mg_{LN05MO}$ $cm^{-2}$); the spectrum of the charged electrode at the $4^{th}$ cycle overlaps in 4.8b. Reprinted from ref. [108], Copyright (2015), with permission from Elsevier.

Both electrodes at the last cycle show similar total resistance values, which are less than one-half that of the electrode cycled at C/3 (see Figure 4.6b), clearly

demonstrating that thinner layers are formed on the surface of the LN05MO cathodes cycled at 1C. This clearly demonstrates that the C-rate and the charge cut-off voltage play a crucial role in influencing the cycling stability of the high-voltage LN05MO cathode.

In order to identify the phenomena that take place during cycling, impedance spectroscopy measurements on the LN05MO/SP electrode were carried out even at different states of charge (in the potential range 3.50 V and 4.83 V) during the 4$^{th}$ cycle and selected spectra are shown in Figure 4.9. The Figure also displays the equivalent circuit used to fit each spectrum, which includes uncompensated resistance, $R_u$, in series with the three parallel R/Q and $Q_W$, where Q symbolizes the constant phase element. Mathematically the admittance of the constant phase element is given by Equation 4.1:

$$Y(\omega) = Y_0 (j\,\omega)^{\alpha} \tag{4.1}$$

where $Y_o$ represents an ideal capacitance if $\alpha = 1$ and a Warburg element if $\alpha = 0.5$.[123]

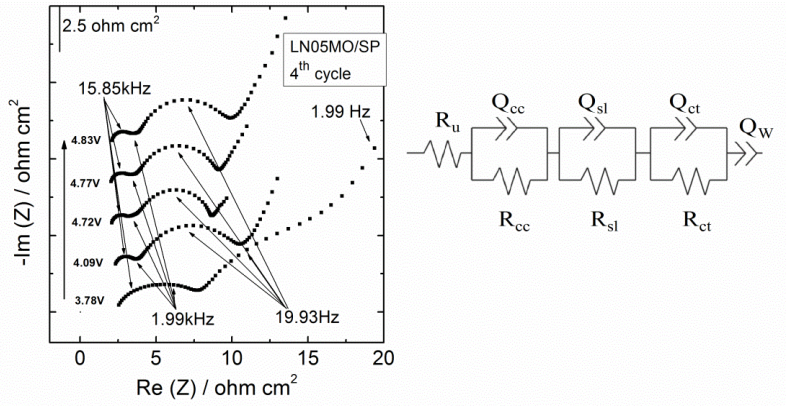


Figure 4.9. Selection of impedance spectra (100 kHz - 50 mHz) of LN05MO/SP electrode (8.06 $mg_{LN05MO}$ $cm^{-2}$) during the charge of the 4th cycle in LP30 at 30 °C and scheme of the equivalent circuit used to fit each spectrum. Reprinted from ref. [108], Copyright (2015), with permission from Elsevier.

The fitting data to the equivalent circuit displayed in Figure 4.9 showed that the $R_{cc}$ resistance related to the first semicircle at the highest frequency remains nearly constant and low (< 1 ohm $cm^2$) over all the $Li^+$ de-insertion with capacitance values of 10 µF $cm^{-2}$ ($\alpha_{cc}$ parameter of the $Q_{cc}$ was equal to 1 and, thus, $Q_{cc}$ represents an ideal capacitor). This suggested that this semicircle is related to aluminum current collector. The second semicircle at high frequency displayed resistance $R_{sl}$ values which initially decrease with the $Li^+$ de-insertion becoming comparable to $R_{cc}$ and the related $Q_{sl}$ non-ideal capacitance values ($\alpha_{sl}$ parameters were 0.8) increased and remained almost constant at 2 mF $s^{(\alpha-1)}$ $cm^{-2}$. This second semicircle was attributed to the passivation surface layer. The semicircle at high-medium frequency was attributed to the charge-transfer reaction and displayed resistance $R_{ct}$ values which significantly decreased from 13 ohm $cm^2$ to 5 ohm $cm^2$, remaining almost constant after complete $Mn^{3+}$ oxidation. The related $Q_{ct}$ non-ideal capacitance values ($\alpha_{ct}$ parameters were 0.9) were around 3 mF $s^{(\alpha-1)}$ $cm^{-2}$ . The constant phase element $Q_W$ at the low frequency displayed $\alpha_w$ values that were very far from 1 and near to the Warburg element frequency dependence. Therefore, $Q_W$ is nearly representative of the $Li^+$ diffusion in the solid electrode.

As per equivalent circuit *supra*, the impedance spectrum at the end of cycling at 1C of Figure 4.8b was also analyzed and Table 4.3 compares the fitting parameters of the spectra of the charged electrode at the $4^{th}$ and $74^{th}$ cycles.

The data of Table 4.3 clearly show that both $R_{sl}$ and $R_{ct}$ increase four/five-fold upon cycling and $R_{ct}$, being five times higher than $R_{sl}$, contributes most to the total electrode resistance. Furthermore, $Q_{sl}$ significantly decreases together with the $R_{sl}$ increase over cycling, thus indicating the growth of a solid passivation film of low electronic conductivity, which in turn is responsible for the increase of $R_{ct}$.

Table 4.3. Fitting parameters and $\chi^2$ of the impedance spectra of the charged LN05MO/SP electrode of Figure 4.8b; the α parameters of the constant phase elements are in brackets. Reprinted from ref. [108], Copyright (2015), with permission from Elsevier.

| cycle | $R_u$ | $R_{cc}$ | $R_{sl}$ | $R_{ct}$ | $Q_{cc}$ | $Q_{sl}$ | $Q_{ct}$ | $Q_W$ | $\chi^2$ |
|---|---|---|---|---|---|---|---|---|---|
| | ohm $cm^2$ | | | | $F\ s^{(\alpha-1)}cm^{-2}$ | | | | |
| 4 | 2.1 | 1.0 | 0.8 | 4.9 | 9.8E-06 (1.00) | 1.0E-03 (0.82) | 2.2E-03 (0.92) | 4.6E-01 (0.67) | 0.019 |
| 74 | 3.1 | 2.9 | 4.1 | 19.8 | 9.3E-06 (0.98) | 1.7E-04 (0.83) | 1.1E-03 (0.80) | 2.6E-01 (0.60) | 0.009 |

### 4.1.5 Electrochemical characterization of $LiNi_{0.5}Mn_{1.5}O_4$ composite electrodes with different carbon blacks and partially reduced graphene oxide as conducting additives

The LN05MO/electrolyte interface film formed upon cycling is highly detrimental to overall electrode resistance, and with the aim to limit its increase in thickness over cycling, composite electrodes featuring LN05MO coated with pRGO were prepared and mixed with carbon SP or C65.

Figure 4.10 compares data of discharge capability test performed on LN05MO composite electrodes with pRGO, namely LN05MO/pRGO-SP, and without pRGO, namely LN05MO/SP. Both electrodes were charged (excluding the first three CC cycles at C/3) at 1C constant current up to 4.8 V followed by a constant voltage step until the current decreases at a value corresponding to that of a C/7, and subsequently discharged down to 3.5 V at different C-rates, as indicated in the Figure (15 cycles per each discharge rate, excluding the last cycles at 1C). The data clearly show that the LN05MO/pRGO-SP electrode performs notably better than the LN05MO/SP, particularly at the highest discharge rate.

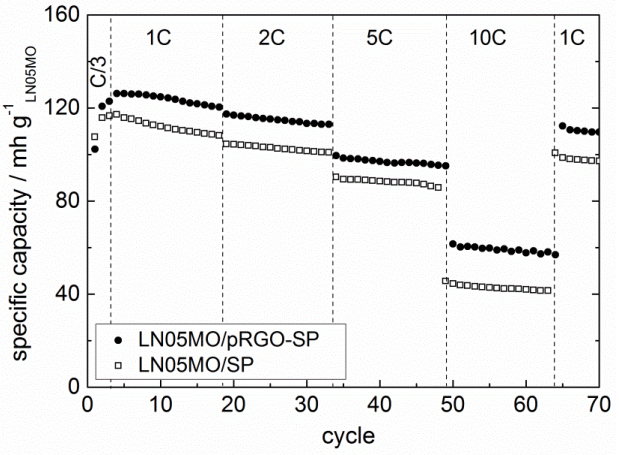


Figure 4.10. Charge CC-CV (1C- 4.8 V until C/7) and discharge CC: C/3, 1C, 2C, 5C, 10C and 1C, of LN05MO/SP (7.28 $mg_{LN05MO}$ $cm^{-2}$) (void symbol) and LN05MO/pRGO-SP (7.49 $mg_{LN05MO}$ $cm^{-2}$) (full symbol) electrodes upon discharge capability test in LP30 at 30 °C. Reprinted from ref. [108], Copyright (2015), with permission from Elsevier.

The results of galvanostatic tests performed at high C-rates (1C, 2C and 3C) between 3.50 and 4.80 or 4.85 V on LN05MO/pRGO-C65 and on LN05MO/C65 for a comparison are shown in Figure 4.11. Even the pRGO-coated electrode featuring C65 showed superior performance than that with C65 alone in term of delivered charge and cycling stability. Over more than 100 cycles the LN05MO/pRGO-C65 electrode displayed a capacity loss less than 10% instead of 20% of the electrode without pRGO.

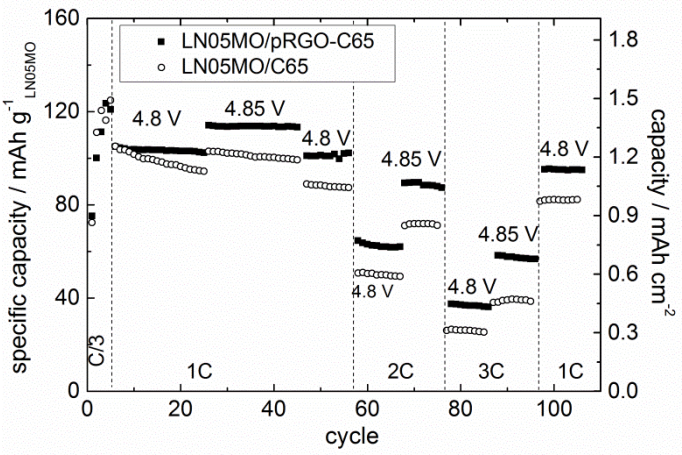


Figure 4.11. Discharge capacity over charge/discharge cycles of LN05MO/pRGO-C65 (11.94 $mg_{LN05MO}$ $cm^{-2}$) (full symbol) and LN05MO/C65 (12.09 $mg_{LN05MO}$ $cm^{-2}$) (void symbol) electrodes at different C-rate charged up to 4.80 and 4.85 V (five conditioning cycles at C/3 were carried out at the beginning) in LP30 at 30 °C. Reprinted from ref. [108], Copyright (2015), with permission from Elsevier.

The impedance spectra of Figure 4.12 confirm the beneficial effect of pRGO's coating on cycling stability. As expected, unlike the LN05MO/C65 electrode, the fully charged LN05MO/pRGO-C65 electrode showed a slowly increase of the total resistance over cycling up to a value of 22 ohm $cm^2$, including uncompensated resistance. The results of the fitting analysis of the selected spectra (Figure 4.12) are reported in Table 4.4: the best fits were obtained to the equivalent circuit featuring a resistance in series with two parallel R/Q and $Q_W$, and the R values at the highest frequencies include $R_u$ and $R_{cc}$.

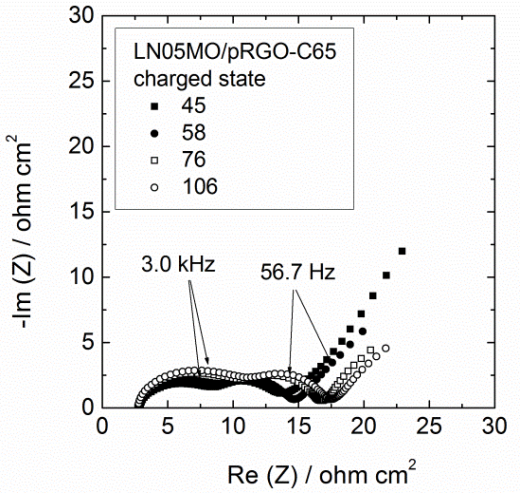


Figure 4.12. Impedance spectra of the LN05MO/pRGO-C65 electrode (11.94 $mg_{LN05MO}$ $cm^{-2}$) in the charged state at 4.76 V at different number of cycles in LP30 at 30 °C. Reprinted from ref. [108], Copyright (2015), with permission from Elsevier.

Table 4.4. Fitting parameters and $\chi^2$ of the impedance spectra of the charged LN05MO/pRGO-C65 electrode of Figure 4.11b; the α parameters of the constant phase elements are in brackets. Reprinted from ref. [108], Copyright (2015), with permission from Elsevier.

| **cycle** | **R** | **$R_{sl}$** | **$R_{ct}$** | **$Q_{sl}$** | **$Q_{ct}$** | **$Q_W$** | **$\chi^2$** |
|---|---|---|---|---|---|---|---|
| | | **ohm $cm^2$** | | | **F $s^{(\alpha-1)}cm^{-2}$** | | |
| 45 | 2.8 | 4.6 | 6.7 | 6.4E-05 (0.77) | 4.0E-03 (0.62) | 3.8E-01 (0.59) | 0.033 |
| 58 | 2.6 | 5.3 | 6.8 | 4.9E-05 (0.80) | 2.4E-03 (0.68) | 7.0E-01 (0.57) | 0.035 |
| 76 | 2.7 | 6.4 | 7.7 | 3.5E-05 (0.80) | 2.0E-03 (0.67) | 9.7E-01 (0.59) | 0.031 |
| 106 | 2.6 | 6.6 | 8.3 | 2.6E-05 (0.83) | 1.9E-03 (0.66) | 8.5E-01 (0.57) | 0.035 |

The beneficial effect of pRGO's coating on cycling stability was also evaluated over more than 100 cycles at 1C on LN05MO/pRGO-SP electrodes in the voltage

range 3.5 and 4.8 V, as shown in Figure 4.13. The Figure displays the very good cycling stability of the pRGO-based electrode with a capacity retention of 87% at the end of the cycling test at 1C. It is worth noting that all the results with pRGO are fully in agreement with those recently reported in ref. [70].

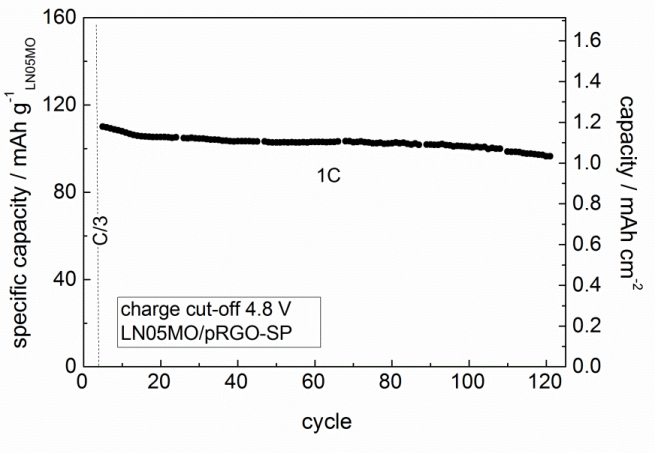


Figure 4.13. Discharge capacity over charge/discharge cycles at 1C of the LN05MO/pRGO-SP electrode (10.70 $mg_{LN05MO}$ $cm^{-2}$) charged up to 4.80 V in LP30 at 30 °C. Reprinted from ref. [108], Copyright (2015), with permission from Elsevier.

### 4.1.6 Electrochemical characterization of $LiNi_{0.5}Mn_{1.5}O_4$ composite electrodes with carbon black Super C65 and reduce graphene oxide as conducting additives

The electrochemical characterization of composite electrodes featuring the commercial reduced graphene oxide (RGO), aimed to evaluate the effect of RGO addition and its dry mixing to other components, was carried out on the following composite electrodes: LN05MO/RGO/C65, LN05MO/C65/RGO, LN05MO/RGO and LN05MO/C65, where the electrode codes are referred to the component addition order. In particular, LN05MO/RGO/C65 indicates that RGO and LN05MO were dry mixed, then C65 was added and mixed; LN05MO/C65/RGO indicates that

RGO was dry mixed with the already mixed LN05MO/C65 powder; LN05MO/RGO and LN05MO/C65 indicate that RGO or C65 were dry mixed with LN05MO. Figure 4.14 shows the results of discharge capability tests in LP30 at 30 °C, with charge at C/3 and discharge in the range from C/3 to 10 C (3 cycles at each rate) between 3.5 and 4.8 V *vs.* $Li^+/Li$.

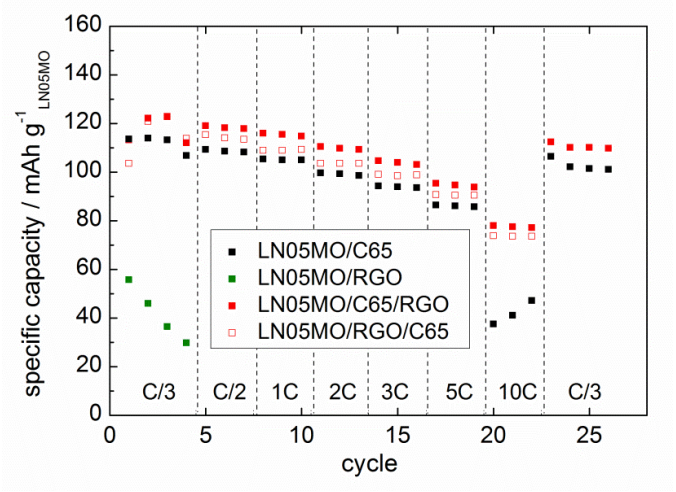


Figure 4.14. Discharge capacity at different C-rates of the LN05MO/C65 (4.40 mg $cm^{-2}$), LN05MO/RGO (4.96 mg $cm^{-2}$), LN05MO/C65/RGO (4.06 mg $cm^{-2}$) and LN05MO/RGO/C65 (4.92 mg $cm^{-2}$) electrodes charged at C/3 in LP30 at 30 °C. Reproduced with permission from ref. [120]. Copyright 2015, The Electrochemical Society.

These data clearly demonstrates that RGO in presence of C65, both mixed with LN05MO before the C65 addition or added to the LN05MO/C65 mixture, positively affect the rate capability performance of LN05MO, especially at high rate. By contrast, RGO alone is not able to assure good cyclability despite its lower electronic resistivity with respect to C65 (0.014 ohm cm *vs.* 0.2 ohm cm, values from data sheets), because the resistivity of the LN05MO/RGO composite film is very high compared to those of the other composite films (see Table 4.2 in Subsection 4.1.3) for the tendency of RGO to agglomerate into thickly aggregate

structures [71] that does not enable the dispersion of LN05MO particles and a good electric contact among them. Furthermore, low polarizations for intercalation/de-intercalation processes require good electronic transport process coupled with fast ionic transport properties, and RGO when is present in high percentage (10%) as in LN05MO/RGO electrodes can hinders $Li^+$ ion migration because its two-dimensional structure may occlude some $Li^+$ paths in LN05MO composites and the lithium ion is forced to increase the path length to reach the electrochemical reaction site.[124–126]

All the electrochemical results of Figure 4.14 are in agreement with the resistivity data in Table 4.2. The good electric contact between the conductive agents and LN05MO particles due to the carbon black nanoparticles that homogeneously disperse RGO hindering its stacking in the LN05MO/C65/RGO composite provides an electrode of low resistivity and fast $Li^+$ transport and, thus, polarizations are less crucial and allow to recover charge even at high C-rate.

The beneficial impact of RGO in combination with C65 was also demonstrated by the cycling stability of the LN05MO composite electrodes tested by deep galvanostatic charge/discharge cycles at 1C, after the conditioning cycles at C/3 rate, as shown in Figure 4.15. The electrodes containing RGO and C65 display superior stability than the electrode with C65 alone, showing a capacity retention of 92% after 100 cycles at 1C against 70% of the electrode with C65 alone. The coulombic efficiency of all electrodes was low in the first conditioning cycles, owing to the irreversible processes responsible in part for the formation of a passivation layer on the cathode surface. However, the coulombic efficiency increased over cycling, although in some cycles it decreased due to the rebuilding of the surface layer, which may have broken down during the preceding cycle.

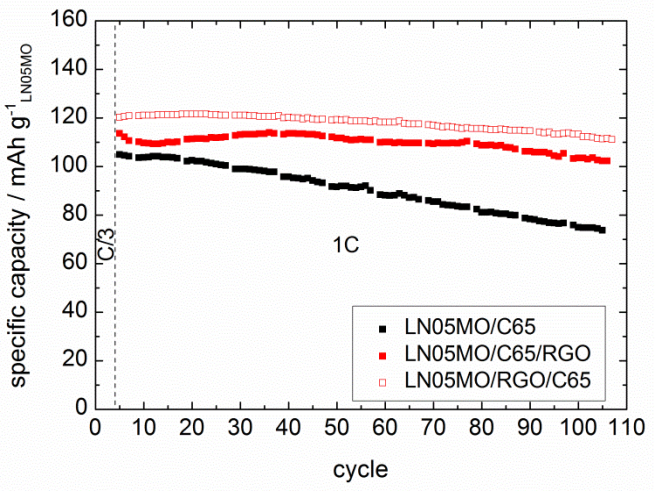


Figure 4.15. Stability tests upon galvanostatic charge/discharge cycles at 1C of the LN05MO/C65 (9.30 mg $cm^{-2}$), LN05MO/C65/RGO (9.58 mg $cm^{-2}$) and LN05MO/RGO/C65 (6.12 mg $cm^{-2}$) electrodes in LP30 at 30 °C.

The sharper capacity loss over cycling of the LN05MO/C65 than that of the LN05MO with RGO is not related to metal dissolution upon cycling, as clearly shown by the discharge voltage profiles of the 87$^{th}$ cycle of the LN05MO/C65 and LN05MO/RGO/C65 electrodes which display the characteristic plateau of $Mn^{4+}$ reduction to $Mn^{3+}$ at around 4.0 V (Figure 4.16). This was also confirmed by the cyclic voltammograms carried out before and after the discharge capability tests and displayed in Figure 4.17 which shows that the $Mn^{3+}/Mn^{4+}$ peak at ca. 4.0 V did not change for both the LN05MO/RGO/C65 and LN05MO/C65 electrodes.

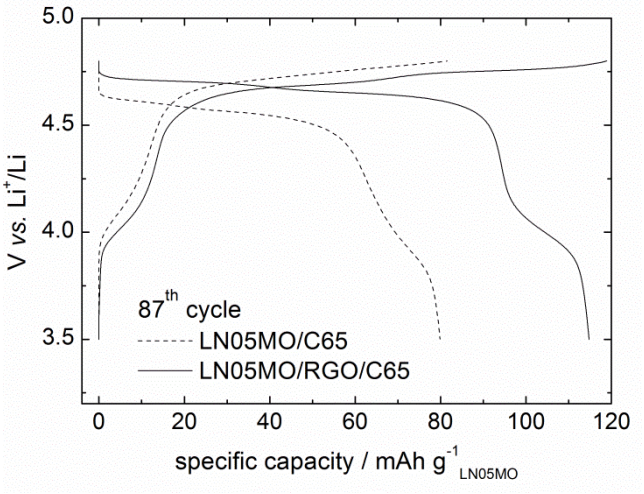


Figure 4.16. Charge and discharge voltage profiles of the 87$^{th}$ cycle of the LN05MO/C65 and LN05MO/RGO/C65 electrodes upon cycling stability test (charge and discharge at 1C) in LP30 at 30 °C. Reproduced with permission from ref. [120]. Copyright 2015, The Electrochemical Society.

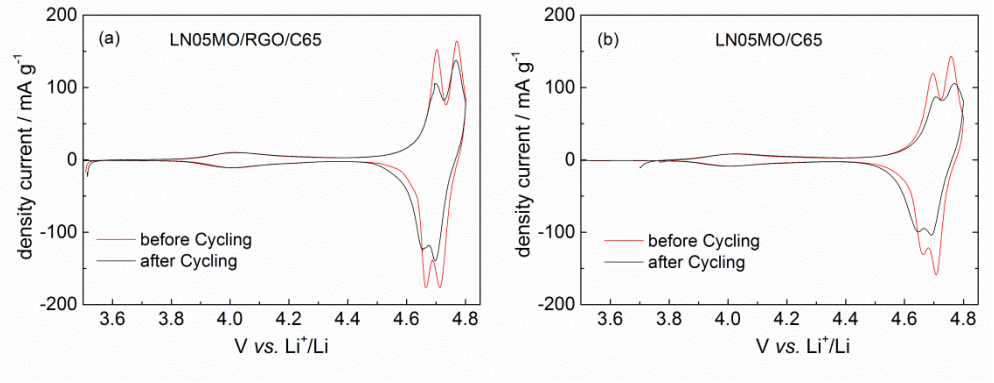


Figure 4.17. Cyclic voltammetries at 50 μV s$^{-1}$ of (a) LN05MO/RGO/C65 and (b) LN05MO/C65 electrodes before and after cycling in LP30 at 30 °C.

Such findings indicate that the amount of $Mn^{3+}$ in LN05MO is maintained the same over cycling, being in good agreement with the results previously discussed in Subsection 4.1.4 for LN05MO/SP electrode. Furthermore, the ratio between Mn and Ni did not change before and after cycling for all the electrodes as evinced by

energy-dispersive X-ray spectroscopy (EDX) analysis. On the other hand, it has been reported that only cycling and storage of the electrodes at high temperature (60 °C) cause local Mn and Ni dissolution.[127]

Morphologic information regarding the LN05MO cathode evolution after electrochemical tests (hereinafter referred to as "cycled" electrode) were obtained by SEM images (Figures 4.18a-d). The pristine LN05MO/C65 cathode shows a rather clean LN05MO surface covered by C65 (4.18a) compared to the cycled electrode which shows a more compact, coated-like morphology (4.18b). On the other hand, the LN05MO/RGO/C65 pristine and cycled electrodes (Figures 4.18c and 4.18d) displays more or less the same morphology without clearly evincing a passivation layer on the particles.

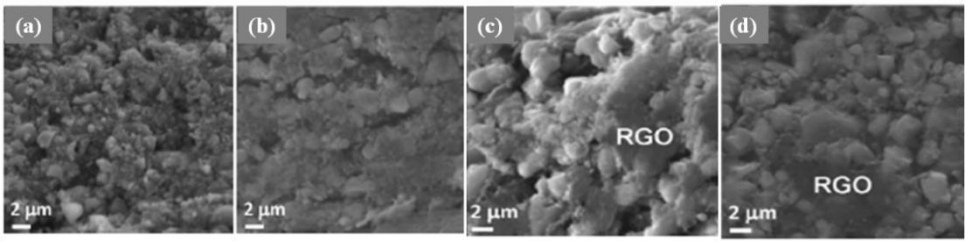


Figure 4.18. SEM images (x10000) of a) pristine LN05MO/C65, b) cycled LN05MO/C65, c) pristine LN05MO/RGO/C65 and d) cycled LN05MO/RGO/C65 electrodes. Reproduced with permission from ref. [120]. Copyright 2015, The Electrochemical Society.

The FT-IR spectra of the pristine and cycled electrodes were carried out and the results are compared in Figure 4.19 which shows displays the related spectra obtained by scrapping the powders off from the pristine and the cycled cathodes. All the spectra show three small signals at ca. 840 $cm^{-1}$, 880 $cm^{-1}$ and 1180 $cm^{-1}$ attributable to PVdF [128] and at 1278 and 1398 $cm^{-1}$ that may be attributable to $Li_2CO_3$ and δC-H.[129] No new band or peak appears in cycled LN05MO/RGO/C65 compared to the spectrum of cycled LN05MO/C65 which, in turn, shows two new spectral features at 1630 $cm^{-1}$ and at 750 $cm^{-1}$. The former can be assigned to the

O=C—O asymmetric stretch mode characteristic of alkyl carbonates, which are presumably formed on $LiNi_{0.5}Mn_{1.5}O_4$ electrodes,[128] and the latter can be assigned to LiF.[130] The new peaks support the assumption that the decomposition reactions in LN05MO/C65 are more facilitated with respect to those occurring in LN05MO/RGO/C65. It is worth noting that the lack of these peaks in LN05MO/RGO/C65 cannot be taken as an indicator that the passivation layer is absent. Although SEI should include P-based moieties, the FT-IR spectra did not show any related signal.

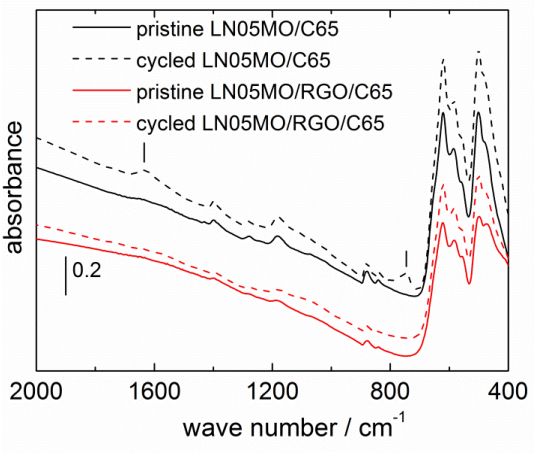


Figure 4.19. FT-IR spectra of pristine (solid line) and cycled (dashed line) LN05MO/C65 (9.30 $mg_{LN05MO}$ $cm^{-2}$) (black line) and LN05MO/RGO/C65 (6.12 $mg_{LN05MO}$ $cm^{-2}$) (red line) electrodes. The cycled electrodes were recovered from cells which performed 100 galvanostatic charge/discharge cycles at 1C in LP30 at 30 °C. Reproduced with permission from ref. [120]. Copyright 2015, The Electrochemical Society.

However, EDX analysis confirmed that the phosphorous is present only in cycled electrodes and that it is present in lower amount in LN05MO/RGO/C65 electrode (0.3 wt.%) than in LN05MO/C65 (1 wt.%), thus suggesting that the formation of the passivation layer is minimized in the former electrode due to the presence of RGO that may limit the electrolyte decomposition on the cathode

surface. Although the fluorine concentration cannot be considered as an indicator of the surface layer since F is present in PVdF binder and, hence, also in pristine LN05MO electrodes, EDX analysis demonstrated that the F content increases from 10.0 wt.% in the pristine LN05MO/C65 electrode to 28.4 wt.% in cycled LN05MO/C65 and from 9.0 to 13.4 wt.% in LN05MO/RGO/C65.

Given that the FT-IR and EDX measurements were performed *ex-situ* after electrode removal from the cell, rinsing and, for FT-IR analysis, scraping the materials off the current collector, the electrode surface could be thus affected by this manipulation and testing in air; therefore, in order to investigate the electrode/electrolyte interface changes occurring over cycling the electrodes were also characterized by impedance spectroscopy measurements during cell operation.

The EIS spectra of LN05MO/C65, LN05MO/RGO, LN05MO/RGO/C65 and LN05MO/C65/RGO electrodes in the charged state were collected after the 3rd cycle at 1C (7th total cycle) and then every ten-twenty cycles. The related spectra shown in Figures 4.20a, 4.20c and 4.20d were collected after $27^{th}$, $47^{th}$, $67^{th}$ and $87^{th}$ cycles and were analyzed with the equivalent circuit $R_u(R_{sl}Q_{sl})(R_{ct}Q_{ct})Q_w$, where $R_u$ is the uncompensated resistance, $R_{sl}$ and $Q_{sl}$ are related to the cathode surface layer, $R_{ct}$ and $Q_{ct}$ are related to charge-transfer reaction and $Q_W$ is representative of the $Li^+$ diffusion in the solid electrode. $R_{sl}$ and $R_{ct}$ of LN05MO/C65, LN05MO/C65/RGO and LN05MO/RGO/C65 increased over cycling, indicating that the cathode surface layer was growing and that the kinetics of the $Li^+$ insertion processes slowed over cycling. However, this trend is less pronounced when RGO is added. The impedance spectra of LN05MO/RGO electrode collected after the $7^{th}$ and $17^{th}$ cycles are also reported in Figure 4.20b for comparison. The expected high resistance values may be ascribed to the stacking/agglomeration of RGO particles discussed above, thus justifying the poor cycling performance of LN05MO/RGO electrode shown in Figure 4.14.

The impedance spectroscopy analysis clearly demonstrates that the introduction

of the reduced graphene oxide and carbon black in LN05MO composite electrodes decreases the total resistance values over cycling, thus explaining the better electrochemical performance of LN05MO/RGO/C65 and LN05MO/C65/RGO with respect to the LN05MO electrode with C65 alone. Therefore, these results confirm that the RGO can effectively slow down the side-reactions at the LN05MO/electrolyte interface.

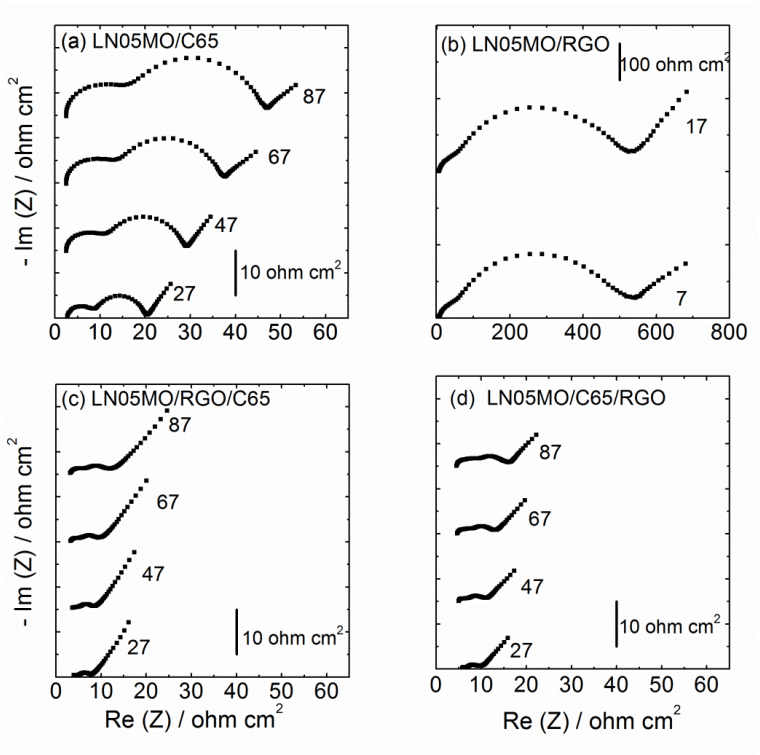


Figure 4.20. Nyquist plots of different electrodes in their charged state over cycling in LP30 at 30 °C: a) LN05MO/C65 (4.40 $mg_{LN05MO}$ $cm^{-2}$), b) LN05MO/RGO (4.96 $mg_{LN05MO}$ $cm^{-2}$), c) LN05MO/RGO/C65 (4.92 $mg_{LN05MO}$ $cm^{-2}$), d) LN05MO/C65/RGO (4.06 $mg_{LN05MO}$ $cm^{-2}$). Reproduced with permission from ref. [120]. Copyright 2015, The Electrochemical Society.

### 4.1.7 Graphite//$LiNi_{0.5}Mn_{1.5}O_4$/pRGO-C65 cell

In view of the use of the LN05MO-based electrodes in full cell for plug-in hybrid electric vehicle applications, a LN05MO/pRGO-C65 cathode (composite weight of 6.36 mg $cm^{-2}$) was combined with a graphite anode (composite weight of 3.96 mg $cm^{-2}$) and tested in LP30 at 30 °C. Before cell assembly, the two electrodes were conditioned by charge/discharge cycles at C/3 and 1C (three cycles for each C-rate), providing a capacity of 0.80 mAh $cm^{-2}$ at 1C, corresponding to 229 mAh $g^{-1}$ for the graphite and 101 mAh $g^{-1}$ for the LN05MO.

The graphite//LN05MO-pRGO-C65 cell performed five deep charge/discharge cycles between 3.00 and 4.80 V at 2C effective rate. Figure 4.21 displays the discharge voltage profile of the cell as well as the specific energy referred to the sum of the two electrode composite weights, removed from the cell at different depths of discharge (DOD). The Figure shows that at 100% DOD the cell delivered a specific energy of 220 Wh $kg^{-1}$ corresponding to a specific power of 440 W $kg^{-1}$, thus indicating that these preliminary results are of notable interest for plug-in HEV applications. The total energy target suggested by U.S. Department of Energy (DOE) for minimum PHEV is 5.6 kWh, delivered at 10 kW-rate, by a battery pack of 60 kg.[111] Since it is likely that the weight of the battery pack is the double of that of the composite electrodes,[131] the graphite//LN05MO/pRGO-C65 cell providing a total energy of 6.6 kWh at 13.3 kW-rate with a 60-kg battery pack should thus be able to meet the DOE target.

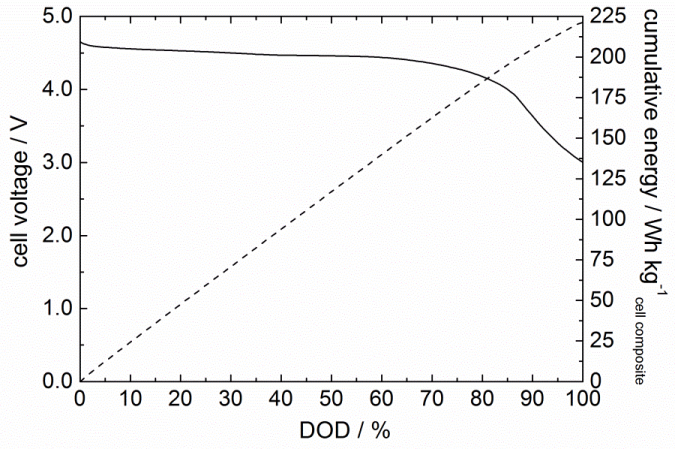


Figure 4.21. Discharge voltage profile (solid line) and cumulative specific energy (dashed line) at 2C effective rate at different DOD of the cell with graphite anode and LN05MO/pRGO-C65 cathode in LP30 at 30 °C. Reprinted from ref. [108], Copyright (2015), with permission from Elsevier.

### 4.1.8 $Li^+$ diffusion coefficient evaluation

The lithium ion diffusion occurs in response to electron transfer electron transfer process at the transition metal to maintain electroneutrality. The apparent lithium ion diffusion coefficient in solid state intercalation compounds is often calculated from peak currents ($i_p$) of linear sweep voltammetry using the Randles-Sevcik equation (Eq. 4.2):

$$i_p(\text{in ampere}) = 0.4463\ (F^3/RT)^{1/2}\ n^{3/2}\ A\ D^{1/2}\ C\ v^{1/2} \qquad (4.2)$$

which was developed for Nernstian processes with semi-infinite diffusion of electroactive species in liquid solution, and where *F* is the Faraday constant, *R* the gas constant, *T* the temperature in *K*, *n* the stoichiometric number of electrons, *A* the area in $cm^2$, *D* the diffusion coefficient in $cm^2\ s^{-1}$, *C* the bulk concentration in mol $cm^{-3}$ and *v* the scan rate in $V\ s^{-1}$.

It is noteworthy that the $i_p$ equation for intercalation/de-intercalation processes in

the solid state with finite-space diffusion is more complicated than Eq. 4.2 [132] and takes on the classical Randles-Sevcik form, in agreement with the treatment of Aoki *et al.*[133] when the ratio ($r$) between the thickness of the finite diffusion space ($\delta$) and that of the diffusion layer $((RT/nF)\,(D/v))^{1/2}$ is higher than 1 to satisfy the semi-infinite diffusion. At lower $r$ values, the Randles-Sevcik equation is no longer applicable, and the dependence of $i_p$ from $v$ gradually becomes linear, as do the voltammetric surface waves.

Cyclic voltammetry measurements at scan-rates from 10 to 150 μV $s^{-1}$, in the potential range between 4.30 and 4.78 V *vs.* $Li^+/Li$, were carried out on LN05MO/C65 and LN05MO/pRGO-C65 composite electrodes, after some conditioning galvanostatic charge/discharge cycles, to evaluate the $Li^+$ diffusion coefficient in LN05MO. Figure 4.22 displays for the LN05MO/C65 electrode the cyclic voltammetries at selected rates and shows that the peak potential related to the oxidation of $Ni^{2+}$ to $Ni^{3+}$ ($A_1$) does not change with the scan-rate: this is an indication of a Nernstian process. Moreover, the $A_1$ peak current ($i_{pA1}$) has a dependence on the scan-rate approaching 0.5, and this indicates that it is controlled by semi-infinite diffusion. Similar trends of $A_1$ peak potential and current with scan-rate were found for the LN05MO/pRGO-C65 electrode, and Figure 4.23 shows the magnification related to the $A_1$ peak of the cyclic voltammetries normalized to the mass of active material, at 80 μV $s^{-1}$ for the two composite electrodes. The higher normalized $i_{pA1}$ value for the LN05MO/pRGO-C65 electrode than for the LN05MO/C65 may be due to a greater active area of the composite electrode with pRGO, in agreement with the findings of Figure 4.11 that show a higher specific capacity at 1C for electrodes based on such a composite.

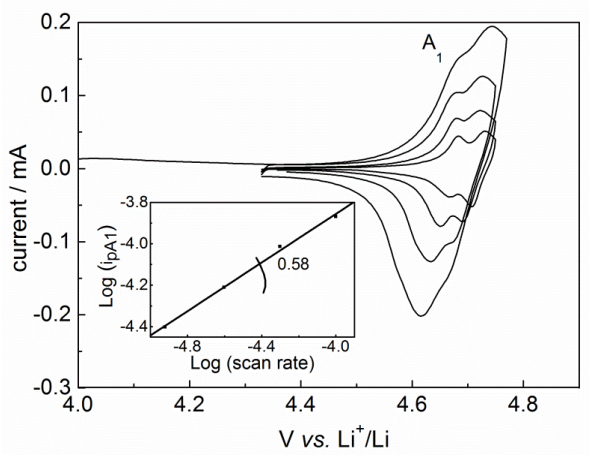


Figure 4.22. Cyclic voltammetries at scan-rates of 12, 25, 50 and 100 μV $s^{-1}$ for LN05MO/C65 (2.56 $mg_{LN05MO}$ $cm^{-2}$) composite electrode in LP30 at 30 °C. Inset reports the trend of Log $i_{pA1}$ with the Log scan rate. Reprinted from ref. [108], Copyright (2015), with permission from Elsevier.

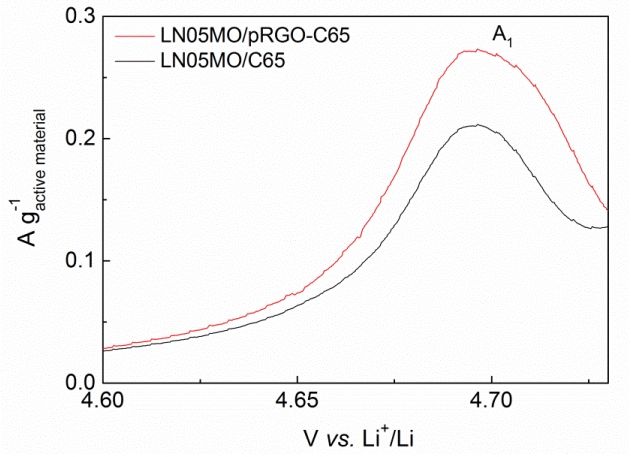


Figure 4.23. Magnification of cyclic voltammetries at 80 μV $s^{-1}$ of LN05MO/pRGO-C65 (3.77 $mg_{LN05MO}$ $cm^{-2}$) and LN05MO/C65 (2.33 $mg_{LN05MO}$ $cm^{-2}$) electrodes in LP30 at 30 °C with current normalized to the active material mass. Reprinted from ref. [108], Copyright (2015), with permission from Elsevier.

The characteristics of the cyclic voltammetries in Figure 4.22, i.e. the current peak dependence on $v^{1/2}$ and oxidation peak potential independence on $v$, make Eq. 4.2 applicable for the evaluation of the lithium ion apparent diffusion coefficient ($D_{Li+}$) in the LN05MO phase. The dependence of $i_p$ on $v^{1/2}$ is not sufficient condition for a reversible process, given that even the irreversible processes show the same dependence on scan-rate. However, the $D_{Li+}$ values reported in literature from voltammetric data of composite electrodes via Eq. 4.2 have ambiguities because of the different assumptions for the geometrical factors.[134] The use of geometric area is not correct because it underestimates the active area of the electrode and, hence, the corresponding $D_{Li+}$ values are overestimated. For instance, the $i_{pA1}$ values at different scan-rates of the LN05MO/C65 electrode of 2.56 mg $cm^{-2}$ loading (Figure 4.22), with the parameters in the Randles-Sevcik equation at the following values, $n$ = 1, $C$ = ½ $C_{LN05MO}$ = $3.5\times10^{-3}$ mol $cm^{-3}$ (calculated on the average value of the $LiNi_{0.5}Mn_{1.5}O_4$ tap density from data sheet) and $A$ = 0.636 $cm^2$ (geometric area), lead to an average $D_{Li+}$ value of $4\times10^{-10}$ $cm^2$ $s^{-1}$. This is a too high value and it is unacceptable as the $r$ value will be significantly lower than 1 with the diffusion space thickness $\delta$ = 300 nm (LN05MO grain size from NEI Corp. datasheet). On the other hand, the use of the active area calculated on the basis of the surface area of the intercalation material powder leads to overestimation of the electrode area, given that during the electrode preparation the powders may aggregate, and do so even in different ways, depending on the composite components. Given an LN05MO surface area of 2.5 $m^2$ $g^{-1}$ (from NEI Corp. data sheet) and electrode loadings as in the caption of Figure 4.23, the estimated $D_{Li+}$ value, for the LN05MO/pRGO-C65 and LN05MO/C65 electrodes, will be $2\times10^{-12}$ and $1\times10^{-13}$ $cm^2$ $s^{-1}$, respectively. Given that the $D_{Li+}$ value should be a characteristic of the intercalation material, this difference further demonstrates that the aggregation of the particles is different in the two composites, being lower for LN05MO/pRGO-C65 composite, as already noted *supra*. As more

realistic $D_{Li+}$ value at the potential of the $Ni^{2+}/Ni^{3+}$ oxidation peak can be considered that from LN05MO/pRGO-C65 composite, i.e. $D_{Li+} = 2\times10^{-12}$ $cm^2$ $s^{-1}$. This value is nearly consistent with that reported in ref. [134], where thin-film electrodes of better defined geometry obtained via pulsed laser deposition were used. Furthermore, the estimated *r* value with this $D_{Li+}$ and with a diffusion space thickness of 300 nm fully meets the condition of semi-infinite diffusion if the scan-rate is higher than 50 μV $s^{-1}$. All this clearly indicates the fragility of the diffusion coefficient data evaluated by electrochemical measurements on composite electrodes.

## 4.2 Conclusions

The study on the effect of different conducting additives, i.e. carbon blacks (C65 and SP) and reduced or partially reduced graphene oxides, demonstrated the beneficial effect of the home-made prepared partially reduced graphene oxide (pRGO) and the commercial reduced graphene oxide (RGO) on the electrochemical performance of $LiNi_{0.5}Mn_{1.5}O_4$ (LN05MO) composite electrodes in conventional LP30 electrolyte at 30 °C. The coating of LN05MO by pRGO or the addition of RGO to LN05MO in presence of carbon black positively affect the electrode/electrolyte interface, consequently improving the cycling stability of the LN05MO cathodes. It was also demonstrate the important role of the charge cut-off voltage at 4.8 V *vs.* $Li^+/Li$ and of C-rate at 1C on the cycling stability of such high-voltage composite cathodes.

The cycling performance of all the tested LN05MO composite electrodes demonstrated that the capacity loss over cycling is not due to manganese dissolution, but to the increase in thickness of the passivation surface layer, as also confirmed by the impedance spectroscopy analyses. In particular, in presence of pRGO or of RGO with C65 the total cell resistance less increases over cycling and,

then, pRGO and RGO slow down the side-reactions responsible of passivation layer formation, acting as a protective barrier that hinders its increase in thickness, while increasing the electronic conductivity of the composite electrode.

The specific energy of 220 Wh $kg^{-1}$ delivered at 1C effective rate by a graphite//LN05MO/pRGO-C65 cell, tested in LP30 at 30 °C, suggests that the pRGO-coated LN05MO composite cathode may be very interesting for lithium-ion batteries for plug-in hybrid HEV applications.

Furthermore, it was highlighted that the discrepancies regarding lithium ion diffusion coefficients in LN05MO from cyclic voltammetry data of composite electrodes are mainly due to the difficulties in evaluating the geometrical factors of these electrodes.

# Chapter 5. Water-soluble sodium carboxymethyl cellulose binder for $LiNi_{0.5}Mn_{1.5}O_4$ electrodes

Chapter 5 deals with the study on the effect of water-soluble sodium carboxymethyl cellulose (CMC), environmentally-friendly binder as alternative to PVdF, on electrochemical performance of $LiNi_{0.5}Mn_{1.5}O_4$ (LN05MO) composite electrodes in conventional EC : DMC – 1M $LiPF_6$ (LP30) electrolyte, at 20 °C and 40 °C, by using commercial $LiNi_{0.5}Mn_{1.5}O_4$ powder as active material. All the electrochemical results are compared to those with LN05MO composite electrodes featuring the most widely used PVdF.

Furthermore, the electrochemical performance of a full cell featuring graphite anode and LN05MO cathode, both electrodes with CMC binder, is also shown.

This part of the PhD work was carried out during the six-months (April 1$^{st}$, 2015 - September 30$^{th}$, 2015) of Internship as Visiting PhD Student at Helmholtz Institute Ulm (HIU) (Ulm, Germany), under the supervision of Prof. Dr. Stefano Passerini.

## 5.1 Electrochemical performance of $LiNi_{0.5}Mn_{1.5}O_4$ composite electrodes featuring water-soluble carboxymethyl cellulose binder

The formulation of all the LN05MO composite electrodes featured CMC was the same of that with PVdF binder in terms of component percentage and is reported in Table 5.1 together with the active material mass loading range. CMC-based electrodes featured carbon black Super C45 (C45) instead of Super C65 because the former is recommended for processing in aqueous solutions. The composite electrodes of 1.13 $cm^2$ geometric area were tested in LP30 in half cells *vs.* Li in excess with Whatman GF/D separator and Li reference electrode at 20 °C and 40 °C.

A graphite//LN05MO cell with the electrodes balanced in capacity was assembled and tested in LP30 at 20 °C. The composite graphite electrode (1.13 $cm^2$), based on commercial graphite, was prepared at MEET by a battery line.

Table 5.1. Formulation and active material mass loading of the LN05MO and graphite electrodes tested in half or in full cells with LP30 and Whatman GF/D separator.

| **electrode formulation / wt.%** | | **active mass loading / mg $cm^{-2}$** | |
|---|---|---|---|
| **graphite anode** | **LN05MO cathode** | **graphite** | **LN05MO** |
| 90% SLP 30<br>5% Super C45<br>5% CMC | 85% LN05MO<br>10% C45 or C65<br>5% CMC or PVdF<br>(Kynar HSV 900) | 3.0 - 4.0 | 4.0 - 10.0 |

### 5.1.1 Water-soaked $LiNi_{0.5}Mn_{1.5}O_4$ characterization

In order to investigate the effect of aqueous processing on $LiNi_{0.5}Mn_{1.5}O_4$ (LN05MO) powder, it was soaked in deionized water for 30 min under magnetic stirring at 200 rpm at room temperature and, then, filtered. After drying at 180 °C overnight, Li, Ni and Mn content was evaluated by inductively coupled plasma atomic emission spectroscopy (ICP-AES) analysis and the results are reported in Table 5.2 as well as the those of the pristine LN05MO powder for comparison. The Ni/Mn ratio remained unchanged in the water treated LN05MO powder and no Ni and Mn dissolution occurred as demonstrated by the ICP-AES analysis of the filtration water of soaked powder, which showed only a small amount of lithium presumably due to the $Li^+$–$H^+$ ion exchange taking place during the aqueous processing.[103]

Table 5.2. Results of ICP-AES analysis of pristine and water-soaked $LiNi_{0.5}Mn_{1.5}O_4$ powder.

| **ICP-AES results on $LiNi_{0.5}Mn_{1.5}0_4$ powder** | **Li** | **Ni** | **Mn** | **Ni/Mn ratio** |
|---|---|---|---|---|
| | | **%** | | |
| Pristine | 3.31 | 14.85 | 45.91 | 0.32 |
| soaked in deionized water | 3.41 | 14.85 | 46.84 | 0.32 |

The comparison of the SEM images of the water treated LN05MO and the pristine powder, displayed in Figure 5.1, shows almost the same morphology for both powders, thus indicating that the aqueous processing does not affect the surface morphology of LN05MO particles.

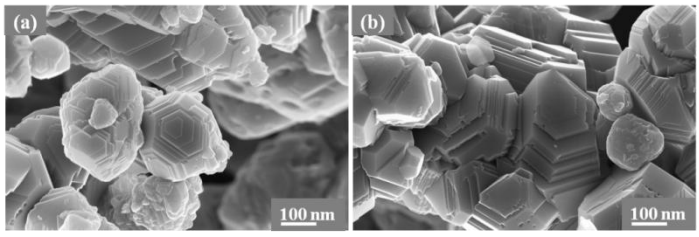


Figure 5.1. SEM images (x50000) of a) pristine and b) water treated LN05MO powder.

### 5.1.2 Electrochemical characterization of $LiNi_{0.5}Mn_{1.5}O_4$ composite electrodes with CMC or PVdF binder

The effect of water-soluble sodium carboxymethyl cellulose (CMC) binder on the electrochemical performance of the LN05MO composite electrodes was evaluated by rate capability and cycling stability tests with charge/discharge cycles between 3.5 and 4.8 V *vs.* $Li^+/Li$ in LP30 at 20 °C and 40 °C, and all the results were compared with those of electrodes having PVdF binder.

Figure 5.2 which displays the cyclic voltammetries at 20 °C of the LN05MO-CMC and of the LN05MO-PVdF electrode, both after a few conditioning cycles at C/10, highlights that the two main $A_1$ and $A_2$ peaks ($Ni^{2+} \rightarrow Ni^{3+} \rightarrow Ni^{4+}$) at high potentials and the small $A_0$ peak ($Mn^{3+} \rightarrow Mn^{4+}$) at ca. 4.0 V are fully superimposed. This confirms that the aqueous processing does not cause any modification of LN05MO structure.

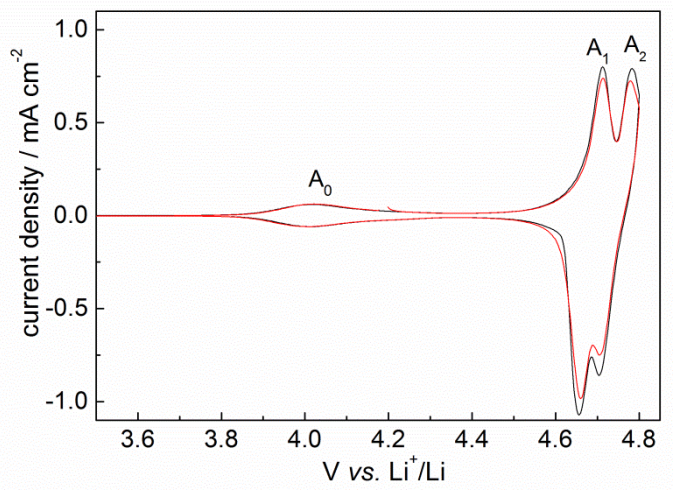


Figure 5.2. Cyclic voltammetries at 50 μV $s^{-1}$ of LN05MO-CMC (5.89 $mg_{LN05MO}cm^{-2}$) (red line) and LN05MO-PVdF (5.66 mg $cm^{-2}$) (black line) -based electrodes in LP30 at 20 °C.

The rate capability performance of the CMC-based electrode was evaluated by galvanostatic cycles with charge and discharge at different C-rates from C/2 to 10C (three cycles for each C-rate) after four conditioning cycles at C/3 and the data are displayed in Figure 5.3. The Figure also shows the capacity values of the PVdF-based electrode for a comparison. While the two electrodes deliver almost the same specific capacities at C/2 and 1C, the CMC-based electrode performs significantly better at the high C-rates in the range from 2C to 10C. The initial capacity values at C/3 highlight that the LN05MO-CMC electrode requires more conditioning cycles than the LN05MO-PVdF electrode presumably because of some $Li^+$ ions were exchanged by $H^+$ ions during the aqueous slurry processing, as reported in ref. [103].

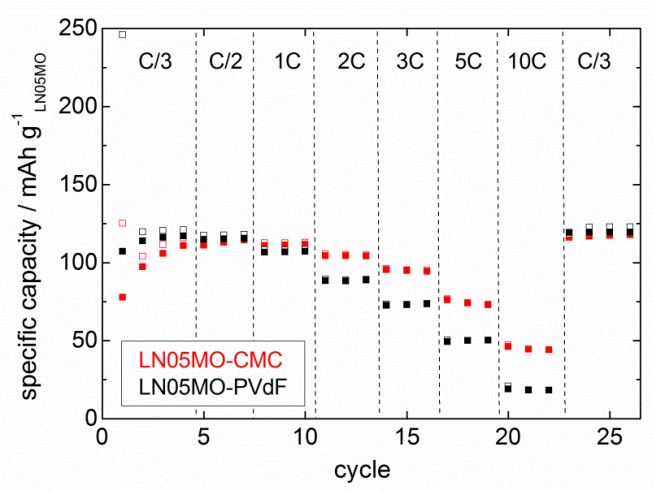


Figure 5.3. Charge (void symbol) and discharge (full symbol) specific capacities of LN05MO-CMC (5.34 $mg_{LN05MO}$ $cm^{-2}$) and LN05MO-PVdF (5.25 $mg_{LN05MO}$ $cm^{-2}$) electrodes upon rate capability test at different C-rates in LP30 at 20 °C.

The strongest difference in terms of electrochemical performance between the LN05MO-CMC and LN05MO-PVdF electrodes was evident mainly upon long-term cycling test performed on the same electrodes after the rate capability test and

shown in Figure 5.4. The two electrodes performed twenty galvanostatic cycles at C/3 and 400 cycles at 1C, with 5 cycles at C/3 each 100 cycles at 1C to evaluate the capacity retention of the electrodes. The superior cycling stability of the CMC-based electrode is clearly visible by the lower capacity loss over the cycles at 1C, i.e. 17% (0.04% per cycle) against 38% (0.1% per cycle) of the PVdF-based electrode, as well as by the higher capacity retention (the ratio between the discharge capacity of the last C/3 cycle and that of the 27$^{th}$ one), namely 90% with respect to 88% displayed by the LN05MO-PVdF electrode.

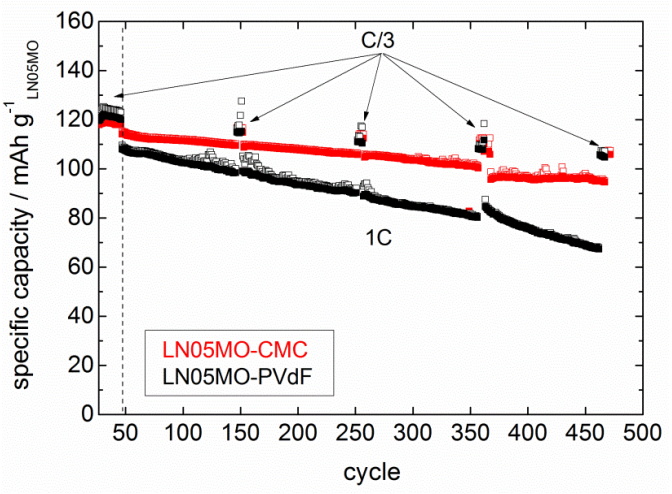


Figure 5.4. Charge (void symbol) and discharge (full symbol) specific capacities of LN05MO-CMC (5.34 $mg_{LN05MO}$ $cm^{-2}$) and LN05MO-PVdF (5.25 $mg_{LN05MO}$ $cm^{-2}$) electrodes upon cycling stability test at C/3 (20 cycles) and 1C (400 cycles with 5 cycles at C/3 each 100 cycles at 1C) in LP30 at 20 °C. Both electrodes performed the rate capability test shown in Figure 5.3.

The charge/discharge voltage profiles of the 1$^{st}$ and 400$^{th}$ cycle at 1C of the two electrodes displayed in Figure 5.5 clearly show that the highest capacity loss of the LN05MO-PVdF electrode upon cycling is not due to the metal dissolution because the characteristic plateau of $Mn^{4+}$ reduction to $Mn^{3+}$ at around 4.0 V is still present in the discharge voltage profile of the 400$^{th}$ cycle. It is evident that the ohmic drop of the LN05MO-CMC electrode increased over cycling less than that of the

LN05MO-PVdF, thus resulting in a more cycling stability.

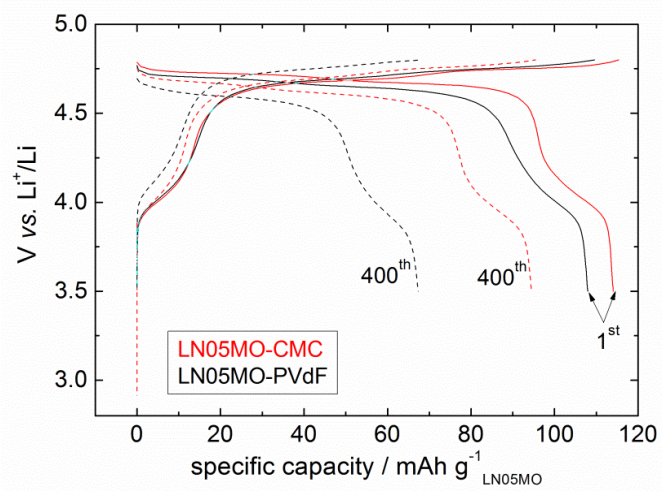


Figure 5.5. Charge and discharge voltage profiles of the 1st (solid line) and 400$^{th}$ cycle at 1C (dashed line) of the LN05MO-CMC (5.34 $mg_{LN05MO}$ $cm^{-2}$) and LN05MO-PVdF (5.25 $mg_{LN05MO}$ $cm^{-2}$) electrodes upon cycling stability test in LP30 at 20 °C.

To explain the better performance of the CMC-based electrode with respect to that with PVdF, *ex-situ* SEM measurements of the cycled LN05MO-CMC and LN05MO-PVdF electrodes were carried out and the images are reported in Figures 5.6a-d. The Figure highlights the different morphology of CMC-based electrode compared to the PVdF-based one. The SEM images of the pristine and pressed LN05MO-CMC (5.6a) and LN05MO-PVdF (5.6c) electrodes show that the electrode containing CMC binder displays a more homogeneous surface, where the LN05MO particles are better dispersed within the carbon matrix than the electrode with PVdF which, in turn, displays some aggregates on the surface. Figures 5.6b and 5.6d show the SEM images of cycled LN05MO-CMC and LN05MO-PVdF electrodes, respectively, and it is evident that the nature of the binder strongly influences the morphological structure of the LN05MO composite electrodes. Unlike the CMC-based electrode which still displays a compact, homogeneous and

nearly unchanged surface after 400 cycles at 1C, the PVdF-based electrode appears fully covered by a surface layer that hinders the detection of the particles of LN05MO and carbon black.

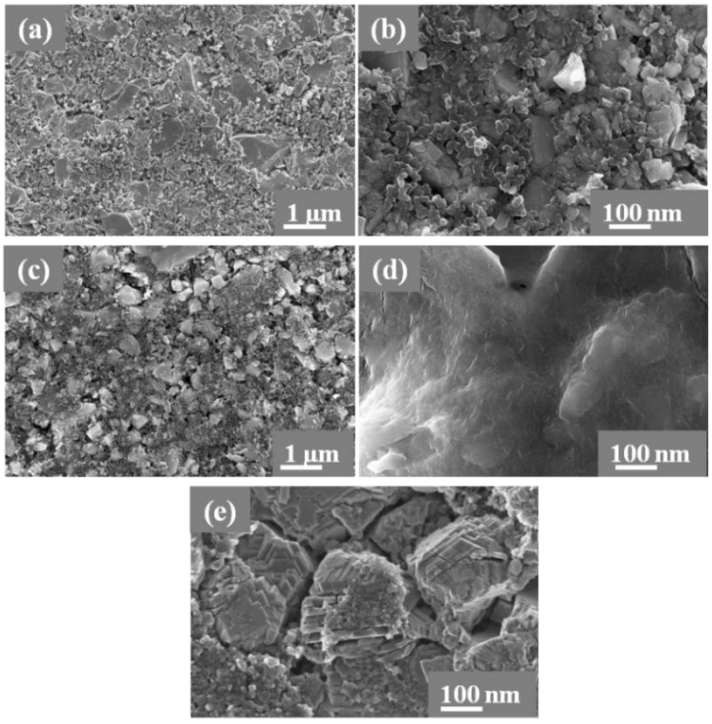


Figure 5.6. SEM images of the LN05MO-CMC electrodes (a) pristine (x20000) and (b) after 400 cycles at 1C (x50000) as in Figure 5.4; of the LN05MO-PVdF electrodes (c) pristine (x20000) and (d) after 400 cycles (x50000) as in Figure 5.4; of LN05MO-PVdF electrode (5.18 mg $cm^{-2}$) (e) after 100 cycles at 1C.

The formation of such a thick passivation layer, which is detrimental for the cycling performance of the electrode as demonstrated by the results shown in Figure 5.4, is due to the electrolyte decomposition on the cathode surface at high operating potentials. Owing to the strong affinity of PVdF with the organic solvents, it can easily swell when it is in contact with the carbonate-based electrolyte solution leading to the penetration of the electrolyte into the whole

composite electrode.[135] The percolating conducting network between carbon black and active particles may be thus partly lost as well as the integrity of the electrode, resulting in cracked and inhomogeneous electrode surface, as evinced by the SEM image of another cycled LN05MO-PVdF electrode after 100 cycles at 1C reported in Figure 5.6e. Indeed, PVdF can also suffer from dehydrofluorination, i.e. the formation of C=C bonds and elimination of HF,[136] leading to integrity loss of the surface electrode. Therefore, the surface of PVdF-based electrode is much more exposed than the CMC-based ones to the to the side-reactions that take place at high-operating voltages causing the formation of thick passivation layer which leads to high capacity fading over long-term cycling. On the other hand, the superior performance of the CMC-based electrodes can be explained taking into consideration the strong binding affinity between CMC binder and LN05MO particles with formation of ester bonds between the carboxylic groups of CMC and the hydroxyl groups on the surface of the active material particles,[137] thus leading to a highly homogeneous distribution of CMC within the LN05MO composite electrodes. As CMC is more efficient in bridging the active particles, the dispersion of carbon black in the aqueous slurry is more effective than in the NMP organic solvent for the PVdF-based slurry.[101] Therefore, the homogenous three-dimensional network that CMC promotes between the conductive additive and active material particles leads to a tight and more homogeneous electrode architecture than with PVdF binder and this is expected to be beneficial for the cycling stability of the electrode, especially when high-voltage cathode materials are involved.

All these findings are supported by the impedance spectroscopy measurements that aimed to investigate the electrode/electrolyte interface of the LN05MO composite electrodes with CMC or PVdF binders during the cell operation. The IS spectra of LN05MO-CMC and LN05MO-PVdF electrodes in the charged state at 4.8 V *vs.* $Li^+$/Li were collected at the end of the rate capability test ($27^{th}$ cycle) and

upon the cycling stability test at 1C, i.e. after the 362$^{th}$ and the last (677$^{th}$) cycles. Figure 5.7 shows the related spectra that were analyzed with the equivalent circuit $R(R_{sl}Q_{sl})(R_{ct}Q_{ct})Q_W$ as for the spectra of Figure 4.12 in Subsection 4.1.5. The Figure clearly shows the much lower resistance increase of the LN05MO-CMC electrode compared to that of LN05MO-PVdF over cycling. While the resistance $R_{sl}$ and $R_{ct}$ values (Table 5.3) of the CMC-based electrode slowly increased over cycling, those of the PVdF-based electrode increased more sharply, thus indicating that the passivation layer on the LN05MO-PVdF surface was growing and that the kinetics of the $Li^+$ insertion processes slowed as confirmed by the increasing of $R_{ct}$ values.

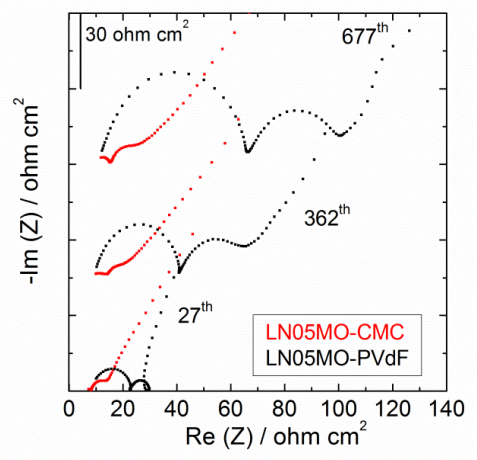


Figure 5.7. Impedance spectra (100 kHz - 10 mHz) of the LN05MO-CMC (5.61 $mg_{LN05MO}$ $cm^{-2}$) (red square) and LN05MO-PVdF (4.69 $mg_{LN05MO}$ $cm^{-2}$) (black square) in the charged state at 4.8 V *vs.* $Li^+$/Li at different number of cycles.

Table 5.3. $R_{sl}$ and $R_{ct}$ (in ohm $cm^2$) from the impedance spectra of the charged (4.8 V vs. $Li^+$/Li) LN05MO-CMC and LN05MO-PVdF electrodes of Figure 5.7.

| **cycle** | **LN05MO-CMC** | | **LN05MO-PVdF** | |
|---|---|---|---|---|
| | **$R_{sl}$** | **$R_{ct}$** | **$R_{sl}$** | **$R_{ct}$** |
| 27 | 1.2 | 4.2 | 5.9 | 14.4 |
| 362 | 4.0 | 6.9 | 18.3 | 29.8 |
| 377 | 5.9 | 7.8 | 27.4 | 55.9 |

These results of impedance spectroscopy measurements demonstrated that in presence of CMC binder the side-reactions between the electrode/electrolyte interface are slowed down thanks to the homogenous three-dimensional network that CMC promotes between the carbon black and LN05MO particles. This enhances the electrical contact between the particles, thus decreasing the electrode polarization and the charge-transfer resistance [107] and remarkably improving the LN05MO's cycling stability. Presumably, the CMC may act also as a protective layer, thus reducing the surface of LN05MO active particles in direct contact with the electrolyte and stabilizing the electrode/electrolyte interface.

In order to investigate the chemistry of the surface passivation layer, *ex-situ* XPS analysis were carried out on the pristine and cycled LN05MO-CMC and LN05MO-PVdF electrodes at the end of the electrochemical tests. All the samples, which were in discharged state, were transferred into XPS apparatus through a sample holder that prevented any contact with air. Although all the cycled electrodes contained C, O and F (survey spectra not reported here), the spectra of Li 1s, Mn 3p and Mn 2p were taken as diagnostic spectra for the comparison of the cycling behaviors the LN05MO composite electrodes with the two different binders. These spectra are shown in Figure 5.8a-d, in particular the pristine LN05MO-CMC and LN05MO-PVdF electrodes in 5.8a-b and the cycled in 5.8c-d. For both pristine electrodes the Figure 5.8a shows the signal of Mn 3p, which consists of a main peak at ca. 50 eV assigned to the $Mn^{4+}$ ions and of a shoulder at ca. 48.4 eV assigned to the $Mn^{3+}$ ions.[117] As shown in Figure 5.8b, the signal of Mn 2p for both electrodes is split in two parts because of spin-orbit coupling: the Mn $2p_{1/2}$ peak at ca. 653.5 eV and the Mn $2p_{3/2}$ peak at 641.7 eV.[138,139] Figures 5.8c and 5.8d clearly highlight the great differences between the cycled LN05MO-CMC and LN05MO-PVdF electrodes. While the Mn 3p and Mn 2p spectra remained almost unchanged even after 400 cycles at 1C in the cycled LN05MO-CMC electrode, except the peak intensities that are lower than for the pristine electrode, no manganese peaks appear

for the cycled LN05MO-PVdF electrode. Moreover, the Li 1s peak, which was not detected in both pristine electrodes, is present at ca. 55.2 eV only in the cycled PVdF-based electrode. It was attributed to LiF and $Li_2CO_3$ [117,140,141] that might arise from the degradation of $LiPF_6$ and from the electrolyte decomposition upon cycling. These findings suggest the formation of a thick passivation layer on the surface of the LN05MO-PVdF electrode and, hence, the side-reactions at the electrode/electrolyte interface were more facilitated in PVdF-based electrode than in that with CMC binder. These XPS results are in good agreement with the SEM findings and impedance spectroscopy measurements, confirming the presence of a thick passivation layer on LN05MO-PVdF electrode surface which is responsible of the high cell resistance increase and, hence, of the sharp capacity fading upon cycling.

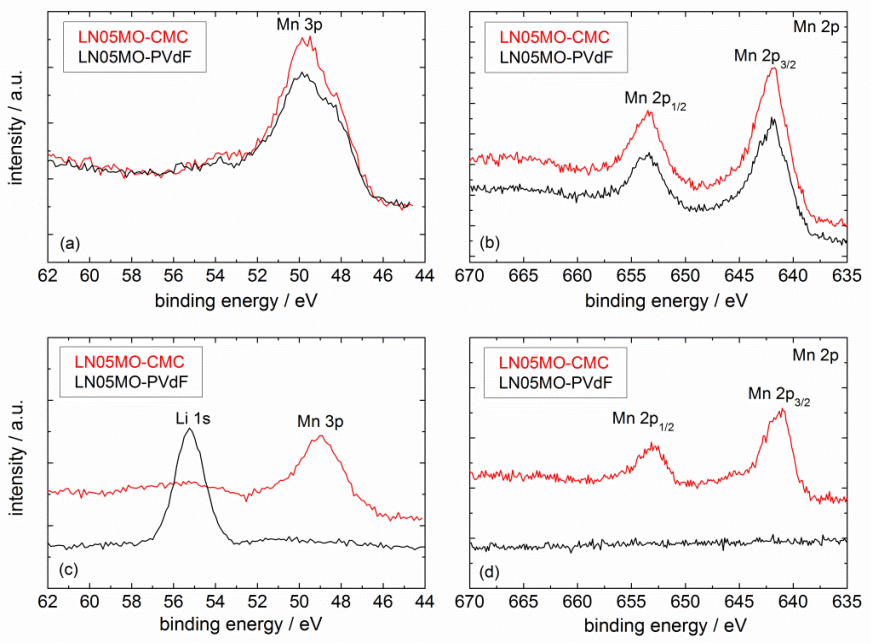


Figure 5.8. Li 1s, Mn 3p and Mn 2p core peaks of the (a, b) pristine and (c, d) cycled LN05MO-CMC (5.34 $mg_{LN05MO}$ $cm^{-2}$) (red line) and LN05MO-PVdF (5.25 $mg_{LN05MO}$ $cm^{-2}$) (black line) electrodes in discharged state.

The cycling stability of the LN05MO-CMC electrode was also evaluated upon one thousand galvanostatic cycles at 1 C between 3.50 and 4.80 V *vs.* $Li^+/Li$ in LP30 at 20 °C V, with 5 cycles at C/3 every 100 cycles. Furthermore, at the end of the 1000 cycles at 1C with charges up to 4.80 V, 20 cycles at C/3 followed by 300 cycles at 1C with charges up to 4.85 V and the discharge specific capacity values over cycling with the two charge-cut-off potentials are in Figure 5.9. The composite electrode displayed a capacity loss of 36% (0.04% per cycle) at the end of 1000 cycles at 1C and a capacity retention of 88.4% at C/3. It is worthy that the LN05MO-PVdF electrode displayed the same capacity loss only after 400 cycles at 1C (see Figure 5.4).

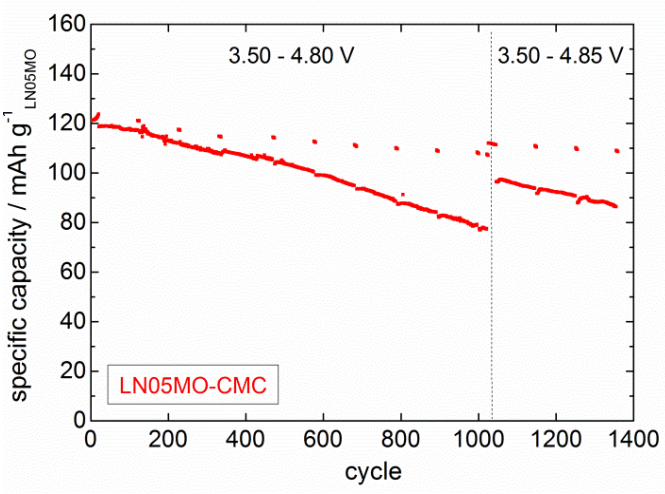


Figure 5.9. Discharge specific capacity of LN05MO-CMC electrodes (5.84 $mg_{LN05MO}$ $cm^{-2}$) upon cycling stability test between 3.50 and 4.80 V *vs.* $Li^+/Li$ at C/3 (20 cycles) and 1C (1000 cycles with 5 cycles at C/3 each 100 cycles at 1C) and up to 4.85 V *vs.* $Li^+/Li$ at C/3 (20 cycles) and 1C (300 cycles with 5 cycles at C/3 each 100 cycles) in LP30 at 20 °C.

Moving to 4.85 V charge-cut-off potential, the capacity of LN05MO-CMC electrode improved as clearly shown by Figure 5.9. The electrode after 300 cycles at 1C up to 4.85 V displayed a capacity loss of 11% (0.04% per cycle) and a

capacity retention of 97% at the end of cycling at C/3 up to 4.85 V. These findings demonstrated that the LN05MO-CMC electrode responds very well to the cycling test even in strong conditions and confirms that the CMC binder may mitigate the side-reactions between LN05MO and LP30, thus stabilizing the electrode/electrolyte interface and improving the LN05MO's cycling performance.

The beneficial effect of the CMC binder was also investigated on the electrochemical performance of the LN05MO composite electrodes at 40 °C where the electrolyte decomposition is more crucial. Figure 5.10a shows the data of the rate capability and Figure 5.10b those of the cycling stability test carried out on the LN05MO-CMC and LN05MO-PVdF electrodes between 3.5 and 4.8 V *vs.* $Li^+/Li$ in LP30. Figure 5.10 highlights that, even at 40 °C, the LN05MO-CMC electrode performs upon the whole cycling sequence, displaying a capacity loss of 8% against 38% for PVdF-based electrode over 100 cycles at 1C and a capacity retention of 91% against of 78%, respectively, at the end of the cycling stability test. While the capacity loss of the LN05MO-CMC over 100 cycles at 1C at 40 °C is the double of that displayed at 20 °C (i.e. 4%), the LN05MO-PVdF displayed a capacity loss more than four-fold higher than that displayed at 20 °C (9%).

Since it is reasonable that the higher is the temperature more accelerated are the unwanted reactions responsible of the formation of the passivation layer on the cathode surface, the impact of the binder on long-term cyclability of the LN05MO composite electrode is more evident when high operating temperatures are involved. Therefore, the results obtained at 40 °C confirm the beneficial effect of the CMC binder on LN05MO's stability. It is reasonable that in presence of the CMC the oxidative electrolyte decomposition is slowed down, thus positively affecting the electrochemical performance also at high temperatures.

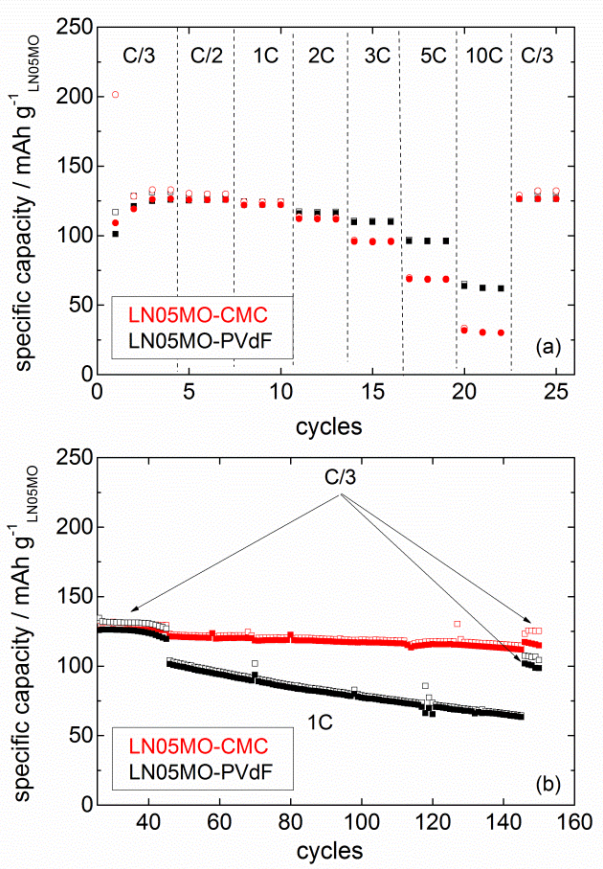


Figure 5.10. Charge (void symbol) and discharge (full symbol) capacities over (a) rate capability at different C-rates and (b) cycling stability at C/3 (20 cycles) and 1C (100 cycles with 5 cycles after 100cycles at 1C) of LN05MO-CMC (5.75 $mg_{LN05MO}$ $cm^{-2}$) (red square) and LN05MO-PVdF (5.61 $mg_{LN05MO}$ $cm^{-2}$) (black square) electrodes between 3.5 and 4.8 V *vs.* $Li^+/Li$ in LP30 at 40 °C.

### 5.1.3 Graphite//$LiNi_{0.5}Mn_{1.5}O_4$ cell featuring both electrodes with CMC binder

A graphite//LN05MO cell featuring the two electrodes with CMC binder was assembled and tested at 20 °C in LP30. Given that the graphite electrode showed irreversible capacity (i.e. 18%) at the first cycle for the formation of SEI and that both electrodes require some conditioning cycles to stabilize the capacity, both

electrodes were pre-cycled in half cell *vs.* Li. The pre-cycling consisted of six cycles in LP30 at 20 °C with constant current (CC) charge at C/10 up to 4.80 V for LN05MO and down to 0.02 V for graphite followed by a constant voltage (CV) step for 30 min and discharge down to 3.5 V for LN05MO and up to 1.5 V for graphite. At the sixth cycle at C/10 the graphite provided a capacity of 367 mAh $g^{-1}$ (i.e. 1.21 mAh $cm^{-2}$) and the LN05MO electrode provided a capacity of 124 mAh $g^{-1}$ (i.e. 1.16 mAh $cm^{-2}$). Then, the graphite//LN05MO cell was assembled and Figure 5.11a shows the specific charge and discharge capacity upon cycling with CC charges at C/10 (0.138 mA $cm^{-2}$) and C/3 (0.460 mA $cm^{-2}$) and at 2C effective rate (1.33 mA $cm^{-2}$) up to 4.8 V, followed by CV step for 30 min and discharge at C/10 and C/3 and 2C effective rate down to 3.5 V. In view of the use of both graphite and LN05MO electrodes based on CMC binder in lithium-ion batteries for plug-in HEV applications, the specific energy referred to the sum of the two composite weights (i.e. 4.12 mg for graphite and 12.51 mg for LN05MO) removed from the cell during the $43^{th}$ cycle at 2C effective rate was evaluated at different depths of discharge (DOD). Figure 5.11b, which displays the discharge voltage profile of the cell as well as the specific energy at different DOD, shows that the cell delivered a specific energy of 164 Wh $kg^{-1}$ at 100% DOD corresponding to a specific power of 382 W $kg^{-1}$. According to the U.S. Department of Energy (DOE), the total energy target suggested for minimum plug-in HEV is 5.6 kWh, delivered at 10 kW-rate, by a battery pack of 60 kg.[111] Taking into account that the weight of the battery pack can be considered the double of the composite weights,[131] the graphite//LN05MO cell at the level of 60-kg battery pack is able to yield a total energy of 5.5 kWh at 12.8 kW-rate which is near to the DOE total energy target. These preliminary results suggested that the combination of a graphite anode with $LiNi_{0.5}Mn_{1.5}O_4$ cathode featuring water-soluble binder is very promising for the development of a high-voltage lithium-ion batteries operating in conventional electrolyte.

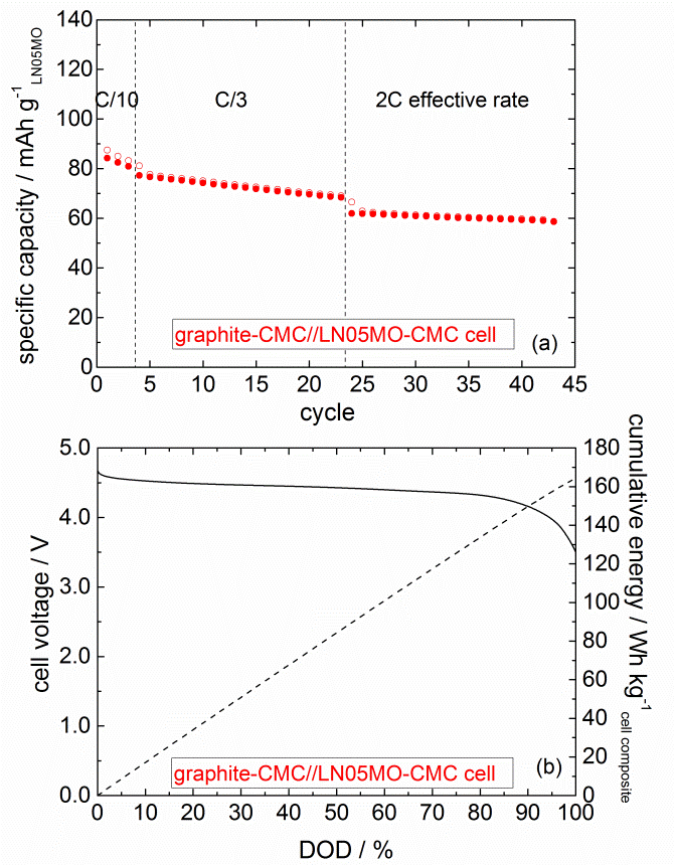


Figure 5.11. (a) Charge (void symbol) and discharge (full symbol) specific capacity upon CC-charges up to 4.8 V, CV-step for 30 min and discharge of the cell with graphite anode (3.28 $mg_{graphite}$ $cm^{-2}$) and LN05MO cathode (9.41 $mg_{LN05MO}$ $cm^{-2}$) and (b) discharge voltage profile (solid line) and cumulative specific energy (dashed line) at 2C effective rate at different DOD of the cell in LP30 at 20 °C.

## 5.2 Conclusions

The study on the effect of water-soluble carboxy methylcellulose (CMC) as alternative binder for high-voltage $LiNi_{0.5}Mn_{1.5}O_4$ (LN05MO) cathode instead of commercially used PVdF binder highlighted that the nature of the binder has a strong influence on the electrochemical performance of LN05MO composite

electrodes, especially upon long-term cyclability. The LN05MO-CMC electrodes outperform those with PVdF in terms of capacity retention upon long-term cycling test carried out with deep charge/discharge cycles in conventional LP30 electrolyte at 20 °C and 40 °C. The CMC is more effective than PVdF in bridging the particles: it promotes an homogeneous three-dimensional percolating network between the conductive carbon and LN05MO particles which results in a more homogeneous electrode surface with respect to the electrode with PVdF binder. This makes it possible to limit the direct contact of the LN05MO surface with the electrolyte, thus reducing the oxidative electrolyte decomposition at high-operating voltages. Therefore, in LN05MO-CMC electrodes the side-reactions responsible of the formation of a passivation layer on LN05MO cathode surface are slowed down as clearly evinced by the impedance spectroscopy measurements. The CMC-based electrodes, indeed, displayed a slower resistance increase over cycling with respect to the LN05MO-PVdF electrodes where the high resistance increase is due to the formation of a thick surface layer responsible of the sharp capacity fading upon cycling. These findings are also supported by the *ex-situ* SEM and XPS analyses carried out on the pristine and cycled CMC- and PVdF-based electrodes at the end of cycling stability tests. The LN05MO-CMC electrodes performed better than those with PVdF even at 40 °C where the oxidative electrolyte decomposition is more crucial. CMC can effectively mitigate the side-reactions between LN05MO particles and the electrolyte promoting a more stable electrode/electrolyte interface, notably improving the cycling performance of the LN05MO cathode.

Furthermore, a graphite//LN05MO cell featuring both electrodes with CMC binder was assembled and the preliminary results suggest that the use of CMC is a very promising, sustainable approach for the development of high-voltage lithium-ion batteries for plug-in HEVs operating in conventional electrolyte.

# Chapter 6. Characterization tests for power-assist and plug-in hybrid electric vehicle applications

Chapter 6 deals with the results of characterization tests according to the U.S. Department of Energy (DOE) Battery Test Manual for power-assist hybrid electric vehicles (HEVs) and plug-in HEVs (PHEVs) carried out on laboratory high-voltage cells featuring graphite anode and $LiNi_{0.4}Mn_{1.6}O_4$ (LNMO) or $LiNi_{0.5}Mn_{1.5}O_4$ (LN05MO) cathodes, in view of the use of such cathode materials in lithium-ion batteries for automotive applications. The first part of the Chapter reports the tests for power-assist HEVs, the second part deals with the tests for PHEVs, even with pre-industrial, high-mass loading electrodes suitable for the scale-up of batteries for automotive applications.

The tests were performed at 20 °C and 30 °C in EC : DMC – 1M $LiPF_6$ (LP30) and EC : DMC – 1M LiFAP (LF30) with and without SEI-forming additives, i.e. succinic anhydride (SA, 2 wt.%) to protect the cathode and 1-fluoro ethylene carbonate ($F_1EC$, 1.6 wt.%) for the graphite anode, using different separators: commercial monolayer polypropylene separator (Celgard®2400), macroporous polyvinylidene fluoride (PVdF) membrane reinforced with nanocrystalline cellulose (NCC) and glass fibre Whatman GF/D separator.

Elsevier is acknowledged for the permission to reprint some parts of the following publications:

- C. Arbizzani, F. Colò, F. De Giorgio, M. Guidotti, M. Mastragostino, F. Alloin, M. Bolloli, Y. Molméret, J.-Y. Sanchez, A non-conventional fluorinated separator in high-voltage graphite/$LiNi_{0.4}Mn_{1.6}O_4$ cells, J. Power Sources 246 (2014), 299-304. Copyright (2014).
- C. Arbizzani, F. De Giorgio, M. Mastragostino, Characterization tests for plug-in hybrid electric vehicle application of graphite/$LiNi_{0.4}Mn_{1.6}O_4$ cells with two different separators and electrolytes, J. Power Sources 266 (2014), 170-174. Copyright (2014).

## 6.1 DOE battery tests for power-assist and plug-in HEV applications on lab-scale cells

The testing procedures developed by U.S. Advanced Battery Consortium (USABC) LLC. and DOE can also be performed on small size laboratory cells of a few mAh or less that are generally tested in research laboratories. Provided that electrode formulations and loadings are suitable for scale-up, the obtained results will yield more confident data to forecast performance of large battery packs in HEVs than those from cycling with conventional deep charge/discharge cycles. Given that the laboratory cells feature low geometric area, the battery size factor, namely the minimum number of cells or modules required for a battery pack to meet all the DOE targets, would be very high, it is preferred to compare specific laboratory cell data with the specific energy and power values obtained by dividing the energy and power targets by the battery pack weights [118] reported in Tables 2.2 and 2.3 (Chapter 2). According to Stewart *et al.*,[131] the total lab cell weight is estimated as twice the composite weight of both electrodes in order to take into account the contribution of all the cell components. Therefore, hereinafter the specific parameters (energy and power) for all the tested cells are referred to the so-called battery weight calculated as the double of the composite weights of graphite anode and LNMO or LN05MO cathode.

The characterization test for HEVs application involve the static capacity (SC) test at constant discharge current to evaluate the capacity and the energy of the battery system and the hybrid pulse power characterization (HPPC) tests with 10s discharge and regenerative pulses to estimate the dynamic power capability of the battery system. The discharge rate of SC test for power-assist HEV was set at 1C and at constant discharge power of 10 kW referred to the full-size battery pack for plug-in HEVs. The HPPC tests incorporated 10 s discharge pulse at low (5C) and high (10C) currents, 40 s equilibration time (rest time) and 10 s regenerative pulse

at a current which is 75% of the discharge pulse currents. This sequence has to be carried out at different depth-of-discharge (DOD) from 10% to 90%, separated by 10% DOD segments at the same discharge-rate of the SC test and 1h equilibration time (rest time). HPPC tests can end before 90% DOD if the cell voltage exceeds the selected $V_{max}$ value in regenerative pulse and $V_{min}$ = 0.55 $V_{max}$ in discharge pulses.

As previously mentioned in Chapter 1, the energy requirements of the battery system are strictly depending on the level of power-train hybridization and on the unassisted electric driving range. While in power-assist HEVs the battery system operates in charge-sustaining (CS) mode where the battery is used during acceleration and braking for a brief time and is kept in an almost constant state-of-charge (SOC) by the internal combustion engine, in PHEVs the battery can also operate in charge-depleting (CD) mode where the battery can be fully discharged during electric propulsion of the vehicle, enabling an electric-driving range greater than in power-assist HEVs. Therefore, the energy demand for PHEVs is significantly higher than for power-assist HEVs and the power-to-energy ratio targets set by DOE are 13 for minimum PHEV and 83 for minimum power-assist HEV with energy goals of 93.3 Wh $kg^{-1}$ [111] and 7.5 Wh $kg^{-1}$,[110] respectively. The goals set by DOE are referred to three different PHEV types: sport utility vehicles (SUV) with a mass of 2000 kg and an electric range of 10 miles (minimum PHEV), cars of 1600 kg and electric range of 20 miles (medium PHEV), and cars of 1500 kg with electric range of 40 miles (maximum PHEV).

## 6.2 High-voltage graphite//$LiNi_{0.4}Mn_{1.6}O_4$ cells for power-assist HEV application

The FreedomCAR test for power-assist HEV were performed on graphite//LNMO cells by using LNMO cathode and graphite anode provided in the frame of AMELIE Project. LNMO composite electrodes based on LNMO active material synthesized by CEA-LITEN (Grenoble, FR) were prepared by MEET MEET (Münster, DE) and the graphite composite electrodes based on commercial graphite were prepared by Kiev National University of Technologies and Design. The cells with electrodes of 0.636 $cm^2$ geometric area were tested in LF30 with $F_1$EC and SA additives at 30 °C and the cell characteristics are shown in Table 6.1.

Table 6.1. Characteristics of graphite//LNMO cells tested according to the FreedomCAR protocol for power-assist HEV application in LF30 1.6 wt.% $F_1$EC-2 wt.% SA at 30 °C.

| **electrode formulation / wt.%** | | **active mass loading / mg $cm^{-2}$** | | **separator** |
|---|---|---|---|---|
| **graphite anode** | **LNMO cathode** | **graphite** | **LNMO** | |
| 89% SLA-1025<br>3% PureBLACK™<br>8% PVdF<br>(Solef®5130) | 85% LNMO<br>10% Super C65<br>5% PVdF<br>(Solef®5130) | 2.5 ÷ 3.1 | 6.5 ÷ 8.0 | PVdF-NCC<br>Celgard®2400 |

The results of the SC tests on graphite//LNMO cells with PVdF-NCC and Celgard®2400 separators, shown in Figure 6.1, were carried out at 1C effective discharge-rate, after charge up to 4.75 V, at different depth-of-discharge (DOD). In particular, Figure 6.1a shows that the cell with PVdF-NCC membrane displayed a cumulative energy ($E_{SCT}$) of 101 Wh $kg^{-1}$, higher than that removed from the cell with Celgard, i.e. 85 Wh $kg^{-1}$ (Figure 6.1b), as expected after the discharge and charge capability results reported in Chapter 3 (Figure 3.15).

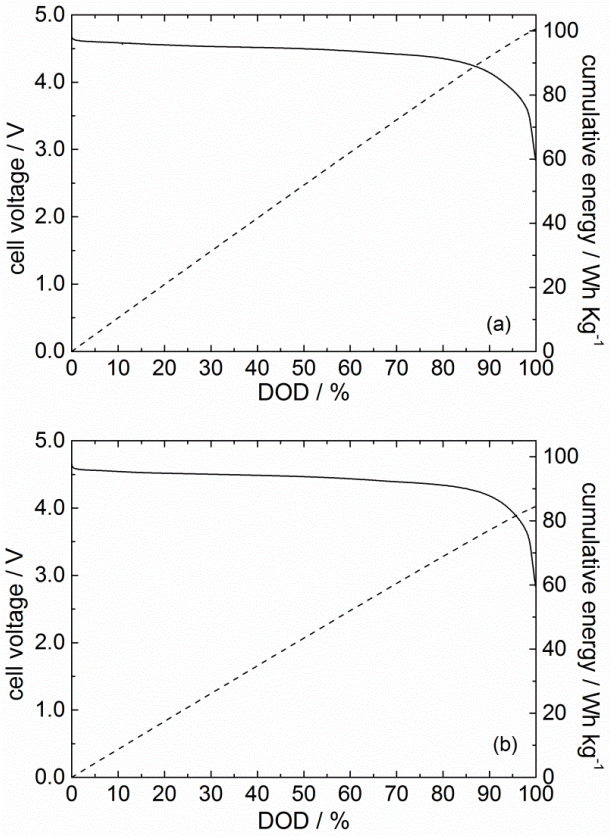


Figure 6.1. Discharge voltage profile (solid line) and specific energy (dashed line) delivered at 1C effective rate *vs.* DOD of the cells with (a) PVdF-NCC and (b) Celgard®2400 separators in LF30-$F_1$EC-SA at 30 °C. Reprinted from ref. [109], Copyright (2014), with permission from Elsevier.

After the SC test, the PVdF-NCC and Celgard cells performed the HPPC tests at low (5C) and high (10C) currents. Figure 6.2 shows the voltage profile of the cell with PVdF-NCC membrane upon the HPPC test with discharge pulses at 5C (2.25 mA $cm^{-2}$) from 10% to 90% DOD with the selected $V_{max}$ value of 5.1 V in regenerative pulse and $V_{min}$ = 0.55 $V_{max}$ in discharge pulse at 30 °C. The inset in the Figure displays the magnification of the pulses at 10% DOD to mark the cell voltage values just before the discharge and regenerative pulses, $V_0$ and $V_2$, and those at the end of these pulses, $V_1$ and $V_3$.

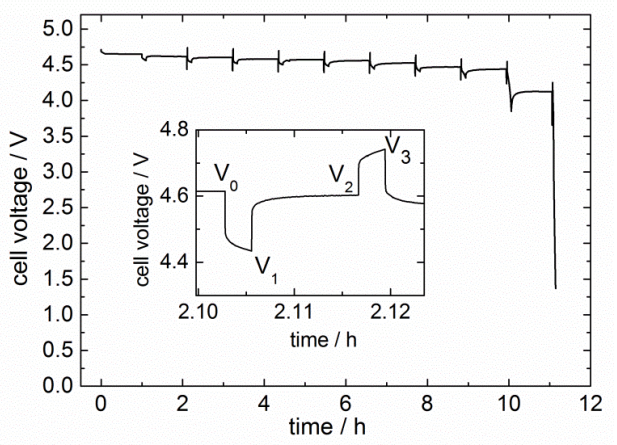


Figure 6.2. Cell voltage profile over HPPC at 5C of the cell with PVdF-NCC separator. In the inset, the magnification of the discharge and regenerative pulses at 10% DOD. Reprinted from ref. [109], Copyright (2014), with permission from Elsevier.

These voltage values were used to calculate at each % DOD the discharge and regenerative pulse resistances, $R_{dis}$ and $R_{reg}$, by Eqs.6.1 and 6.2:

$$R_{dis} = \frac{V_1 - V_0}{I_{dis}} \qquad (6.1) \qquad R_{reg} = \frac{V_3 - V_2}{I_{reg}} \qquad (6.2)$$

and, then, the discharge and regenerative pulse power, $P_{dis}$ and $P_{reg}$, by Eqs. 6.3 and 6.4:

$$P_{dis} = V_{min}\frac{V_0 - V_{min}}{R_{dis}} \qquad (6.3) \qquad P_{reg} = V_{max}\frac{V_{max} - V_2}{R_{reg}} \qquad (6.4)$$

The $R_{dis}$ and $R_{reg}$ values calculated by the data of the HPPC test performed at 5C and 10C currents are shown in Figure 6.3. While the 5C current test ended at 90% DOD, that at 10C ended at 60% DOD.

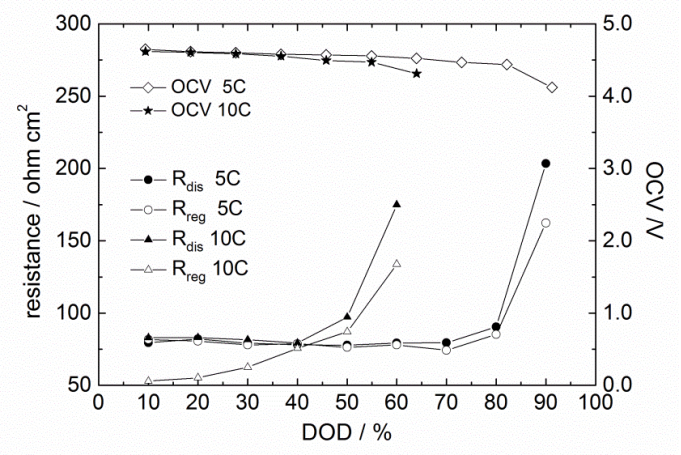


Figure 6.3. Cell with PVdF-NCC separator: (a) open circuit voltage (OCV) and resistance from discharge (full symbol) and regenerative (void symbol) pulses *vs*. DOD% from HPPC tests at 5C and 10C (the last ends at 60% DOD). Reprinted from ref. [109], Copyright (2014), with permission from Elsevier.

Figure 6.4 displays the specific power values (discharge and regenerative) by the 5C current tests *vs*. % DOD of the cell with PVdF-NCC separator.

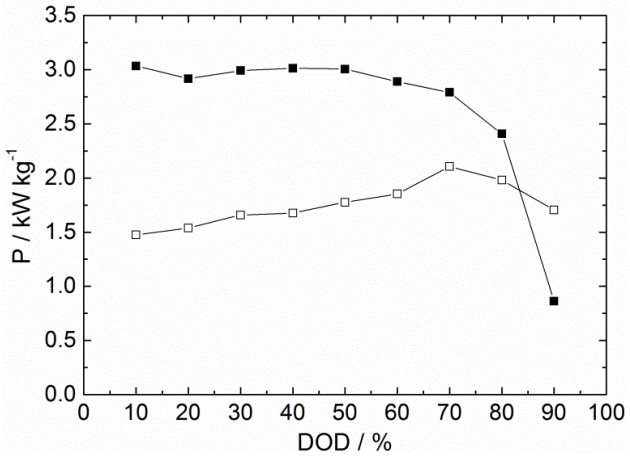


Figure 6.4. Specific power of discharge (full symbol) and regenerative (void symbol) pulses from HPPC test at 5C *vs.* DOD%. Reprinted from ref. [109], Copyright (2014), with permission from Elsevier.

Figure 6.5 is built by combining the cumulative energy data evaluated by the SC test of Figure 6.1a with those of discharge and regenerative powers of Figure 6.4 from the HPPC test at 5C. The two vertical axes are scaled in proportion to the discharge and regenerative power goals for the minimum power-assist HEV and the dashed horizontal line in the Figure identifies on *y*-axes the % DOD discharge and regenerative FreedomCAR power goals for the minimum power-assist HEV expressed in terms of specific values (0.625 discharge and 0.500 kW $kg^{-1}$ regenerative power pulses). The available energy, i.e. the energy removed during 1C-discharge over the DOD range for which the discharge and regenerative pulse power goals for a given mode (minimum or maximum power assist HEV) are precisely met, can be evaluated by the difference in the cumulative energy between the two vertical lines corresponding to the highest DOD that still provides enough power to meet the targets and the 10% DOD. The available energy removed by the PVdF-NCC cell is 82 Wh $kg^{-1}$, a value that largely surpass the energy target of 7.5 Wh $kg^{-1}$ for the minimum power-assist HEV. Moreover, as clearly evinced by the Figure, the cell can greatly overcome even the energy target for the maximum power-assist HEV (8.3 Wh $kg^{-1}$). The dotted segments between the discharge and regenerative pulse power curve shown in Figure 6.5 indicate the power pulses with lower available energy viable beyond these goals.

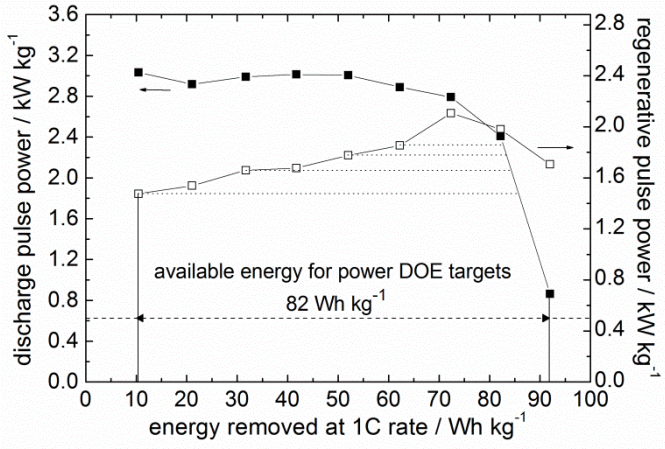


Figure 6.5. Cell with PVdF-NCC separator: specific discharge power (full symbol) and regenerative (void symbol) from HPPC test at 5C with the two vertical axes rescaled in proportion of discharge and regenerative power goals *vs.* energy removed during 1C discharge of Figure 6.1a. Reprinted from ref. [109], Copyright (2014), with permission from Elsevier.

The $R_{dis}$ and $R_{reg}$ values shown in Figure 6.6 were obtained from the low and high current HPPC tests (the 10C test ended at 70% DOD) carried out on the cell with Celgard®2400 separator at 30 °C. Figure 6.7 shows the specific discharge and regenerative power values by 5C HPPC tests *vs.* energy removed during the discharge at 1C. As explained for Figure 6.5, Figure 6.7 is built through the use of the cumulative energy data from the SC test of Figure 6.1b and displayed a specific available energy of 68 Wh $kg^{-1}$. Although this value is lower than that displayed by the cell with PVdF-NCC separator, also the Celgard cell can overcome the DOE energy target.

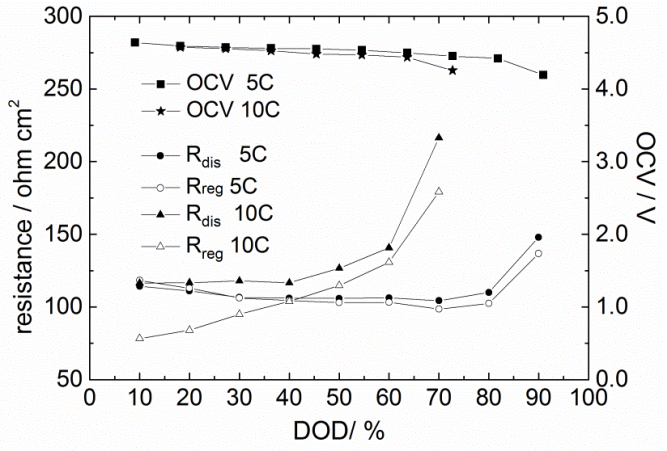


Figure 6.6. Cell with Celgard®2400 separator: open circuit voltage (OCV) and resistance from discharge (full symbol) and regenerative (void symbol) pulses *vs*. DOD% from HPPC tests at 5C and 10C (the last ends at 70%DOD). Reprinted from ref. [109], Copyright (2014), with permission from Elsevier.

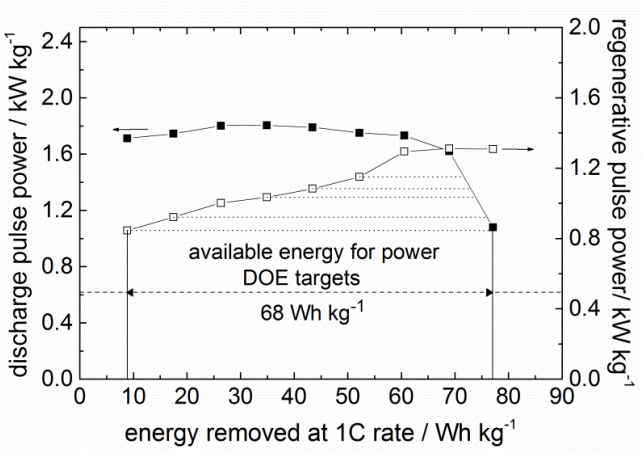


Figure 6.7. Specific discharge power (full symbol) and regenerative (void symbol) from HPPC test at 5C with the two vertical axes rescaled in proportion of discharge and regenerative power goals *vs.* energy removed during 1C discharge of Figure 6.1b. Reprinted from ref. [109], Copyright (2014), with permission from Elsevier.

Figure 6.8 compares the plots of available energy *vs.* discharge pulse power for the graphite//LNMO cells with PVdF-NCC and Celgard®2400 separators obtained by using the data of the HPPC tests at 5C (Figures 6.5 and 6.7) and those of high current (10C) HPPC tests. These plots display the energy (or power) available over the operating region where a specified power (or energy) demand can be met. The Figure shows that the DOE energy and power targets, which are indicated by the horizontal and vertical lines, for minimum (solid) and maximum (dashed) power-assist HEV are largely exceeded by both cells with the two different separators. However, the cell with PVdF-NCC performs notably better than the cell with Celgard®2400. These results are in good agreement with those previously discussed in Chapter 3 confirming that the reinforced fluorinated macroporous membrane effectively improve the electrochemical performance of the graphite//LNMO cells tested in LF30 with 1.6% $F_1EC$ and 2% SA at 30 °C with respect to that of cell with the conventional polyolefin separator: This findings demonstrated that the PVdF-NCC membrane is a suitable separator of notably interest for the development of high-voltage lithium-ion cells for automotive applications.

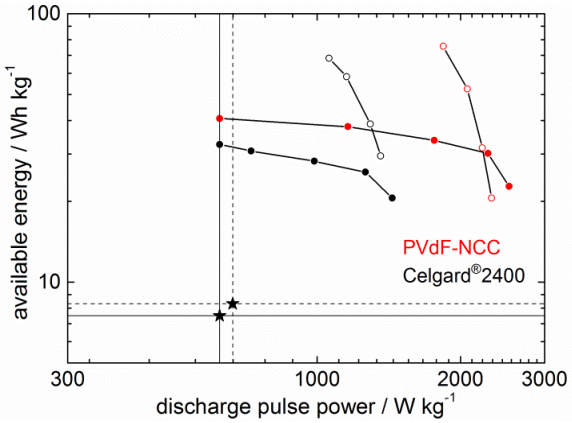


Figure 6.8. Plots of available energy for a given pulse-power *vs.* discharge pulse power for the cells with PVdF-NCC (red symbol) and Celgard®2400 (black symbol) separators from HPPC test at 5C (full symbol) and 10C (void symbol) in LF30-$F_1EC$-SA at 30 °C. Reprinted from ref. [109], Copyright (2014), with permission from Elsevier.

## 6.3 High-voltage graphite//$LiNi_{0.5}Mn_{1.5}O_4$ and graphite//$LiNi_{0.4}Mn_{1.6}O_4$ cells for plug-in HEV application

HPPC tests for plug-in hybrid electric vehicle (PHEV) applications were performed on lab-scale graphite//LNMO cells with pre-industrial electrodes of optimized formulation and active mass loading suitable for the scale-up of high-energy demanding lithium-ion batteries for PHEV applications and on graphite//LN05MO cells with both electrodes featuring the water-soluble carboxymethyl cellulose (CMC) binder instead of PVdF.

The graphite//LNMO cells were assembled with pre-industrial, high mass loading electrodes (balanced in capacity) of 0.636 $cm^2$ geometric area prepared at CEA-LITEN laboratories by a battery line in the frame of AMELIE Project. The graphite anode was based on commercial graphite and LNMO cathode on $LiNi_{0.4}Mn_{1.6}O_4$ active material synthesized by CEA-LITEN. The cells having PVdF-NCC or Celgard®2400 separators were tested in LP30 and LF30 electrolyte with $F_1$EC and SA additives at 30 °C.

The graphite//LN05MO cell with the electrodes balanced in capacity was assembled by using composite electrode of 1.13 $cm^2$. The graphite composite electrodes was based on commercial graphite and prepared at MEET by a battery line and the LN05MO composite electrodes was based on commercial $LiNi_{0.5}Mn_{1.5}O_4$. The cells was tested in commercial LP30 electrolyte with Whatman GF/D separator at 20 °C and 30 °C.

Table 6.2 shows the electrode formulation and active mass loading electrodes of the graphite//LN05MO and graphite//LNMO cells tested according to the DOE protocol for plug-in HEVs with different electrolytes and separators.

Table 6.2. Electrode formulation and active mass loading of graphite//LN05MO and graphite//LNMO cells tested according to DOE protocol for plug-in HEV application with different electrolytes and separators.

| *graphite//LNMO cell with PVdF-NCC or Celgard®2400 separators* | | | | |
|---|---|---|---|---|
| **electrode formulation / wt.%** | | **active mass loading / mg cm$^{-2}$** | | **electrolyte** |
| **graphite anode[(a)]** | **LNMO cathode[(a)]** | **graphite** | **LNMO** | |
| 91% SLA-1025<br>3% PureBLACK™<br>6% PVdF<br>(Solef®5130) | 92% LNMO<br>4% Super C65<br>4% PVdF<br>(Solef®5130) | 8.7 | 21.3 | LF30-$F_1$EC-SA<br>LP30-$F_1$EC-SA |
| *graphite//LN05MO cell with Whatman GF/D* | | | | |
| **electrode formulation (wt.%)** | | **active mass loading (mg cm$^{-2}$)** | | **electrolyte** |
| **graphite anode** | **LN05MO cathode** | **graphite** | **LN05MO** | |
| 90% SLP 30<br>5% Super C45<br>5% CMC | 85% LN05MO<br>10% Super C45<br>5% CMC | 3.3 | 9.4 | LP30 |

(a) pre-industrial electrodes

### 6.3.1 DOE battery tests for plug-in HEV applications on graphite//$LiNi_{0.4}Mn_{1.6}O_4$ cell with pre-industrial electrodes

The characterizations tests for PHEV applications were performed on graphite//LNMO cells having pre-industrial, high-mass loading electrodes with optimized composition. The cells were tested in LP30 and LF30 with additives (1.6 wt.% $F_1$EC and 2 wt.% SA) at 30 °C using PVdF-NCC and Celgard®2400 as separators.

Figure 6.9 shows the results of SC test over the last discharge of three cycles between 3.50 and 4.95 V at 2C effective rate corresponding to a discharge power ≥ 10 kW referred to minimum PHEV with 60 kg battery pack, namely 17 and 13 kW for PVdF-NCC and Celgard cells with LF30-$F_1$EC-SA, and 16 and 10 kW for PVdF-NCC and Celgard cells with LP30-$F_1$EC-SA.

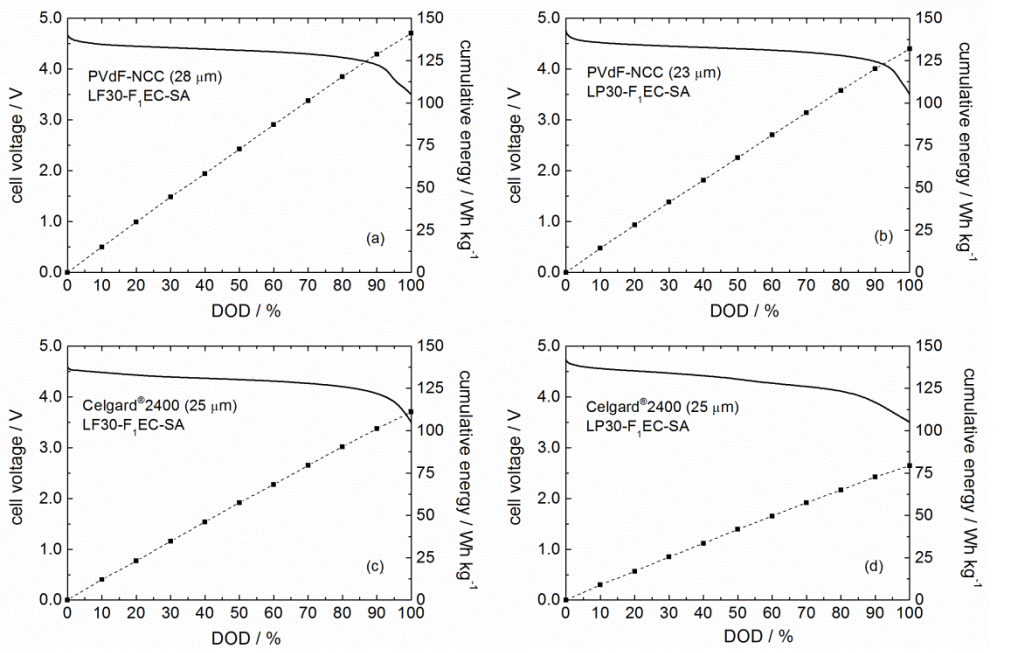


Figure 6.9. Discharge voltage profile (solid line) and cumulative specific energy (dashed line) at 2C effective rate at different DOD of the cells with (a) PVdF-NCC and LF30-$F_1$EC-SA (3.85 mA $cm^{-2}$), (b) PVdF-NCC and LP30-$F_1$EC-SA (3.55 mA $cm^{-2}$), (c) Celgard and LF30-$F_1$EC-SA (3.03 mA $cm^{-2}$), (d) Celgard and LP30-$F_1$EC-SA (2.12 mA $cm^{-2}$). Reprinted from ref. [119], Copyright (2014), with permission from Elsevier.

As expected from the data reported in Chapter 3, the cells tested in LF30 with $F_1$EC and SA additives display higher $E_{SCT}$ at 100 % DOD values than the cells tested in LP30-$F_1$EC-SA, with the highest values for the cells with PVdF-NCC. In particular, the cells with PVdF-NCC display 141 and 132 Wh $kg^{-1}$ in LF30-additives and LP30-additives, respectively, whereas the cells with Celgard®2400 display 111 and 79 Wh $kg^{-1}$.

The HPPC tests were performed on the graphite//LNMO cells at 5C current and, as an example, Figure 6.10 shows the HPPC voltage profile of the cell with PVdF-NCC separator and LP30-$F_1$EC-SA along the sequence from 10% to 90% DOD with discharge pulses at 5C (8.88 mA $cm^{-2}$) with the selected $V_{max}$ value of 5.0 V in

regenerative pulse and $V_{min}$ = 0.55 $V_{max}$ in discharge pulse. The inset in the Figure displays the magnification of the pulses at 10% DOD and the marked voltage values just before the discharge and regenerative pulses, $V_0$ and $V_2$, and those at the end of these pulses, $V_1$ and $V_3$, were used to calculate at each % DOD the discharge and regenerative pulse resistances, $R_{dis}$ and $R_{reg}$, by Eqs. 6.1 and 6.2 and then, the discharge and regenerative pulse-power, $P_{dis}$ and $P_{reg}$, by Eqs. 6.3 and 6.4.

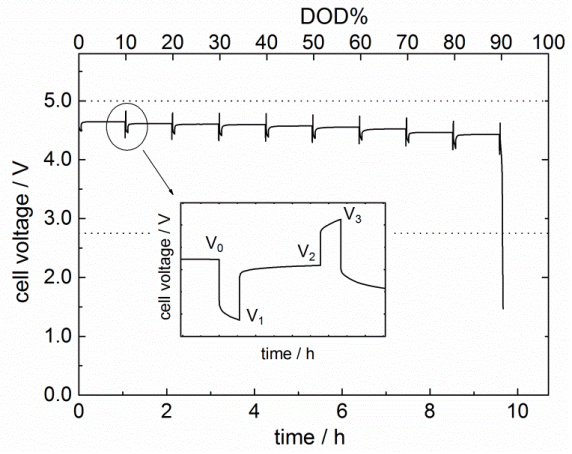


Figure 6.10. Cell voltage profile over HPPC at 5C of the cell with PVdF-NCC separator and LP30-$F_1$EC-SA. In the inset, the magnification of the discharge and regenerative pulses at 10% DOD. Reprinted from ref. [119], Copyright (2014), with permission from Elsevier.

The $R_{dis}$ and $R_{reg}$ values of the graphite//LNMO cells over the 5C current HPPC tests are compared in Figure 6.11 which shows that the PVdF-NCC cells display lower resistance values in both electrolytes with respect to those with Celgard®2400 and this can partly explain the higher $E_{SCT}$ values of the former cells.

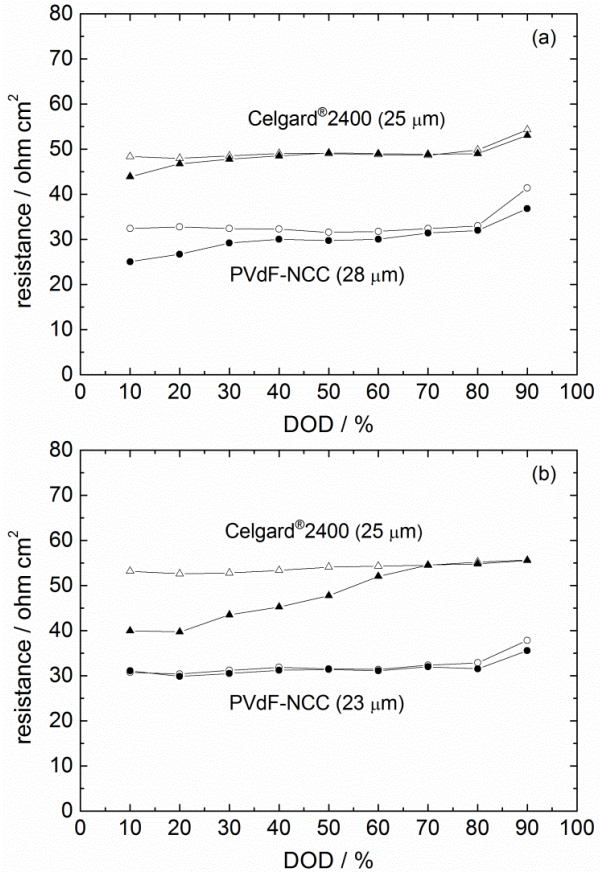


Figure 6.11. Discharge (empty symbol) and regenerative (full symbol) pulse resistances *vs.* DOD% from 5C HPPC on cells with PVdF-NCC and Celgard®2400 separators and (a) LF30-$F_1$EC-SA and (b) LP30-$F_1$EC-SA. Reprinted from ref. [119], Copyright (2014), with permission from Elsevier.

Although the resistances of cells with Celgard separator are almost the same in both electrolytes, the cumulative energy provided in LP30 with $F_1$EC and SA is significantly lower than in LF30-$F_1$EC-SA. This is presumably due to the presence in LF30 of LiFAP salt which shows higher stability toward hydrolysis and oxidation than $LiPF_6$ and, hence, its effect is more evident when Celgard separator is used.

Figure 6.12 shows the discharge and regenerative pulse power values estimated

at different DOD from 5C HPPC tests *vs.* energy removed at the 2C effective rate, shown in Figure 6.9, for the cells with the two separators and electrolytes. The dashed horizontal line on the *y*-axes identifies the discharge and regenerative DOE power goals for the minimum PHEV (0.750 kW $kg^{-1}$ and 0.500 kW $kg^{-1}$), and the available energy of the battery system at these power targets corresponds to the difference in the energy removed between the two vertical lines at 90% and 10% DOD. By taking into account the DOE energy targets for CS and CD operation modes ($AE_{CS\ Target}$ and $AE_{CD\ Target}$) reported in Table 2.3 (Chapter 2), the useable energy (UE) for each mode, $UE_{CS}$ and $UE_{CD}$, and the useable energy margin ($UE_M$) can be estimated as in ref. [111] by the following Equations:

$$UE_{CS} = (E_{90\%\ DOD} - E_{10\%\ DOD}) - \left(AE_{CD\ Target} - \tfrac{1}{2}\, AE_{CS\ Target}\right) \tag{6.5}$$

$$UE_{CD} = (E_{90\%\ DOD} - E_{10\%\ DOD}) - \tfrac{1}{2}\, AE_{CS\ Target} \tag{6.6}$$

$$UE_M = \left(UE_{CD} - AE_{CD\ Target}\right) = (UE_{CS} - AE_{CS\ Target}) \tag{67}$$

The first term in the $UE_{CS}$ and $UE_{CD}$ has to be substituted with the corresponding energy value if the HPPC test ends before 90% DOD. Considering that the DOE targets for CS and CD modes have to be met at the end-of-life of the battery system and that it is reasonable that the decrease of energy and power occurs over cycling and calendar life, the battery should provide sufficiently high energy margins, i.e. 20–30% of the $AE_{CD\ Target}$, at the beginning of battery life.

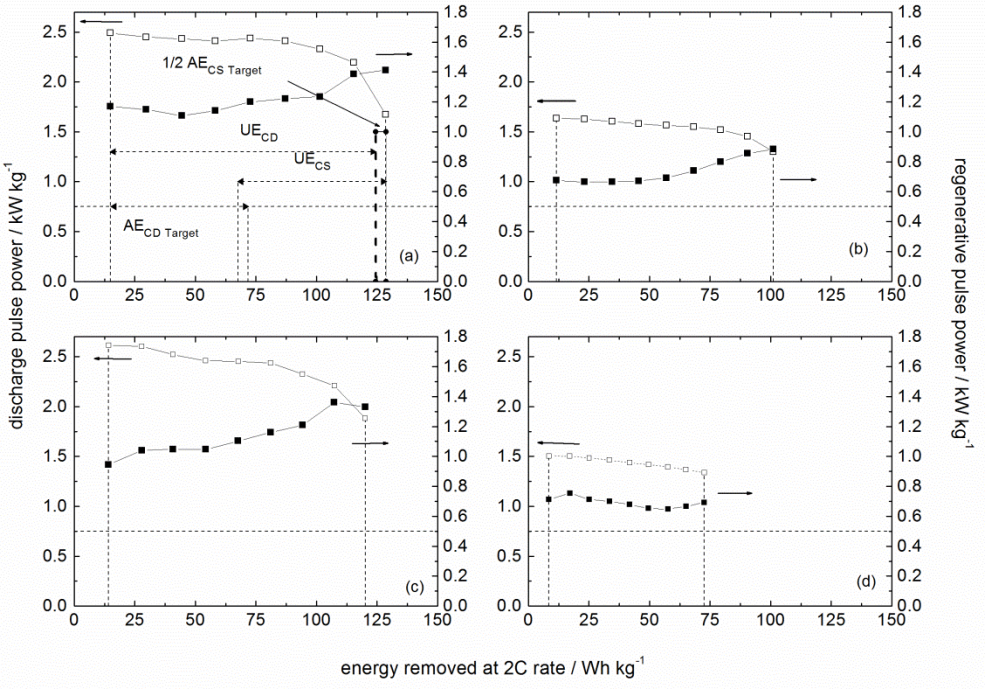


Figure 6.12. Discharge (empty symbol) and regenerative (full symbol) pulse power from 5C HPPC tests on cells with (a, c) PVdF-NCC or (b, d) Celgard®2400 separator and (a, b) LF30-$F_1$EC-SA or (c, d) LP30-$F_1$EC-SA. Reprinted from ref. [119], Copyright (2014), with permission from Elsevier.

Table 6.3 compares the experimental $E_{SCT}$, $UE_{CD}$, $UE_{CS}$ and $UE_M$ values for the graphite//LNMO cells with the two separators and electrolytes; the $AE_{CS\ Target}$ and $AE_{CD\ Target}$ for different PHEV types are also reported. The data of the Table highlight that the cells with PVdF-NCC separator can assure some energy margins in both electrolytes even when maximum PHEV targets are considered. By contrary, the cells with Celgard separator can assure a significant $UE_M$ only for minimum PHEV. These findings demonstrated that the change of electrolyte from LF30 to LP30 does not significantly affect the performance of cells with PVdF-NCC separator, whereas it has a remarkably effect on cells with Celgard, which meet the DOE energy target only for minimum PHEV with an unsatisfactory $UE_M$ value that is more than 10 times lower than that of cells with PVdF-NCC.

Table 6.3. Experimental $E_{SCT}$, $UE_{CD}$, $UE_{CS}$ and $UE_M$ values (in Wh $kg^{-1}$) of graphite//LNMO cells with different separators and electrolytes for different PHEV types. The DOE energy targets $AE_{CS}$ and $AE_{CD}$ are also reported. Reprinted from ref. [119], Copyright (2014), with permission from Elsevier.

| **Plug-in SCT&HPPC tests** | **$E_{SCT}$** | **Minimum PHEV** | | | **Medium PHEV** | | | **Maximum PHEV** | | |
|---|---|---|---|---|---|---|---|---|---|---|
| | | **$UE_{CD}$** | **$UE_{CS}$** | **$UE_M$** | **$UE_{CD}$** | **$UE_{CS}$** | **$UE_M$** | **$UE_{CD}$** | **$UE_{CS}$** | **$UE_M$** |
| *LF30 – 1.6% $F_1$EC – 2% SA* | | | | | | | | | | |
| PVdF-NCC (28 μm) | 141 | 110 | 61 | 53 | 112 | 33 | 29 | 113 | 18 | 16 |
| Celgard®2400 (25 μm) | 111 | 86 | 37 | 29 | 88 | 9 | 5 | 89 | - | - |
| *LP30 – 1.6% $F_1$EC – 2% SA* | | | | | | | | | | |
| PVdF-NCC (23 μm) | 132 | 102 | 53 | 45 | 104 | 25 | 21 | 105 | 10 | 8 |
| Celgard®2400 (25 μm) | 79 | 60 | 12 | 3 | 62 | - | - | 63 | - | - |
| $AE_{CD\ Target}$ | | | 57 | | | 83 | | | 97 | |
| $AE_{CS\ Target}$ | | | 8 | | | 4 | | | 3 | |

## 6.3.2 DOE battery tests for plug-in HEV application on graphite//$LiNi_{0.5}Mn_{1.5}O_4$ cells with CMC binder for both electrodes

The characterization tests for PHEV applications were also performed on graphite//LN05MO cells featuring both electrodes with CMC binder to investigate the feasibility of using water-soluble binder for the development of high-voltage lithium-ion batteries attractive for such automotive applications. Unlike the graphite anode which was prepared by the battery line at MEET, the LN05MO composite electrode was prepared by a laboratory doctor blade coater.

The cell performed the SC and HPPC tests after the cycling test in LP30 at 20 °C shown in Figure 5.11a (Chapter 5). The cumulative energy, removed over the SC test at 2C effective discharge rate (1.33 mA $cm^{-2}$), is 82 Wh $kg^{-1}$ at 100% DOD and corresponds to a 6.6 kW referred to minimum PHEV with 60 kg battery pack

(see Figure 5.11b).

Figure 6.13 shows the voltage profiles of the cell from 10% to 90% DOD upon the HPPC test with discharge pulses at 5C (3.32 mA $cm^{-2}$) with the selected $V_{max}$ value of 5.0 V in regenerative pulse and $V_{min}$ = 0.55 $V_{max}$ in discharge pulse. The inset in the Figure displays the magnification of the pulses at 10% DOD and the marked voltage values used to calculate at each % DOD the discharge and regenerative pulse resistances, $R_{dis}$ and $R_{reg}$, by Eqs. 6.1 and 6.2 and then, the discharge and regenerative pulse-power, $P_{dis}$ and $P_{reg}$, by Eqs. 6.3 and 6.4.

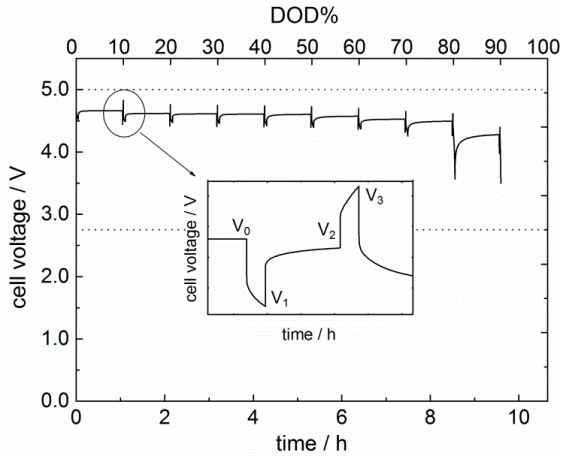


Figure 6.13. Cell voltage profile over HPPC at 5C of the graphite//LN05MO cell in LP30 at 20 °C. In the inset, the magnification of the discharge and regenerative pulses at 10% DOD.

Figure 6.14a shows the $R_{dis}$ and $R_{reg}$ and Figure 6.14b the discharge and regenerative pulse power values estimated at different DOD from 5C HPPC tests *vs.* energy removed at the 2C effective rate from SC test of Figure 5.11b.

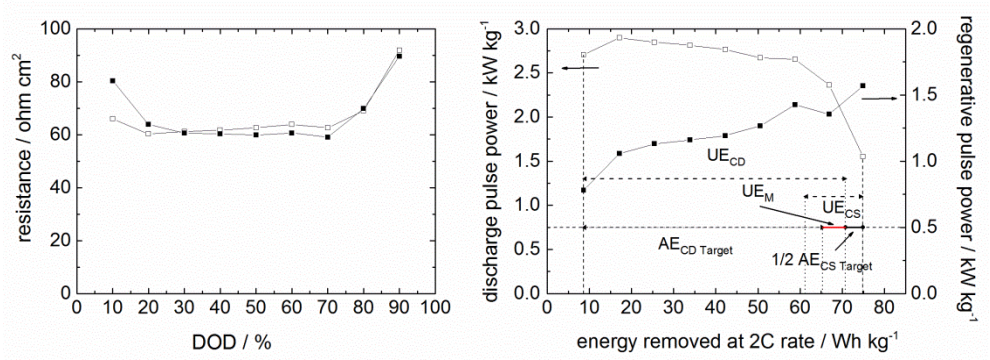


Figure 6.14. (a) Discharge (empty symbol) and regenerative (full symbol) pulse resistances *vs*. DOD% and (b) discharge (empty symbol) and regenerative (full symbol) pulse power from 5C HPPC tests on graphite//LN05MO cell in LP30 at 20 °C.

At the end of HPPC test at 20 °C, the graphite//LN05MO cell performed the SC and the 5C current HPPC tests also at 30 °C. The $E_{SCT}$ removed from the cell at 2C effective rate at 30 °C was 81.6 Wh $kg^{-1}$ which is only 0.73% less than that removed at 20 °C. However, during the discharge and regenerative pulses at 90% DOD the cell suffered a sharp resistances increase, as shown in Figure 6.15a which compares the discharge and regenerative pulse resistances *vs*. % DOD from 5C HPPC at 20 °C and 30 °C. As expected, the more facilitated side-reactions at 30 °C due to the oxidative electrolyte decomposition on LN05MO cathode surface justify this resistance increase. The cell can meet the DOE goals for discharge and regenerative pulse powers for the minimum PHEV up to 80% DOD as shown in Figure 6.15b which displays the discharge and regenerative pulse power values estimated at different DOD from 5C HPPC test.

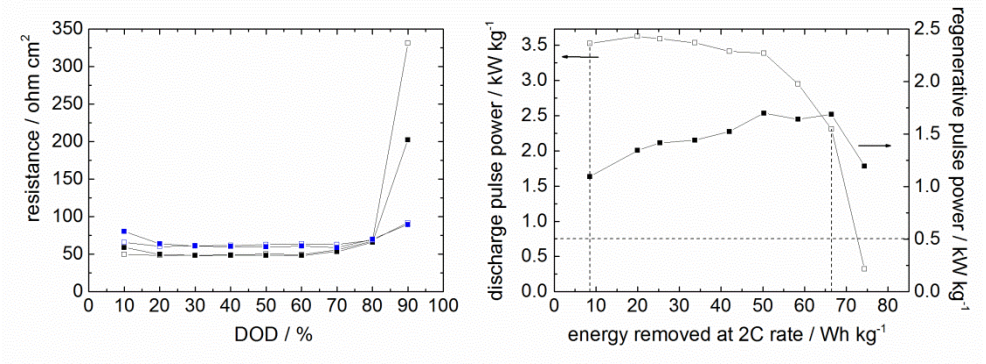


Figure 6.15. (a) Discharge (empty symbol) and regenerative (full symbol) pulse resistances *vs.* DOD% from 5C HPPC on graphite//LN05MO cell in LP30 at 20 °C (blue symbol) and 30 °C (black symbol); (b) discharge (empty symbol) and regenerative (full symbol) pulse power from 5C HPPC tests on graphite//LN05MO cell in LP30 at 30 °C.

The experimental $E_{SCT}$, $UE_{CD}$, $UE_{CS}$ and $UE_M$ values for the graphite//LN05MO cell as well as the $AE_{CS\ Target}$ and $AE_{CD\ Target}$ for minimum PHEV type are summarized in Table 6.4 which clearly shows that the values of usable energy can assure some margin only after the HPPC test at 20 °C. However, it is worthy that these results were obtained on graphite//LN05MO cells featuring LN05MO composite electrode with composition and mass loading not still optimized. In fact, pre-industrial electrodes are necessary to fulfil the high-demanding energy and power DOE targets for PHEVs, as demonstrated by the successful results on graphite//LNMO cells with pre-industrial electrodes of optimized composition and mass loading.

However, these preliminary findings are very promising and highlight that the use of water-soluble CMC binder for graphite anode and $LiNi_{0.5}Mn_{1.5}O_4$ cathode is a very attractive and sustainable approach for the development of high-voltage lithium-ion batteries operating in conventional electrolyte, i.e. LP30 without additives, for plug-in hybrid electric vehicles.

Table 6.4. Experimental $E_{SCT}$, $UE_{CD}$, $UE_{CS}$ and $UE_M$ values (in Wh $kg^{-1}$) of graphite//LN05MO cell featuring both electrodes with CMC binder for minimum PHEV type in LP30 with Whatman GF/D separator. The DOE energy targets $AE_{CS}$ and $AE_{CD}$ are also reported.

| **Plug-in SCT&HPPC tests** | **$E_{SCT}$** | **Minimum PHEV** | | |
|---|---|---|---|---|
| | | **$UE_{CD}$** | **$UE_{CS}$** | **$UE_M$** |
| *graphite-CMC//LN05MO-CMC cell in LP30* | | | | |
| 20 °C | 82.2 | 62.1 | 13.7 | 5 |
| 30 °C | 81.6 | 53.8 | 5.4 | - |
| $AE_{CD\ Target}$ | | | 57 | |
| $AE_{CS\ Target}$ | | | 8 | |

## 6.4 Conclusions

For the first time, characterization tests according to the DOE protocols to simulate the performance of lithium-ion cell in power-assist HEV and plug-in HEV were performed on lab-scale high-voltage cells with graphite anode and $LiNi_{0.4}Mn_{1.6}O_4$ (LNMO) or $LNi_{0.5}Mn_{1.5}O_4$ (LN05MO) cathode, also with pre-industrial, high-mass loading electrodes suitable for battery scale-up for automotive applications. The results of the static capacity (SC) test and hybrid pulse power characterization (HPPC) tests highlight that the combination of graphite anode with LNMO or LN05MO cathodes yields lithium-ion cells suitable for power-assist and plug-in HEV application and energy values of full cells with LNMO or LN05MO and different electrolytes, separators and binders are summarized in Table 6.5.

Table 6.5. Experimental cumulative energy values ($E_{SCT}$ in Wh $kg^{-1}$) removed from full cells with different electrolytes, separators and electrode binders at 1C and 2C effective rate according to DOE protocols for power-assist HEV and PHEV, respectively.

| full cell | electrolyte | separator | binder | $E_{SCT}$ | C-rate |
|---|---|---|---|---|---|
| graphite//LNMO | LF30-$F_1$EC-SA | PVdF-NCC | PVdF | 101 | 1C[(a)] |
| | | Celgard®2400 | | 85 | |
| graphite//LNMO (pre-industrial, high mass loading electrodes) | LF30-$F_1$EC-SA | PVdF-NCC | PVdF | 141 | 2C[(b)] |
| | | Celgard | | 111 | |
| | LP30-$F_1$EC-SA | PVdF-NCC | | 132 | |
| | | Celgard | | 79 | |
| graphite//LN05MO | LP30 | Whatman GF/D | CMC | 82 | 2C[(b)] |

(a) DOE protocols for power-assist HEV

(b) DOE protocols for PHEV

The results of the power-assist HEVs performed at 5C and 10C on the graphite//LNMO cells with low-mass loading electrodes, PVdF-NCC or Celgard®2400 separator in LF30-$F_1$EC-SA demonstrate the superior performance of the cells with the fluorinated macroporous PVdF-NCC separator with respect to those with the commercial polypropylene Celgard®2400, even if both cells exceed the FreedomCAR goals of power and energy for minimum and maximum power-assist HEV.

The results of HPPC tests for plug-in HEVs on graphite//LNMO cells with pre-industrial, high-mass loading electrodes highlight the outstanding performance of the cells with PVdF-NCC separator both in LF30 and LP30 with additives and demonstrate once again the strong and beneficial impact of this separator. These cells exceed the targets even for medium PHEVs with margins of 35% in LF30-$F_1$EC-SA and 25% in LP30-$F_1$EC-SA. On the other hand, the cells with Celgard separator are able to provide satisfactory useable energy margins only for minimum PHEV in LF30-$F_1$EC-SA; the highest energy values in LF30 based electrolytes

highlight the need for new fluorinated salts and/or solvents, since LF30 is no longer commercialized.

The results of the characterization tests for PHEVs on graphite//LN05MO cell with CMC electrodes' binder, LP30 electrolyte without additives and electrodes not still optimized in terms of formulation and mass loading are very promising and indicate that the use of CMC binder is a feasible and sustainable approach to develop high-voltage lithium-ion batteries operating in conventional electrolyte for plug-in HEV applications.

# Chapter 7. Conclusions

This PhD work investigated $LiNi_{0.4}Mn_{1.6}O_4$ (LNMO) and $LiNi_{0.5}Mn_{1.5}O_4$ (LN05MO) as high-voltage cathode materials for high-energy lithium-ion batteries, mainly for the use in hybrid electric vehicle (HEV) applications. The study highlights the great importance of the appropriate selection of battery components, such as electrolyte, separator, conductive additive and electrode binder that strongly affect the electrode/electrolyte interface, especially when LNMO and LN05MO cathode materials are involved. These materials, operating at 4.7 V *vs.* $Li^+/Li$, demand battery components stable at such a high potential where the oxidative electrolyte decomposition on the cathode surface is more facilitated.

Fluorinated materials have been proved to play a key role for the electrochemical performance of graphite//LNMO cells. The study on the effect of LF30 electrolyte having a non-conventional lithium salt (lithium tris(pentafluoroethyl)trifluorophosphate, LiFAP, which is more stable at high potentials than conventional $LiPF_6$ even in presence of $F_1$EC and SA additives, and of the fluorinated macroporous PVdF separator reinforced with nanocrystalline cellulose (NCC) demonstrated their beneficial impact in mitigating the side-reactions between LNMO and electrolyte, leading to a stable electrode/electrolyte interface. This yielded full cells with significantly enhanced capacity retention, cycling stability and self-discharge after fully charge up to 4.95 V with respect to those with the commercial polypropylene Celgard®2400 separator. PVdF-NCC, providing a better compatibility with the electrodes than Celgard, gives a lower and more stable ion transport resistance, which positively affects the battery performance at high rates.

The study on the effect of different conducting additives, namely carbon blacks, home-made prepared partially reduced graphene oxide (pRGO) and commercial

RGO demonstrated that the coatings of LN05MO by pRGO and the addition of RGO to LN05MO improved in presence of carbon black the electrode/electrolyte interface in conventional LP30, by functioning as a protective barrier that hinders the formation of a thick passivation layer of low electronic conductivity on the cathode surface due to the side-reactions with the electrolyte. Moreover, it was also highlighted that the charge cut-off voltage and the C-rate have an important effect on the cycling stability of LN05MO, as demonstrated by the superior stability of the LN05MO electrodes with charges up to 4.80 V instead of 4.85 V *vs.* $Li^+/Li$ over cycling at 1C.

The study on the effect of the water-soluble carboxymethyl cellulose (CMC) binder demonstrated that CMC strongly affects LN05MO's performance, remarkably improving its cycling stability and capacity retention, especially upon long-term cycling in LP30 with respect to the LN05MO-PVdF electrodes, both at 20 °C and 40 °C. Thanks to its more effective ability of in bridging the particles compared to PVdF, CMC promotes a homogeneous three-dimensional percolating network between the conductive carbon and the LN05MO particles, which results in a homogeneous electrode surface, more compact and stable than that of electrodes with PVdF. This prevents the unwanted reactions between the electrode and electrolyte upon high-operating voltages, reducing the formation of a thick surface layer on the LN05MO surface, as demonstrated by the slower resistance increase over cycling for the CMC-based electrodes with respect to the LN05MO-PVdF ones, which suffer from a sharp capacity fading.

Finally, in view of the use of LNMO and LN05MO cathode materials in lithium-ion batteries for power-assist and plug-in HEV applications, full cells with graphite anode were assembled and tested according to the U.S. Department of Energy (DOE) battery test protocol for power-assist HEV and plug-in HEV applications. The results demonstrated that the graphite//LNMO cells tested in LF30-$F_1$EC-SA with PVdF-NCC and Celgard®2400 separators can meet the DOE

energy and power targets for power-assist HEVs. Furthermore, full cells with pre-industrial graphite and LNMO electrodes with optimized formulation and mass loading suitable for battery scale-up, PVdF-NCC separator and LF30-$F_1$EC-SA, fulfil the energy and power requirements for high-energy demanding plug-in HEVs These cells exceeded the DOE targets for all the three PHEVs types, demonstrating that the development of high-voltage lithium-ion batteries based on lithium nickel manganese oxide cathodes is a promising and viable approach to effectively improve the energy of the lithium-ion batteries for automotive applications.

Moreover, the preliminary results of the characterization tests for PHEVs on graphite//LN05MO cells with CMC electrodes' binder, LP30 electrolyte without additives and electrodes not still optimized for automotive applications, highlight that the use of CMC is a very promising and sustainable approach to develop high-voltage lithium-ion batteries operating in conventional electrolyte and suitable for PHEV applications.

# Bibliography


1. International Energy Agency. *Key Trends in $CO_2$ emissions*. http://www.iea.org/publications/freepublications/publication/CO2EmissionsTrends.pdf. (Last visited on 12.01.2016)

2. D. Larcher, J.-M. Tarascon, *Nat. Chem.*, **7**, 19–29 (2014).

3. H. Helms, C. Kämper, U. Lambrecht in *Advances in Battery Technologies for Electric Vehicles*, B. Scrosati, J. Garche and W. Tillmetz Eds., Woodhead Publishing Ltd., 17–34 (2015).

4. The 7th Environment Action Programme (2014-20). http://ec.europa.eu/environment/action-programme/. (Last visited on 14.01.2016)

5. B. Dunn, H. Kamath, J.-M. Tarascon, *Science*, **334**, 928–935 (2011).

6. C. J. Rydh, B. A. Sandén, *Energy Convers. Manag.*, **46**, 1980–2000 (2005).

7. B. Scrosati, J. Garche, *J. Power Sources*, **195**, 2419–2430 (2010).

8. F. Orecchini, A. Santiangeli, A. Dell'Era in *Lithium-Ion Batteries: Advances and Applications*, G. Pistoia Ed., Elsevier, 205–248 (2014).

9. B. Scrosati in *Lithium Batteries: Advanced Technologies and Applications*, B. Scrosati, K. M. Abraham, W. A. van Schalkwijk and J. Hassoun Edts., John Wiley & Sons Wiley, 21–38 (2013).

10. N. S. Choi, Z. Chen, S. A. Freunberger, X. Ji, Y.-K. Sun, K. Amine, G. Yushin, L. F. Nazar, J. Cho, P. G. Bruce, *Angew. Chem. Int. Ed.*, **51**, 9994–10024 (2012).

11. K. M. Abraham, *J. Phys. Chem. Lett.*, **6**, 830–844 (2015).

12. E. J. Berg, C. Villevieille, D. Streich, S. Trabesinger, P. Novák, *J. Electrochem. Soc.*, **162**, A2468–A2475 (2015).

13. R. Marom, S. F. Amalraj, N. Leifer, D. Jacob, D. Aurbach, *J. Mater. Chem.*, **21**, 9938–9954 (2011).

14. M. S. Whittingham, *Chem. Rev.*, **104**, 4271–4301 (2004).

15. M. Hu, X. Pang, Z. Zhou, *J. Power Sources*, **237**, 229–242 (2013).

16. P. Mohan, G. P. Kalaignan, *Ionics*, **19**, 895–902 (2012).

17. S. Patoux, L. Sannier, H. Lignier, Y. Reynier, C. Bourbon, S. Jouanneau, F. Le Cras, S. Martinet, *Electrochim. Acta*, **53**, 4137–4145 (2008).

18. D. Doughty, E. P. Roth, *Electrochem. Soc. Interface*, 37–44 (2012).

19. X. Rui, Q. Yan, M. Skyllas-Kazacos, T. M. Lim, *J. Power Sources*, **258**, 19–38 (2014).

20. V. Aravindan, J. Gnanaraj, Y.-S. Lee, S. Madhavi, *J. Mater. Chem. A*, **1**, 3518–3539 (2013).

21. C. Wang, Y. Bi, Y. Liu, Y. Qin, Y. Fang, D. Wang, *J. Power Sources*, **263**, 332–337 (2014).

22. J. Hong, H. Gwon, S.-K. Jung, K. Ku, K. Kang, *J. Electrochem. Soc.*, **162**, A2447–A2467 (2015).

23. D. Liu, W. Zhu, J. Trottier, C. Gagnon, F. Barray, A. Guerfi, A. Mauger, H. Groult, C. M. Julien, J. B. Goodenough, K. Zaghib, *RSC Adv.*, **4**, 154–167 (2014).

24. A. Padhi, K. Nanjundaswamya, J. Goodenough, *J. Electrochem. Soc.*, **144**, 1188–1194 (1997).

25. F. Wang, J. Yang, Y. NuLi, J. Wang, *Electrochim. Acta*, **103**, 96–102 (2013).

26. C. Arbizzani, L. Da Col, F. De Giorgio, M. Mastragostino, F. Soavi, *ECS Trans.*, **66**, 139–147 (2015).

27. R. Santhanam, B. Rambabu, *J. Power Sources*, **195**, 5442–5451 (2010).

28. A. M. C. M. Julien, *Ionics*, **19**, 951–988 (2013).

29. K. Amine, H. Tukamoto, H. Yasuda, Y. Fujita, *J. Power Sources*, **68**, 604–608 (1997).

30. Q. Zhong, A. Bonakclarpour, M. Zhang, Y. Gao, J. R. Dahn, *J. Electrochem. Soc.*, **144**, 205–213 (1997).

31. J.-H. Kim, S.-T. Myung, C. S. Yoon, S. G. Kang, Y.-K. Sun, *Chem. Mater.*, **16**, 906–914 (2004).

32. J. Yang, X. Han, X. Zhang, F. Cheng, J. Chen, *Nano Res.*, **6**, 679–687 (2013).

33. K. Ariyoshi, Y. Iwakoshi, N. Nakayama, T. Ohzuku, *J. Electrochem. Soc.*, **151**, A296–A303 (2004).

34. S. Patoux, L. Daniel, C. Bourbon, H. Lignier, C. Pagano, F. Le Cras, S. Jouanneau, S. Martinet, *J. Power Sources*, **189**, 344–352 (2009).

35. K. Xu, *Chem. Rev.*, **104**, 4303–4417 (2004).

36. R. Younesi, G. M. Veith, P. Johansson, K. Edstrom, T. Vegge, *Energy Environ. Sci.*, **8**, 1905–1922 (2015).

37. D. Aurbach in *Advances in Lithium-ion Batteries,* W. A. van Schalkwijk and B. Scrosati Eds., Kluwer Academic/Plenum Publishers, New York, 7–77 (2002).

38. D. Aurbach, M. Moshkovich, Y. Cohen, A. Schechter, *Langmuir*, **15**, 2947–2960 (1999).

39. M. Moshkovich, M. Cojocaru, H. E. Gottlieb, D. Aurbach, *J. Electroanal. Chem.*, **497**, 84–96 (2001).

40. S. E. Sloop, J. B. Kerr, K. Kinoshita, *J. Power Sources*, **119-121**, 330–337 (2003).

41. P. G. Balakrishnan, R. Ramesh, T. Prem Kumar, *J. Power Sources*, **155**, 401–414 (2006).

42. E. P. Roth, C. J. Orendorff, *Interface*, **21**, 45–50 (2012).

43. K. Xu, *Chem. Rev.*, **114**, 11503–11618 (2014).

44. V. Borgel, E. Markevich, D. Aurbach, G. Semrau, M. Schmidt, **189**, 331–336 (2009).

45. N.-S. Choi, J.-G. Han, S.-Y. Ha, I. Park, C.-K. Back, *RSC Adv.*, **5**, 2732–2748 (2015).

46. Z. Zhang, L. Hu, H. Wu, W. Weng, M. Koh, P. C. Redfern, L. A. Curtiss, K. Amine, *Energy Environ. Sci.*, **6**, 1806–1810 (2013).

47. L. Hu, Z. Zhang, K. Amine, *Electrochem. Commun.*, **35**, 76–79 (2013).

48. E. M. Erickson, E. Markevich, G. Salitra, D. Sharon, D. Hirshberg, E. de la

Llave, I. Shterenberg, A. Rozenman, A. Frimer, D. Aurbach, *J. Electrochem. Soc.*, **162**, A2424–A2438 (2015).

49. M. He, L. Hu, Z. Xue, C. C. Su, P. Redfern, L. A. Curtiss, B. Polzin, A. von Cresce, K. Xu, Z. Zhang, *J. Electrochem. Soc.*, **162**, A1725–A1729 (2015).

50. M. Schmidt, U. Heider, A. Kuehner, R. Oesten, M. Jungnitz, N. Ignat'ev, P. Sartori, *J. Power Sources*, **97-98**, 557–560 (2001).

51. J. S. Gnanaraj, M. D. Levi, Y. Gofer, D. Aurbach, M. Schmidt, *J. Electrochem. Soc.*, 445–454 (2003).

52. J. S. Gnanaraj, E. Zinigrad, M. D. Levi, D. Aurbach, M. Schmidt, *J. Power Sources*, **121**, 799–804 (2003).

53. D. Aurbach, *J. Power Sources*, **119-121**, 497–503 (2003).

54. S. S. Zhang, *J. Power Sources*, **162**, 1379–1394 (2006).

55. L. Yang, T. Markmaitree, B. L. Lucht, *J. Power Sources*, **196**, 2251–2254 (2011).

56. S. Dalavi, M. Xu, B. Knight, B. L. Lucht, *Electrochem. Solid-State Lett.*, **15**, A28–A31 (2012).

57. A. von Cresce, K. Xu, *J. Electrochem. Soc.*, **158**, A337–A342 (2011).

58. H. Bouayad, Z. Wang, N. Dupré, R. Dedryvère, D. Foix, S. Franger, J. F. Martin, L. Boutafa, S. Patoux, D. Gonbeau, D. Guyomard, *J. Phys. Chem. C*, **118**, 4634–4648 (2014).

59. H. Lee, S. Choi, S. Choi, H.-J. Kim, Y. Choi, S. Yoon, J.-J. Cho, *Electrochem. Commun.*, **9**, 801–806 (2007).

60. V. Tarnopolskiy, J. Kalhoff, M. Nádherná, D. Bresser, L. Picard, F. Fabre, M. Rey, S. Passerini, *J. Power Sources*, **236**, 39–46 (2013).

61. Y.-K. Sun, K. J. Hong, J. Prakash, K. Amine, *Electrochem. Commun.*, **4**, 344–348 (2002).

62. Y. Fan, J. Wang, Z. Tang, W. He, J. Zhang, *Electrochim. Acta*, **52**, 3870–3875 (2007).

63. Y. Kobayashi, H. Miyashiro, K. Takei, H. Shigemura, M. Tabuchi, H. Kageyama, T. Iwahori, *J. Electrochem. Soc.*, **150**, A1577–A1582 (2003).

64. J. Wang, S. Yao, W. Lin, B. Wu, X. He, J. Li, J. Zhao, *J. Power Sources*, **280**, 114–124 (2015).

65. H.-M. Cho, M. V. Chen, A. C. MacRae, Y. S. Meng, *ACS Appl. Mater. Interfaces*, **7**, 16231–16239 (2015).

66. D. A. C. Brownson, C. E. Banks, *Analyst*, **135**, 2768–2778 (2010).

67. G. Kucinskis, G. Bajars, J. Kleperis, *J. Power Sources*, **240**, 66–79 (2013).

68. J. Zhu, D. Yang, Z. Yin, Q. Yan, H. Zhang, *Small*, **10**, 3480–3498 (2014).

69. R. Raccichini, A. Varzi, S. Passerini, B. Scrosati, *Nat. Mater.*, **14**, 271–9 (2015).

70. X. Fang, M. Y. Ge, J. P. Rong, C. W. Zhou, *J. Mater. Chem. A*, **1**, 4083–4088 (2013).

71. S. J. R. Prabakar, Y.-H. Hwang, B. Lee, K.-S. Sohn, M. Pyo, *J. Electrochem. Soc.*, **160**, A832–A837 (2013).

72. P. Arora, Z. Zhang, *Chem. Rev.*, **104**, 4419–4462 (2004).

73. S. S. Zhang, *J. Power Sources*, **164**, 351–364 (2007).

74. K. K. Patel, J. M. Paulsen, J. Desilvestro, *J. Power Sources*, **122**, 144–152 (2003).

75. M. J. Martínez, S. Shimpalee, J. W. Van Zee, *J. Electrochem. Soc.*, **156**, B80–B85 (2009).

76. E. P. Roth, D. H. Doughty, D. L. Pile, *J. Power Sources*, **174**, 579–583 (2007).

77. F. C. Laman, M. A. Gee, J. Denovan, *J. Electrochem. Soc.*, **140**, L51 (1993).

78. C. J. Orendorff, *Interface*, **21**, 61–65 (2012).

79. C. M. Costa, M. M. Silva, S. Lanceros-Méndez, *RSC Adv.*, **3**, 11404-11417 (2013).

80. C. M. Costa, J. L. Gomez Ribelles, S. Lanceros-Méndez, G. B. Appetecchi, B. Scrosati, *J. Power Sources*, **245**, 779–786 (2014).

81. D. Bansal, B. Meyer, M. Salomon, *J. Power Sources*, **178**, 848–851 (2008).

82. E. S. Pampal, E. Stojanovska, B. Simon, A. Kilic, *J. Power Sources*, **300**, 199–215 (2015).

83. M. Zaccaria, D. Fabiani, G. Cannucciari, C. Gualandi, M. L. Focarete, C. Arbizzani, F. De Giorgio, M. Mastragostino, **162**, 915–920 (2015).

84. J.-M. Tarascon, A. S. Gozdz, C. Schmutz, F. Shokoohi, P. C. Warren, *Solid State Ionics*, **86–88**, 49–54 (1996).

85. F. Boudin, X. Andrieu, C. Jehoulet, I. I. Olsen, *J. Power Sources*, **81-82**, 804–807 (1999).

86. J. Saunier, F. Alloin, J. Y. Sanchez, G. Caillon, *J. Power Sources*, **119-121**, 454–459 (2003).

87. D. Djian, F. Alloin, S. Martinet, H. Lignier, *J. Power Sources*, **187**, 575–580 (2009).

88. J. Saunier, F. Alloin, J. Y. Sanchez, B. Barrière, *J. Polym. Sci. B Polym. Phys.*, **42**, 532–543 (2004).

89. J. Saunier, F. Alloin, J. Y. Sanchez, B. Barrière, *J. Polym. Sci. B Polym. Phys.*, **42**, 544–552 (2004).

90. J. Saunier, F. Alloin, J. Y. Sanchez, L. Maniguet, *J. Polym. Sci. B Polym. Phys.*, **42**, 2308–2317 (2004).

91. B. S. Lalia, Y. A. Samad, R. Hashaikeh, *J. Solid State Electrochem.*, **17**, 575–581 (2013).

92. A. Samir, F. Alloin, J. Sanchez, A. Dufresne, *Electrochim. Acta*, **50**, 4839–4844 (2004).

93. S. Pejovnik, R. Dominko, M. Bele, M. Gaberscek, J. Jamnik, *J. Power Sources*, **184**, 593–597 (2008).

94. A. Guerfi, M. Kaneko, M. Petitclerc, M. Mori, K. Zaghib, *J. Power Sources*, **163**, 1047–1052 (2007).

95. S.-L. Chou, Y. Pan, J.-Z. Wang, H.-K. Liu, S.-X. Dou, *Phys. Chem. Chem. Phys.*, **16**, 20347–20359 (2014).

96. I. Kovalenko, B. Zdyrko, A. Magasinski, B. Hertzberg, Z. Milicev, R. Burtovyy, I. Luzinov, G. Yushin, *Science*, **334**, 75–79 (2011).

97. L. Chai, Q. Qu, L. Zhang, M. Shen, L. Zhang, H. Zheng, *Electrochim. Acta*, **105**, 378–383 (2013).

98. P. P. Prosini, M. Carewska, C. Cento, A. Masci, *Electrochim. Acta*, **150**, 129–135 (2014).

99. S. F. Lux, F. Schappacher, A. Balducci, S. Passerini, M. Winter, *J. Electrochem. Soc.*, **157**, A320–A325 (2010).

100. J. Drofenik, M. Gaberscek, R. Dominko, F. W. Poulsen, M. Mogensen, S. Pejovnik, J. Jamnik, *Electrochim. Acta*, **48**, 883–889 (2003).

101. B. Lestriez, S. Bahri, I. Sandu, L. Roue, D. Guyomard, *Electrochem. Commun.*, **9**, 2801–2806 (2007).

102. G. T. Kim, S. S. Jeong, M. Joost, E. Rocca, M. Winter, S. Passerini, A. Balducci, *J. Power Sources*, **196**, 2187–2194 (2011).

103. J. Li, R. Klöpsch, S. Nowak, M. Kunze, M. Winter, S. Passerini, *J. Power Sources*, **196**, 7687–7691 (2011).

104. Z. Wang, N. Dupré, A.-C. Gaillot, B. Lestriez, J.-F. Martin, L. Daniel, S. Patoux, D. Guyomard, *Electrochim. Acta*, **62**, 77–83 (2012).

105. W.-Y. Chou, Y.-C. Jin, J.-G. Duh, C.-Z. Lu, S.-C. Liao, *Appl. Surf. Sci.*, **355**, 1272–1278 (2015).

106. J.-H. Lee, U. Paik, V. A. Hackley, Y.-M. Choi, *J. Electrochem. Soc.*, **152**, A1763–A1769 (2005).

107. K. A. Seid, J. C. Badot, O. Dubrunfaut, S. Levasseur, D. Guyomard, B. Lestriez, *J. Mater. Chem.*, **22**, 24057–24066 (2012).

108. S. Monaco, F. De Giorgio, L. Da Col, M. Riché, C. Arbizzani, M. Mastragostino, *J. Power Sources*, **278**, 733–740 (2015).

109. C. Arbizzani, F. Colò, F. De Giorgio, M. Guidotti, M. Mastragostino, F. Alloin, M. Bolloli, Y. Molméret, J. Y. Sanchez, *J. Power Sources*, **246**, 299–304

(2014).

110. FreedomCAR Battery Test Manual for Power-Assist Hybrid Electric Vehicles, October 2003.

111. Battery Test Manual for Plug-In Hybrid Electric Vehicles, U.S. Department of Energy, December 2010. Vehicle Technologies Program, Revision 2 (2010)

112. C. Arbizzani, F. De Giorgio, L. Porcarelli, M. Mastragostino, V. Khomenko, V. Barsukov, D. Bresser, S. Passerini, *J. Power Sources*, **238**, 17–20 (2013).

113. D. Guyomard, J. M. Tarascon, *J. Power Sources*, **54**, 92–98 (1995).

114. G. Pistoia, A. Antonini, R. Rosati, D. Zane, *Electrochim. Acta*, **41**, 2683–2689 (1996).

115. J. Vetter, P. Novák, M. R. Wagner, C. Veit, K.-C. Möller, J. O. Besenhard, M. Winter, M. Wohlfahrt-Mehrens, C. Vogler, A. Hammouche, *J. Power Sources*, **147**, 269–281 (2005).

116. L. Yang, B. Ravdel, B. L. Lucht, *Electrochem. Solid-State Lett.*, **13**, A95–A97 (2010).

117. R. Dedryvère, D. Foix, S. Franger, S. Patoux, L. Daniel, D. Gonbeau, *J. Phys. Chem. C*, **114**, 10999–11008 (2010).

118. C. Arbizzani, F. De Giorgio, M. Mastragostino in *Advances in Battery Technologies for Electric Vehicles*, B. Scrosati, J. Garche and W. Tillmetz Eds., Woodhead Publishing Ltd., 55–72 (2015).

119. C. Arbizzani, F. De Giorgio, M. Mastragostino, *J. Power Sources*, **266**, 170–174 (2014).

120. C. Arbizzani, L. Da Col, F. De Giorgio, M. Mastragostino, F. Soavi, *J. Electrochem. Soc.*, **162**, A2174–A2179 (2015).

121. N. P. W. Pieczonka, Z. Liu, P. Lu, K. L. Olson, J. Moote, B. R. Powell, J.-H. Kim, *J. Phys. Chem.*, **117**, 15947–15957 (2013).

122. R. Qiao, Y. Wang, P. Olalde-Velasco, H. Li, Y.-S. Hu, W. Yang, *J. Power Sources*, **273**, 1120–1126 (2015).

123. A. J. Bard, L. R. Faulkner, *Electrochemical Methods: Fundamentals and Applications*, John Wiley & Sons (2001).

124. C. Su, X. Bu, L. Xu, J. Liu, C. Zhang, *Electrochim. Acta*, **64**, 190–195 (2012).

125. X. Zhou, F. Wang, Y. Zhu, Z. Liu, *J. Mater. Chem.*, **21**, 3353–3358 (2011).

126. F.-Y. Su, Y. B. He, B. Li, X. C. Chen, C. H. You, W. Wei, W. Lv, Q. H. Yang, F. Kang, *Nano Energy*, **1**, 429–439 (2012).

127. D. Aurbach, B. Markovsky, Y. Talyossef, G. Salitra, H.-J. Kim, S. Choi, *J. Power Sources*, **162**, 780–789 (2006).

128. N. S. Norberg, S. F. Lux, R. Kostecki, *Electrochem. Commun.*, **34**, 29–32 (2013).

129. D. Aurbach, M. D. Levi, E. Levi, H. Teller, B. Markovsky, G. Salitra, U. Heider, L. Heider, *J. Electrochem. Soc.*, **145**, 3024– 3034 (1998).

130. C. Wu, Y. Bai, F. Wu, *J. Power Sources*, **189**, 89–94 (2009).

131. S. G. Stewart, V. Srinivasan, J. Newman, *J. Electrochem. Soc.*, **155**, A664–A671 (2008).

132. M. D. Levi, G. Salitra, B. Markovsky, H. Teller, D. Aurbach, U. Heider, L. Heider, *J. Electrochem. Soc.*, **146**, 1279–1289 (1999).

133. H. M. K. Aoichi, K. Tokuda, *J. Electroanal. Chem.*, **146**, 417–424 (1983).

134. H. Xia, Y. S. Meng, L. Lu, G. Ceder, *J. Electrochem. Soc.*, **154**, A737–A743 (2007).

135. S. Komaba, K. Shimomura, N. Yabuuchi, T. Ozeki, H. Yui, K. Konno, *J. Phys. Chem. C*, **115**, 13487–13495 (2011).

136. A. Varzi, A. Balducci, S. Passerini, *J. Electrochem. Soc.*, **161**, A368–A375 (2014).

137. Z. Zhang, T. Zeng, Y. Lai, M. Jia, J. Li, *J. Power Sources*, **247**, 1–8 (2014).

138. M. Oku, K. Hirokawa, S. Ikeda, *J. Electron Spectros. Relat. Phenomena*, **7**, 465–473 (1975).

139. G. C. Allen, S. J. Harris, J. a. Jutson, J. M. Dyke, *Appl. Surf. Sci.*, **37**, 111–134

(1989).

140. A. M. Andersson, D. P. Abraham, R. Haasch, S. MacLaren, J. Liu, K. Amine, *J. Electrochem. Soc.*, **149**, A1358–A1369 (2002).

141. P. Verma, P. Maire, P. Novák, *Electrochim. Acta*, **55**, 6332–6341 (2010).

## List of Publications

C. Arbizzani, L. Da Col, F. De Giorgio, M. Mastragostino, F. Soavi, *J. Electrochem. Soc.*, **162** (10), A2174–A2179 (2015). "Reduced graphene oxide in cathode formulations based on $LiNi_{0.5}Mn_{1.5}O_4$".

C. Arbizzani, L. Da Col, F. De Giorgio, M. Mastragostino, F. Soavi. *ECS Trans.*, **66**, 139–147 (2015). "The Role of Modified Graphene in Cathode Formulations for Lithium-Ion Batteries".

M. Zaccaria, D. Fabiani, G. Cannucciari, C. Gualandi, M. L. Focarete, C. Arbizzani, F. De Giorgio, and M. Mastragostino. *J. Electrochem. Soc.*,**162**, A915–A920 (2015). "Effect of Silica and Tin Oxide Nanoparticles on Properties of Nanofibrous Electrospun Separators".

S. Monaco, F. De Giorgio, L. Da Col, M. Riché, C. Arbizzani, M. Mastragostino. *J. Power Sources*, **278**, 733–740 (2015). "Electrochemical performance of $LiNi_{0.5}Mn_{1.5}O_4$ composite electrodes featuring carbons and reduced graphene oxide".

C. Arbizzani, F. De Giorgio, M. Mastragostino. Advances in battery technologies for electric vehicles, B. Scrosati, J. Garche and W. Tillmetz Eds., *Woodhead Publishing Ltd.*, 55–72 (2015). "Battery parameters for hybrid electric vehicles" (Chapter 4).

C. Arbizzani, F. De Giorgio, M. Mastragostino. *J. Power Sources*, **266**, 170–174 (2014). "Characterization tests for plug-in hybrid electric vehicle application of

graphite/$LiNi_{0.4}Mn_{1.6}O_4$ cells with two different separators and electrolytes".

C. Arbizzani, F. Colò, F. De Giorgio, M. Guidotti, M. Mastragostino, F. Alloin, M. Bolloli, Y. Molméret, J.-Y. Sanchez. *J. Power Sources*, **246**, 299–304 (2014). "A non-conventional fluorinated separator in high-voltage graphite/$LiNi_{0.4}Mn_{1.6}O_4$ cells"**.**

C. Arbizzani, F. De Giorgio, L. Porcarelli, M. Mastragostino, V. Khomenko, V. Barsukov, D. Bresser, S. Passerini. *J. Power Sources*, **238**, 17–20 (2013). "Use of non-conventional electrolyte salt and additives in high-voltage graphite/$LiNi_{0.4}Mn_{1.6}O_4$ batteries".

## List of contribution to Conferences

F. De Giorgio, C. Arbizzani, M. Mastragostino, N. Laszczynski, S. Passerini. CMC as effective binder for high-voltage $LiNi_{0.5}Mn_{1.5}O_4$ electrodes. *Abstract accepted as poster contribution to 18th International Meeting on Lithium Batteries (IMLB), 19-24/06/2016, Chicago (US-IL).*

F. De Giorgio, C. Arbizzani, M. Bolloli, J.-Y. Sanchez, M. Mastragostino. "High-energy lithium-ion batteries for a sustainable transport". *ExpoChimica, 25-27/11/2015,San Lazzaro di Savena (BO, IT)*. Participation with poster contribution.

C. Arbizzani, F. Bigoni, L. Da Col, F. De Giorgio, F. Soavi. "Water-soluble binders in cathode formulations for Li-ion batteries". *Giornate dell'Elettrochimica Italiana (GEI2015), 20-24/9/15, Bertinoro (FC, IT).*

C. Arbizzani, L. Da Col, F. De Giorgio, M. Mastragostino, F. Soavi. "The role of modified graphene in cathode formulations for lithium-ion batteries". *Giornate dell'Elettrochimica Italiana (GEI2015), 20-24/09/15, Bertinoro (FC, IT).*

C. Arbizzani, L. Da Col, F. De Giorgio, M. Mastragostino, F. Soavi. "The role of modified graphene in cathode formulations for lithium-ion batteries". *227th Meeting Electrochemical Society, 24-28/05/15, Chicago (US-IL).*

F. De Giorgio, C. Arbizzani, L. Da Col, M. Mastragostino, F. Soavi. "Effect of modified graphene oxide on high-voltage cathode materials for high energy lithium-ion batteries". *EST - the International Conference and Exhibition on Energy, Science & Technology, 20-22/05/2015, Karlsruhe (GE).* Participation with oral contribution.

F. De Giorgio, S. Monaco, L. Da Col, M. Riché, C. Arbizzani, M. Mastragostino. "Carbon blacks and partially reduced graphene oxide in $LiNi_{0.5}Mn_{1.5}O_4$ composite electrodes". *XIV Giornata della Chimica dell'Emilia-Romagna (Chemistry Day of the Emilia-Romagna), University of Parma (IT), 18/12/2014*. Participation with poster contribution.

M. Bolloli, A. Thiam, C. Antonelli, Y. Molméret, F. Alloin, C. Iojoiu, C. Arbizzani, M. Mastragostino, F. Colò, F. De Giorgio, J.-Y. Sanchez. "Nano Crystalline Cellulose: versatile reinforcing nanofibers for lithium battery electrolytes". *International Workshop 2014 "On the green road to environmentally friendly Li-ion cells", 28-29/10/2014, Ulm (DE).*

F. De Giorgio, S. Monaco, L. Da Col, M. Riché, C. Arbizzani and M. Mastragostino. "Electrochemical performance of $LiNi_{0.5}Mn_{1.5}O_4$ composite

electrodes featuring different carbons and reduced graphene oxides". *International Workshop 2014 "On the green road to environmentally friendly Li-ion cells", 28-29/10/2014, Ulm (DE)*. Participation with poster contribution.

C. Arbizzani, G. Cannucciari, F. De Giorgio, D. Fabiani, M. L. Focarete, M. Mastragostino, M. Zaccaria. "Comparison between Poly(vinylidene fluoride) (PVdF) electrospun and conventional separators for Li-ion batteries". *15th International Symposium on Electrets (ISE), 10-13/08/2014, Baltimore (US-MD).*

C. Arbizzani, F. De Giorgio, M. Mastragostino, S. Monaco and F. Soavi. "High-energy lithium batteries for electric transportation and stationary application". *XXXV Meeting of the Electrochemistry Group of the Spanish Royal Society of Chemistry and 1st E3 Mediterranean Symposium: Electrochemistry for environment and Energy, 14-16/07/2014, Burgos (ES).*

C. Arbizzani, F. De Giorgio and M. Mastragostino. "High voltage graphite/LNMO cells for electric transportation". *7$^{th}$ German-Italian-Japanese Meeting of Electrochemists (7$^{th}$ GIJME). 14-16/06/2014, Padova (IT).*

F. De Giorgio, C. Arbizzani, M. Bolloli, Jean-Yves Sanchez, M. Mastragostino. "New fluorinated separators for high power lithium ion batteries". *17th Meeting on Lithium Batteries (IMLB). 10-14/06/2014, Como (IT).* Participation with poster contribution

C. Arbizzani, F. De Giorgio, M. Guidotti, M. Mastragostino. "High-voltage graphite/ $LiNi_{0.4}Mn_{1.6}O_4$ cells with non-conventional fluorinated electrolytes and separators". *GEI 2013 Giornate dell'Elettrochimica Italiana 22–27/09/2013, Pavia (IT).*

C. Arbizzani, F. De Giorgio, M. Guidotti, M. Mastragostino. "Performance of AMELIE graphite/$LiNi_{0.4}Mn_{1.6}O_4$ full cells". *Workshop on "Developing Advanced Battery Materials to meet the challenge of electric vehicles". 4-5/07/2013, Grenoble (FR).*

C. Arbizzani, F. Colò, F. De Giorgio, M. Guidotti, M. Mastragostino. "Use of new fluorinated separator and electrolyte salt in 5V graphite/$LiNi_{0.4}Mn_{1.6}O_4$ batteries". *Workshop on "Batteries for future". Villa del Grumello, 06-07/05/2013, Como (IT).*